JETP Letters, Vol. 80, No. 10, 2004, pp. 617–622. From Pis'ma v Zhurnal Éksperimental'noĭ i Teoreticheskoĭ Fiziki, Vol. 80, No. 10, 2004, pp. 721–726.

Radiative Parton Energy Loss and Jet Quenching in High-Energy Heavy-Ion Collisions¶

B. G. Zakharov

Fakultät für Physik, Universität Bielefeld, D-33501 Bielefeld, Germany
Landau Institute for Theoretical Physics, Russian Academy of Sciences, Moscow, 117334 Russia

Received October 25, 2004

We study within the light-cone path integral approach [3] the effect of the induced gluon radiation on high-p_T hadrons in high-energy heavy-ion collisions. The induced gluon spectrum is represented in a new form which is convenient for numerical simulations. For the first time, computations are performed with a realistic parameterization of the dipole cross section. The results are in reasonable agreement with the suppression of high-p_T hadrons in Au + Au collisions at $\sqrt{s}$ = 200 GeV observed at RHIC. © *2004 MAIK "Nauka/Interperiodica".*

PACS numbers: 12.38.–t

1. One of the most interesting results obtained at RHIC is the suppression of high-p_T hadrons in Au + Au collisions (for a review of the data, see [1]). It is widely believed that parton energy loss due to the induced gluon radiation caused by multiple scattering in the quark-gluon plasma (QGP) produced in the initial stage of nucleus-nucleus collisions plays a major role in this phenomenon (usually called jet quenching) [2–7] (for a review, see [8]). The most general approach to the induced gluon emission is the light-cone path integral (LCPI) approach developed in [3] (see also [8–10]). It accurately treats the mass and finite-size effects and applies at arbitrary strength of the Landau–Pomeranchuk–Migdal (LPM) effect [11, 12]. Other available approaches have limited domains of applicability and can only be used either in the regime of strong (the BDMPS formalism [2, 5]) or weak (the GLV formalism [6]) LPM suppression (the GLV approach [6], in addition, is restricted to the emission of soft gluons). For this reason, they cannot be used for an accurate analysis of jet quenching for RHIC (and LHC) conditions.

The LCPI approach expresses the gluon spectrum through the solution of a two-dimensional Schrödinger equation with an imaginary potential in the impact parameter plane. The imaginary potential is proportional to the cross section of interaction of the $\bar{q}qg$ system (for $q \longrightarrow gq$ transition) with a particle in the medium, $\sigma_3(\rho)$ (here ρ is the transverse distance between the quark and gluon, the antiquark is located at the center of mass of the qg-system). The $\sigma_3(\rho)$ can be written as $\sigma_3(\rho) = C(\rho)\rho^2$. The factor $C(\rho)$ has a smooth (logarithmic) dependence on ρ for $\rho \ll 1/\mu_D$ (hereafter, μ_D is the Debye screening mass). If one replaces $C(\rho)$ by $C(\rho_{\rm eff})$, where $\rho_{\rm eff}$ is the typical value of ρ, the Hamiltonian takes the oscillator form. This approximation, which greatly simplifies the calculations, was employed in several analyses [4, 7, 13] (it was also used in the BDMPS approach [2, 5]). However, the oscillator approximation turns out to be too crude and unsatisfactory. First of all, for RHIC and LHC conditions, the dominating ρ scale is not small enough and the results depend strongly on the choice of $\rho_{\rm eff}$. Another reason why the oscillator approximation is unsatisfactory is more serious. In the high energy limit the gluon formation length, L_f, becomes larger than the quark path length in the QGP and finite-size effects become important. In this regime, $\rho_{\rm eff} \ll 1/\mu_D$ and one might naively expect that the oscillator approximation should work very well. However, one can show [14] that, in this regime, the dominating $N = 1$ rescattering contribution (and any odd rescattering) evaluated in the oscillator approximation simply vanishes. For RHIC and LHC conditions, the finite-size effects play a very important role and the oscillator approximation can lead to uncontrolled errors. For this reason, one has to use an accurate parameterization of the three-body cross section. It requires numerical calculations for solving the Schrödinger equation.

In the present paper, we represent the induced gluon spectrum in a new form that is convenient for numerical computations. We, for the first time, calculate the induced gluon emission and the nuclear modification factor for RHIC conditions using a realistic imaginary potential.

2. We consider a quark with energy E produced in a medium at $z = 0$ (we chose the z-axis along the quark

¶ This article was submitted by the author in English.

momentum). The induced gluon spectrum in the gluon fractional longitudinal momentum x reads [3]

$$\frac{dP}{dx} = 2\mathrm{Re}\int_0^\infty dz_1\int_{z_1}^\infty dz_2 g(x)[K(z_2, \boldsymbol{\rho}_2|z_1, \boldsymbol{\rho}_1) - K_v(z_2, \boldsymbol{\rho}_2|z_1, \boldsymbol{\rho}_1)]\big|_{\boldsymbol{\rho}_1=\boldsymbol{\rho}_2=0}. \quad (1)$$

Here, K is the Green's function for the Hamiltonian (acting in the transverse plane)

$$H = -\frac{1}{2M(x)}\left(\frac{\partial}{\partial\boldsymbol{\rho}}\right)^2 + v(\boldsymbol{\rho}, z) + \frac{1}{L_f}, \quad (2)$$

$$v(\boldsymbol{\rho}, z) = -i\frac{n(z)\sigma_3(\rho)}{2}, \quad (3)$$

and

$$K_v(z_2, \boldsymbol{\rho}_2|z_1, \boldsymbol{\rho}_1) = \frac{M(x)}{2\pi i(z_2-z_1)} \times \exp\left[\frac{iM(x)(\boldsymbol{\rho}_2-\boldsymbol{\rho}_1)^2}{2(z_2-z_1)} - \frac{i(z_2-z_1)}{L_f}\right] \quad (4)$$

is the Green's function for the Hamiltonian (2) with $v(\boldsymbol{\rho}, z) = 0$. In (2), the Schrödinger mass is $M(x) = Ex(1-x)$, $L_f = 2Ex(1-x)/[m_q^2x^2 + m_g^2(1-x)]$ is the gluon formation length, m_q and m_g are the quark and gluon masses that play the role of the infrared cutoffs at $x \sim 1$ and $x \sim 0$ (in the QGP, $m_{q,g}$ are given by the quark and gluon quasiparticle masses). In (3), $n(z)$ is the number density of QGP, and σ_3 is the above mentioned cross section of the color singlet $q\bar{q}g$ system with a particle in the medium. Summation over triplet (quark) and octet (gluon) color states is implicit in (3). The σ_3 may depend on z (through the Debye screening mass); however, below, we will use z-independent μ_D. The vertex factor $g(x)$, entering (1), reads

$$g(x) = \frac{\alpha_s P(x)}{2M^2(x)}\frac{\partial}{\partial\boldsymbol{\rho}_1}\frac{\partial}{\partial\boldsymbol{\rho}_2}, \quad (5)$$

where $P(x) = G_F[1 + (1-x)^2]/x$ is the splitting function for the $q \longrightarrow gq$ transition (C_F is the quark Casimir factor). Note that we neglect the spin-flip $q \longrightarrow qg$ transition, which gives a small contribution to the quark energy loss.

The three-body cross section entering potential (3) can be written as [15, 3]

$$\sigma_3(\rho) = \frac{9}{8}[\sigma_{q\bar{q}}(\rho) + \sigma_{q\bar{q}}((1-x)\rho)] - \frac{1}{8}\sigma_{q\bar{q}}(x\rho), \quad (6)$$

where

$$\sigma_{q\bar{q}}(\rho) = \alpha_s^2 C_T C_F\int d\mathbf{q}\frac{[1-\exp(i\mathbf{q}\boldsymbol{\rho})]}{(q^2+\mu_D^2)^2} \quad (7)$$

is the dipole cross section for the color singlet $q\bar{q}$ pair (C_T is the color Casimir for the thermal parton (quark or gluon)).

Spectrum (1) can be rewritten as (L is the quark path length in the medium)

$$\frac{dP}{dx} = \int_0^L dz n(z)\frac{d\sigma_{\mathrm{eff}}^{BH}(x, z)}{dx}, \quad (8)$$

$$\frac{d\sigma_{\mathrm{eff}}^{BH}(x, z)}{dx} = \mathrm{Re}\int_0^z dz_1\int_z^\infty dz_2 \times\int d\boldsymbol{\rho} g(x)K_v(z_2, \boldsymbol{\rho}_2|z, \boldsymbol{\rho})\sigma_3(\rho)K(z, \boldsymbol{\rho}|z_1, \boldsymbol{\rho}_1)\big|_{\boldsymbol{\rho}_1=\boldsymbol{\rho}_2=0}. \quad (9)$$

Cross section $d\sigma_{\mathrm{eff}}^{BH}/dx$ (9) can be viewed as an effective Bethe–Heitler cross section, which accounts for the LPM and finite-size effects. One can represent (9) as

$$\frac{d\sigma_{\mathrm{eff}}^{BH}(x, z)}{dx} = -\frac{\alpha_s P(x)}{\pi M(x)}\mathrm{Im}\int_0^z d\xi\frac{\partial}{\partial\rho}\left(\frac{F(\xi, \rho)}{\sqrt{\rho}}\right)\Big|_{\rho=0}, \quad (10)$$

where the function F is the solution to the radial Schrödinger equation for the azimuthal quantum number $m = 1$

$$i\frac{\partial F(\xi, \rho)}{\partial\xi} = \left[-\frac{1}{2M(x)}\left(\frac{\partial}{\partial\rho}\right)^2 - i\frac{n(z-\xi)\sigma_3(\rho)}{2} + \frac{4m^2-1}{8M(x)\rho^2} + \frac{1}{L_f}\right]F(\xi, \rho). \quad (11)$$

The boundary condition for $F(\xi, \rho)$ reads $F(\xi = 0, \rho) = \sqrt{\rho}\,\sigma_3(\rho)\epsilon K_1(\epsilon\rho)$, where $\epsilon = [m_q^2x^2 + m_g^2(1-x)^2]^{1/2}$, and K_1 is the Bessel function. In deriving (10), we used the relations [9]

$$\frac{\partial}{\partial\boldsymbol{\rho}_1}\frac{\partial}{\partial\boldsymbol{\rho}_2} = \frac{1}{2}\left[\left(\frac{\partial}{\partial x_1} - i\frac{\partial}{\partial y_1}\right)\left(\frac{\partial}{\partial x_2} + i\frac{\partial}{\partial y_2}\right) + \left(\frac{\partial}{\partial x_1} + i\frac{\partial}{\partial y_1}\right)\left(\frac{\partial}{\partial x_2} - i\frac{\partial}{\partial y_2}\right)\right],$$

$$\left(\frac{\partial}{\partial x_2} \pm i\frac{\partial}{\partial y_2}\right)\int_z^\infty dz_2 K_v(z_2, \boldsymbol{\rho}_2|z, \boldsymbol{\rho}) = \pm\frac{M(x)}{i\pi}\exp(\pm i\phi)K_1(\epsilon\rho).$$

The time variable ξ in (10), in terms of the variables z and z_1 of Eq. (9), is given by $\xi = z - z_1$; i.e., contrary to the Schrödinger equation for the Green's functions entering (1), (10) represents the spectrum through the solution to the Schrödinger equation, which describes the evolution of the $q\bar{q}g$ system back in time. It allows

one to have a smooth boundary condition, which is convenient for the numerical calculations.

3. The jet quenching is usually characterized by the nuclear modification factor (we consider the central rapidity region $y \sim 0$ and suppress the explicit y-dependence)

$$R_{AA}(p_T) = \frac{d\sigma^{AA}(p_T)/dy dp_T^2}{N_{\rm bin} d\sigma^{pp}(p_T)/dy dp_T^2}, \quad (12)$$

where $d\sigma^{AA}/dy dp_T^2$ and $d\sigma^{pp}/dy dp_T^2$ are the inclusive cross section for $A + A$ and $p + p$ collisions, and $N_{\rm bin}$ is the number of the binary nucleon-nucleon collisions. The effect of the parton energy loss on the high-p_T hadron production in the $A + A$ collisions can approximately be described in terms of effective hard partonic cross sections, which account for the induced gluon emission [16]. Using the power-low parameterization for the cross section of the quark production in $p + p$ collisions $\propto 1/p_T^{n(p_T)}$, one can obtain

$$R_{AA}(p_T) \approx P_0(p_T) + \frac{1}{J(p_T)} \int_0^1 dz z^{n(p_T)-2} D_q^h\left(z, \frac{p_T}{z}\right) \times \int_0^1 dx (1-x)^{n(p_T/z)-2} \frac{dI\left(x, \frac{p_T}{z(1-x)}\right)}{dx}, \quad (13)$$

$$J(p_T) = \int_0^1 dz z^{n(p_T)-2} D_q^h\left(z, \frac{p_T}{z}\right), \quad (14)$$

where P_0 is the probability of quark propagation without induced gluon emission, $dI(x, p_T)/dx$ is the probability distribution in the quark energy loss for a quark with $E = p_T$, and $D_q^h(z, p_T/z)$ is the quark fragmentation function. Note that, since $n(p_T) \gg 1$, the z-integrands in (13), (14) are sharply peaked at $z \approx \bar{z}$ ($\bar{z}$ is the value of z at which $z^{n(p_T)-2} D_q^h(z, p_T/z)$ has a maximum). For this reason, (13), to quite good accuracy, can be approximated as

$$R_{AA}(p_T) \approx P_0(p_T) + \int_0^1 dx (1-x)^{n(p_T/\bar{z})-2} \frac{dI\left(x, \frac{p_T}{\bar{z}(1-x)}\right)}{dx}. \quad (15)$$

We take the P_0 and the spectrum in the radiated energy entering (13) in the form

$$P_0(E) = \exp\left(-\int_{x_{\rm min}}^1 dx \frac{dP(x, E)}{dx}\right), \quad (16)$$

$$\frac{dI(x, E)}{dx} = \frac{dP(x, E)}{dx} \exp\left(-\int_x^1 dy \frac{dP(y, E)}{dy}\right), \quad (17)$$

where $x_{\rm min} \approx m_g/E$, and it is assumed that the spectrum equals zero at $x \le x_{\rm min}$. Formula (17) corresponds to the leading order term of the series in $L/L_{\rm rad}$ (here $L_{\rm rad}$ is the radiation length corresponding to the energy loss $\Delta E \sim E$) of the spectrum derived in [17] for the photon emission and, strictly speaking, is only valid for $\Delta E \ll E$. However, even for the more broad domain $\Delta E \lesssim E$ (which is interesting from the point of view of jet quenching at RHIC), (17) reproduces the energy loss spectrum evaluated assuming independent gluon radiation to a reasonable accuracy. An accurate calculation of the nuclear modification factor accounting for the higher order terms in $L/L_{\rm rad}$ in the approximation of independent gluon emission [16] does not make sense, because this approximation itself does not have any theoretical justification. Note that our spectrum is automatically normalized to unity.

The effective exponent $n(p_T)$ for the quark production entering (13) is close to that for hadron production, $n_h(p_T)$. The small difference between these quantities (stemming from the p_T dependence of the integral (14)) is given by $n(p_T) - n_h(p_T) = d\ln J(p_T)/d\ln p_T$. For Au + Au collisions at $\sqrt{s} = 200$ GeV, we use $n_h(p_T) = np_T/(p_T + b)$ with $n = 9.99$ and $b = 1.219$ corresponding to the parameterization $d\sigma/dy dp_T^2 = A/(p_T + b)^n$ obtained in [18] for the π^0 production in the $p + p$ collisions. The above procedure allows one to avoid the uncertainties of the pQCD calculations of the partonic cross sections.

4. To fix the $m_{q,g}$ and μ_D we use the results of the analysis of the lattice calculations within the quasiparticle model [19]. For the relevant range of temperature of the plasma $T \sim (1–3)T_c$ ($T_c \approx 170$ MeV is the temperature of the deconfinement phase transition), analysis [19] gives, for the quark and gluon quasiparticle masses, $m_q \approx 0.3$ and $m_g \approx 0.4$ GeV. With the above value of m_g from the perturbative relation $\mu_D \approx \sqrt{2}\, m_g$, one obtains $\mu_D \approx 0.57$ GeV. To study the infrared sensitivity of our results, we also perform computations for $m_g = 0.75$ GeV (with $\mu_D = 0.57$ GeV). This value of the infrared cutoff for gluon emission in parton-nucleon interaction was obtained from the analysis of the low-x proton structure function within the dipole BFKL equation [15, 20]. It seems to be reasonable for gluon emission in the developed mixed phase and for fast gluons with $L_f \gtrsim L$. This value agrees well with the natural

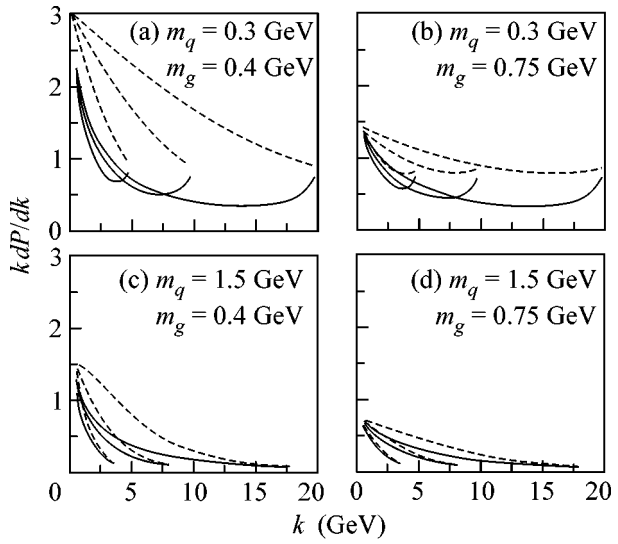

Fig. 1. The induced gluon spectrum (solid line) for $q \longrightarrow gq$ transition versus the gluon momentum k for RHIC conditions for E = 5, 10, and 20 GeV; L = 6 fm was obtained using (8), (10) with α_s = 0.5 for m_q = 0.3 GeV (a, b) and m_q = 1.5 GeV (c, d); m_g = 0.4 GeV (left) and 0.75 GeV (right). The Bethe–Heitler spectrum is shown by the dashed line.

infrared cutoff for gluon emission in the vacuum $m_g \sim 1/R_c$, where $R_c \approx 0.27$ fm is the gluon correlation radius in the QCD vacuum [21]. The above two values of m_g give reasonable lower and upper limits of the infrared cutoff for the induced gluon emission for RHIC and LHC conditions.

We perform numerical calculations for fixed and running α_s. In the first case, we take α_s = 0.5 for the gluon emission from light quarks and gluons, and α_s = 0.4 for the case of c-quark. For the running α_s, we use the parameterization (with Λ_{QCD} = 0.3 GeV) frozen at α_s = 0.7 at low momenta. This parameterization is consistent with the integral of $\alpha_s(Q)$ in the interval $0 < Q <$ 2 GeV obtained from the analysis of the heavy quark energy loss (in vacuum) [22]. Previously, this parameterization was used to successfully describe the HERA data on the low-x proton structure function within the dipole BFKL approach [15, 20]. To incorporate the running α_s in our formalism, we include α_s in the integrand on the right-hand side of (10) and take for virtuality $Q^2 = aM(x)/\xi$. The parameter a was adjusted to reproduce the N = 1 rescattering contribution evaluated in the ordinary diagrammatic approach [23]. It gives $a \approx 1.85$. For the dipole cross section (7), we take $Q^2 = \mathbf{q}^2$.

We assume the Bjorken [24] longitudinal expansion of the QGP with $T^3\tau = T_0^3\tau_0$, which gives $n(z) \propto 1/z$ for $z > \tau_0$. We use the initial conditions suggested in [25]: T_0 = 446 MeV and τ_0 = 0.147 fm for RHIC, and T_0 = 897 MeV and τ_0 = 0.073 fm for LHC. For RHIC, the above conditions were obtained from the charged particle pseudorapidity density $dN/dy \approx 1260$ measured by the PHOBOS experiment [26] in Au + Au collisions at $\sqrt{s}$ = 200 GeV, assuming an isentropic expansion and rapid thermolization at $\tau_0 \sim 1/3T_0$. The LHC parameters correspond to $dN/dy \approx 5625$ at $\sqrt{s}$ = 5.5 TeV, which was estimated in [27]. The above initial conditions for RHIC (translated into τ_0 = 0.6 fm) agrees with those used in the successful hydrodynamic description of Au + Au collisions at RHIC [28]. Note that, since the dominating ρ-scale in (9) $\propto \sqrt{z}$ for $z \ll L_f$, our results are not very sensitive to τ_0 (for a given entropy). The maximum parton path length in the hot QCD medium is restricted by the lifetime of the QGP (and mixed) phase,[1] $\tau_{\max}$. We take $\tau_{\max} \sim R_A \sim 6$ fm. This seems to be a reasonable value for the central heavy-ion collisions, since, due to the transverse expansion, the hot QCD matter should cool quickly at $\tau \gtrsim R_A$ [24].

In Fig. 1, we show the induced gluon spectrum for the $q \longrightarrow gq$ transition for RHIC conditions for the quark path length L = 6 fm obtained with m_q = 0.3 and m_q = 1.5 GeV for m_g = 0.4 and m_g = 0.75 GeV. In Fig. 1, we also show the Bethe–Heitler spectrum (dashed line). One sees that the LPM and finite-size effects strongly suppress the gluon emission. The gluon emission from the c-quark is suppressed in comparison with the light quark due to its larger, mass which leads to decreasing of the dominating ρ scale (note that the spectrum is not sensitive to the light quark mass, except for $x \sim 1$). One can see from Fig. 1 that, although the Bethe–Heitler spectrum differs strongly for two values of m_g, the difference becomes relatively small for the spectrum, which accounts for the LPM and finite-size effects. It is connected with the fact that, due to the multiple scattering and finite-size effects, the dominating 1/ρ-scale becomes larger than m_g; namely, this in-medium scale plays the role of the infrared cutoff at high energies [4] (however, of course, for not very high p_T, the value of m_g is still important). We do not show the spectra for running α_s. They are similar in form (but somewhat suppressed at moderate fractional momenta). The LPM suppression for LHC is considerably stronger than for RHIC, but the spectra are similar in form, and we do not show them as well.

In Fig. 2, we plot the quark energy loss $\Delta E = E\int_{x_{\min}}^1 dx x dP/dx$ evaluated for fixed (solid line) and running (dashed line) α_s for RHIC and LHC conditions for L = 6 fm with m_g = 0.4 GeV (thick lines) and m_g = 0.75 GeV (thin lines). The results for α_s = 0.5 agree roughly with those for running α_s for $E \lesssim 10$ GeV, but, at higher energies, the energy dependence is steeper for

[1] For our choice of the initial conditions, the lifetime of QGP is ~3 fm for RHIC. However, in the interval $\tau \sim$ 3–6 fm, the density of the mixed phase is practically the same as that for the pure QGP phase.

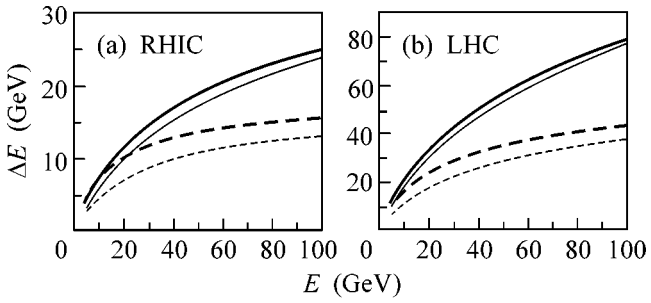

Fig. 2. The energy dependence of the quark energy loss for (a) RHIC and (b) LHC for $L = 6$ fm as obtained with $\alpha_s = 0.5$ (solid line) and running α_s (dashed line), $m_g = 0.4$ GeV (thick lines) and $m_g = 0.75$ GeV (thin lines), $m_q = 0.3$ GeV.

fixed α_s. This says that the typical ρ-scale becomes smaller with increasing energy. It is also seen from the decrease of the relative difference between the curves for $m_g = 0.4$ and 0.75 GeV.

In Fig. 3a, we compare the nuclear modification factor (13) for $T_0 = 446$ MeV calculated using the NLO KKP fragmentation functions [29] for running α_s with that obtained at RHIC [1] for central Au + Au collisions at $\sqrt{s} = 200$ GeV. For illustration of the dependence on T_0, in Fig. 3b, we also present the results for $T_0 = 375$ MeV. The theoretical curves were obtained for $L = 4.9$ fm. It is the typical parton path length in the QGP (and mixed) phase for $\tau_{\max} = 6$ fm. We present the results for $m_g = 0.4$ and 0.75 GeV. For $p_T \lesssim 15$, the results for $\alpha_s = 0.5$ are close to that for running α_s and we do not plot them. The results for the quark (solid line) and gluon (dashed line) jets are shown separately (note that, for $\sqrt{s} = 200$ GeV, the quark and gluon contributions are comparable). The suppression is somewhat stronger for gluon jets. One can see from Fig. 3a that the theoretical R_{AA} for $m_g = 0.4$ is in reasonable agreement with the experimental one. One should bear in mind, however, that our calculations neglect the collisional energy loss [30]. For $p_T \sim 5$–15 GeV, the collisional energy loss may increase the total energy loss by ~30–40%. In this case (if one takes the initial conditions [25]) the value $m_g = 0.75$ GeV would be more preferable for agreement with the RHIC data. As mentioned previously, this value is reasonable for the mixed phase and for gluons with $L_f \gtrsim L$. Since, for $\sqrt{s} = 200$ GeV, the medium spends about half of its time in the mixed phase, the effective infrared cutoff may be larger than the gluon quasiparticle mass in the QGP. For this reason, the collisional energy loss may be included without using an unrealistic infrared cutoff for the induced energy loss. The possible remaining small disagreement with the data may be avoided by taking a somewhat smaller value of T_0 (or α_s). In any case, it is clear that, for such a complicated phenomenon, it is hardly possible to expect perfect agreement with experiment and the agreement found in the present paper is surprisingly good.

The above estimate for the collisional energy loss was obtained for the pQCD plasma. Presently, there are some indications [31] that the medium produced at RHIC may be a strongly coupled QGP. The radiative energy loss should not be very sensitive to the dynamics

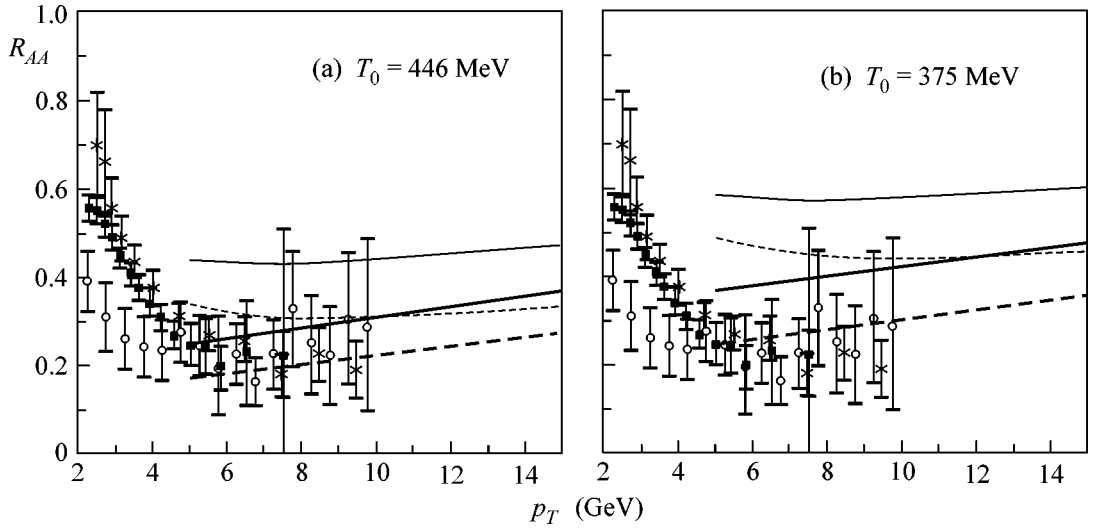

Fig. 3. The nuclear modification factor (13) for central Au + Au collisions at $\sqrt{s} = 200$ GeV for quark (solid line) and gluon (dashed line) jets obtained with m_g = (thick lines) 0.4 and (thin lines) 0.75 GeV for running α_s. The experimental points (from [1]) are for the following: circle—Au + Au $\longrightarrow \pi^0 + X$ (0–10% central) [PHENIX Collaboration], square—Au + Au $\longrightarrow h^{\pm} + X$ (0–10% central) [PHENIX Collaboration], star—Au + Au $\longrightarrow h^{\pm} + X$ (0–5% central) [STAR Collaboration].

of the QGP (for the same number density of the QGP). However, it may be important for the collisional energy loss. Unfortunately, the corresponding calculations have not been performed yet. It is interesting that our results give support for the scenario with strongly coupled QGP. Indeed, this scenario requires $\alpha_s \gtrsim 0.5$ [31] for the thermal partons. The R_{AA} is sensitive to the radiation of soft gluons with an energy of about a few μ_D. One can expect that, for such gluons, α_s should be close to that for thermal partons. We obtained agreement with the data with α_s, which is frozen at a value of 0.7 at low momenta. If α_s is frozen at a value below 0.4–0.5, the theoretical R_{AA} strongly disagrees with that observed at RHIC.

5. In summary, we have represented, within the LCPI approach [3], the induced gluon spectrum in a new form convenient for numerical calculations and carried out computations of the induced gluon emission from fast partons in the expanding QGP for RHIC and LHC conditions. The calculations, for the first time, have been performed with a realistic parameterization of the dipole cross section. The theoretical nuclear modification factor calculated for the initial conditions obtained from the charged particle rapidity density observed at RHIC [25] and the hydrodynamic simulation of the RHIC data [28] are in reasonable agreement with that observed at RHIC.

ACKNOWLEDGMENTS

I thank R. Baier and D. Schildknecht for discussions and their kind hospitality at the University of Bielefeld, where this work was completed. I am also grateful to the High Energy Group of the ICTP for their kind hospitality during my visit to Trieste, where part of this work was performed.

This work was supported by DFG, grant Schi 189/6-1.

REFERENCES

1. D. d'Enterria, *Invited overview talk at 39th Rencontres de Moriond on QCD and High-Energy Hadronic Interactions, La Thuile, Italy, 2004*; nucl-ex/0406012.
2. R. Baier, Y. L. Dokshitzer, A. H. Mueller, *et al.*, Nucl. Phys. B **483**, 291 (1997); **484**, 265 (1997).
3. B. G. Zakharov, JETP Lett. **63**, 952 (1996).
4. B. G. Zakharov, JETP Lett. **65**, 615 (1997).
5. R. Baier, Y. L. Dokshitzer, A. H. Mueller, and D. Schiff, Nucl. Phys. B **531**, 403 (1998).
6. M. Gyulassy, P. Lévai, and I. Vitev, Nucl. Phys. B **594**, 371 (2001).
7. U. A. Wiedemann, Nucl. Phys. A **690**, 731 (2001).
8. R. Baier, D. Schiff, and B. G. Zakharov, Annu. Rev. Nucl. Part. Sci. **50**, 37 (2000).
9. B. G. Zakharov, Phys. At. Nucl. **61**, 838 (1998).
10. B. G. Zakharov, JETP Lett. **70**, 176 (1999).
11. L. D. Landau and I. Ya. Pomeranchuk, Dokl. Akad. Nauk SSSR **92**, 535 (1953); **92**, 735 (1953).
12. A. B. Migdal, Phys. Rev. **103**, 1811 (1956).
13. C. A. Salgado and U. A. Wiedemann, Phys. Rev. Lett. **89**, 092303 (2002); Phys. Rev. D **68**, 014008 (2003).
14. B. G. Zakharov, JETP Lett. **73**, 49 (2001).
15. N. N. Nikolaev, B. G. Zakharov, and V. R. Zoller, Phys. Lett. B **328**, 486 (1994).
16. R. Baier, Yu. L. Dokshitzer, A. H. Mueller, and D. Schiff, J. High Energy Phys. **0109**, 033 (2001); hep-ph/0106347 (2001).
17. B. G. Zakharov, Phys. At. Nucl. **62**, 1008 (1999); JETP Lett. **78**, 759 (2003).
18. S. S. Adler *et al.* (PHENIX Collab.), Phys. Rev. Lett. **91**, 241803 (2003).
19. P. Lévai and U. Heinz, Phys. Rev. C **57**, 1879 (1998).
20. N. N. Nikolaev and B. G. Zakharov, Phys. Lett. B **327**, 149 (1994).
21. E. V. Shuryak, Rev. Mod. Phys. **65**, 1 (1993).
22. Yu. L. Dokshitzer, V. A. Khoze, and S. I. Troyan, Phys. Rev. D **53**, 89 (1996).
23. B. G. Zakharov, JETP Lett. **80**, 67 (2004).
24. J. D. Bjorken, Phys. Rev. D **27**, 140 (1983).
25. R. J. Fries, B. Müller, and D. K. Srivastava, Phys. Rev. Lett. **90**, 132301 (2003).
26. B. B. Back *et al.* (PHOBOS Collab.), Phys. Rev. C **65**, 061901 (2002).
27. J. Kapusta, L. D. McLerran, and D. K. Srivastava, Phys. Lett. B **283**, 145 (1992).
28. U. W. Heinz and P. F. Kolb, Nucl. Phys. A **702**, 269 (2002).
29. B. A. Kniehl, G. Kramer, and B. Potter, Nucl. Phys. B **582**, 514 (2000).
30. J. D. Bjorken, Fermilab Preprint Pub-82/59-THY (1982).
31. E. V. Shuryak, hep-ph/0405066; E. V. Shuryak and I. Zahed, hep-ph/0403127.

JETP Letters, Vol. 80, No. 10, 2004, pp. 623–627. Translated from Pis'ma v Zhurnal Éksperimental'noĭ i Teoreticheskoĭ Fiziki, Vol. 80, No. 10, 2004, pp. 727–731.

On the Dynamic Properties of "Elastic" Interactions between Wave Solitons Consisting of a Few Field Oscillation Cycles

S. A. Skobelev* and A. V. Kim

Institute of Applied Physics, Russian Academy of Sciences, ul. Ul'yanova 46, Nizhni Novgorod, 603950 Russia
** e-mail: sksa@ufp.appl.sci-nnov.ru*

Received August 17, 2004; in final form, October 28, 2004

By the numerical simulation of the dynamics of the optical circularly polarized field in the Kerr-type medium, it has been shown that the binary collisions between wave solitons consisting of a few field oscillation cycles with respect to their energy characteristics exhibit the properties of the collisions of Schrödinger solitons. The corresponding spectral characteristics change according to the conservation of the soliton-like structure of the envelop. In dependence on the absolute difference of the field phases, there are three different interaction regimes: the passage of one structure through another, their repulsion, and the exact replication of one initial wave structure by another. © *2004 MAIK "Nauka/Interperiodica".*

PACS numbers: 41.20.Jb; 42.65.Re; 42.65.Tg

The transition of envelop solitons described by the nonlinear Schrödinger equation and its modifications [1, 2] to wave solitons containing a few field oscillation cycles is an interesting and important step in the theory of nonlinear wave phenomena [3, 4]. A newly found class of solitary solutions of the wave equation with Kerr-type nonlinearity that describes the propagation of electromagnetic pulses of a circularly polarized field with a soliton-structure envelop includes a few oscillations down to one [5]. This analysis seems to also be important for applications in view of the considerable advances in laser technology in the generation of ultrashort light pulses as short as a few optical-oscillation periods. Such pulses have a number of wide potentialities for their scientific and engineering applications, among which we point to possible superdense information packing with the use of such ultrashort pulses and the corresponding ultrafast communication [6–8]. The problem of the complete integrability of the initial nonlinear wave equation is certainly of fundamental importance for the general theory of nonlinear waves, but it seems to be hardly solvable. In this respect, it is natural to use a technique showing good performance such as the numerical-simulation analysis of binary collisions of wave solitons that are the exact solutions of the nonlinear wave equation of the corresponding Hamiltonian system. In this work, we performed the direct numerical simulation of the nonlinear dynamics of the optical field in a medium with Kerr nonlinearity. It has been shown that, in the class of circularly polarized fields, wave solitons consisting of a few oscillations in binary collisions hold the properties of collisions of Schrödinger solitons regarding the structure of their envelop. At the same time, their frequency content can change, but the soliton-like structure is conserved. Free fields, i.e., the nonsoliton part of the spectrum, are not emitted during collisions and the total energy of the solitons is thereby conserved.

For extensive analysis of the nonlinear wave problem describing the dynamics of the field as a whole, without scale separation into the slow envelop and high-frequency content, it is convenient to use the reduced form of the wave equation in the so-called reflectionless approximation, implying that the changes in the field distributions are small in the characteristic wavelengths. In this case, the vector wave equation with nonlinearity of the electron type, which allows solitary solutions in the form of wave solitons, can be represented in the form [5]

$$\frac{\partial^2 \mathbf{E}}{\partial z \partial \tau} + \mathbf{E} + \frac{\partial^2}{\partial \tau^2}(\mathbf{E}^2\mathbf{E}) = 0. \quad (1)$$

As is easily seen, Eq. (1) allows scale invariance and thereby can be written in a dimensionless form. Here, z is the coordinate along the propagation direction, $\tau = t - z\varepsilon_o^{1/2}/c$ is the retarded time, ε_o is the static dielectric constant of the medium, and c is the speed of light in vacuum. In particular, this equation describes the propagation of ultrashort pulses in a quartz optic fiber in the anomalous-dispersion region [3] if the pulse spectrum is sufficiently far from the zero-dispersion point, as well as in an ionized gas, where plasma dispersion prevails over the gas dispersion associated with neutral particles [9].

0021-3640/04/8010-0623$26.00 © 2004 MAIK "Nauka/Interperiodica"

Equation (1) belongs to the class of Hamiltonian systems with the Hamiltonian

$$H = \int_{-\infty}^{+\infty}\left[\left(\int_{-\infty}^{\tau}\mathbf{E}d\tau'\right)^2 - \frac{1}{2}(\mathbf{E}\cdot\mathbf{E})^2\right]d\tau. \quad (2)$$

We emphasize that Eq. (1) allows the existence of other integrals of motion, in particular, the zero mean field [5]. However, Eq. (2) is useful for simulation due to the known high sensitivity of the Hamiltonian to the accuracy of the numerical calculation. This property will be used for increased control over the numerical experiment. A remarkable property of this equation is the existence of localized soliton-like solutions for the circularly polarized field that are stable under small perturbations. For the case of high-frequency content (long pulses consisting of numerous field oscillation cycles), they are smoothly transformed to well-known Schrödinger solitons. In particular, this circumstance makes it possible to hope that wave solitons consisting of a few oscillations will inherit certain properties of Schrödinger solitons. The conservation of the soliton structures of two solitons in their elastic collision is among such important properties. We treat the conservation of the soliton structure of the wave field as the conservation of only the soliton-like structure of the envelop, implying that its spectral content can change significantly due to the nonlinear character of the interaction. The wave solitons of Eq. (1) can be represented as a two-parameter family of solutions of the form [5]

$$\mathbf{E}(z,\tau) = a(\tau-\gamma z)[\mathbf{e}_x\cos\varphi(z,\tau) + \mathbf{e}_y\sin\varphi(z,\tau)], \quad (3)$$

$$\varphi(z,\tau) = \omega(\tau+\gamma z) + \int\frac{\omega a^2(3\gamma-2a^2)}{2(\gamma-a^2)^2}d(\tau-\gamma z) + \varphi_o. \quad (4)$$

Here, ω is the characteristic carrier frequency, γ is the parameter determining the group velocity of the soliton, φ_o is the constant phase of the field, and its envelop $a(\tau - \gamma z)$ satisfies the ordinary differential equation, which can be represented in the following quadrature for the normalized quantities $\xi = \omega(\tau - \gamma z)$ and $u = a/(\gamma)^{1/2}$ in the class of localized functions:

$$\int_{u_m}^{u}\frac{1-3u^2}{u\sqrt{\delta^2 - F(u^2)}}du = \pm(\xi-\xi_o). \quad (5)$$

Here, $F(u^2) = u^2[(3/2)(1+\delta^2) - (4-5u^2)/4(1-u^2)^2]$, the maximum amplitude u_m of the soliton is determined by the real root of the cubic equation $F(u_m^2) = \delta^2$ (except one limiting solution for which $u_m^2 = 2/3$ at $\delta^2 = 1/8$), and ξ_o is the integration constant corresponding to the position of the field-envelop maximum. As seen in Eq. (5), its solution depends only on the parameter $\delta^2 = 1/\gamma\omega^2 - 1$, which is expressed in terms of ω and γ and lies in the interval $0 \le \delta^2 \le 1/8$. Using the smallness of the parameter δ^2, one can represent the amplitude of the wave soliton in the form $u_m \simeq \delta\sqrt{2(1+8\delta^2/3)}$. For small amplitudes $u_m^2 \ll 1/3$, which correspond to extremely small δ values, it is easy to see that solutions (5) have the form of the sech function and correspond to the Schrödinger envelop solitons. Note that, for extremely short durations, despite the broad signal spectrum comparable with the average frequency, it is convenient to treat ω as the characteristic carrier frequency, which is the carrier frequency in the small-amplitude limit. An important feature of the wave solitons under consideration is the semibounded spectrum of their admissible solutions; i.e., the existence of the boundary solution corresponding to the limiting soliton with the maximum possible pulse duration and, correspondingly, with the maximum possible amplitude. With an increase in δ, the amplitude of the soliton increases, and, its duration, which is determined from the half-width of the intensity, decreases, reaching the minimum possible value $\tau_s = 2.3\omega^{-1}$, which is smaller than half the oscillation period at $\delta^2 = 1/8$. It is worth noting that wave solitons consisting of a few oscillations have strong frequency modulation, which prevents the unambiguous introduction of a certain phase velocity for such structure formations. This property distinguishes them from previously known wave solitons [10, 11], for which the carrier frequency and carrier wave vector are strictly defined. The appropriately fitted frequency chirp is apparently responsible for the stability of the wave structures under consideration, which can be easily formed by specifying the appropriate initial, localized field distributions even for the linearly polarized field, as well as for more general equations including, e.g., high-frequency dispersion [3, 4, 9], where they may be only approximate, weakly damping, soliton-like solutions.

Since Eqs. (1) are "one-directional," to analyze the binary-collision dynamics, we arrange solitons (3) in the order of decreasing their group velocities. In addition, they are arranged such that they do not overlap in space. The initial conditions are naturally specified in the form of the wave structures given by Eqs. (3)–(5), which are the exact solutions of initial Eq. (1). We distinguish two fundamentally different cases of interacting solitons. First, interacting solitons have close frequencies. In this case, the results can be compared with the results for Schrödinger solitons. The second case, where the characteristic frequencies noticeably differ from each other, has no corresponding analogue.

In the first run of numerical experiments, the ω values are taken identical for colliding solitons. The amplitudes of the solitons, as well as the absolute phase difference of their frequency content, are taken as the varying parameters. For a fixed distance between the solitons, the absolute phase difference is given as $\Delta\varphi = \varphi_{o1} - \varphi_{o2}$, where φ_{o1} and φ_{o2} are the constant phases of

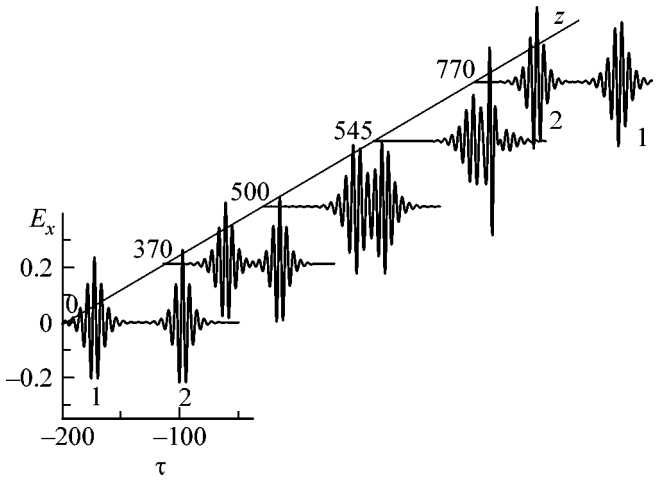

Fig. 1. Regime of passing the solitons consisting of a few oscillations through each other with the complete conservation of their wave structure, including the frequency contents, for the parameters ω = 1 (characteristic oscillation period ≈2π, a_{s1} = 0.24, τ_{s1} = 9.2 (δ_1 = 0.17), a_{s2} = 0.26, τ_{s2} = 8 (δ_2 = 0.19), and Δφ = 0, where a_{si} and τ_{si} are the amplitude and duration of the *i*th (first or second) soliton, which are also marked by the respective numbers in the figure.

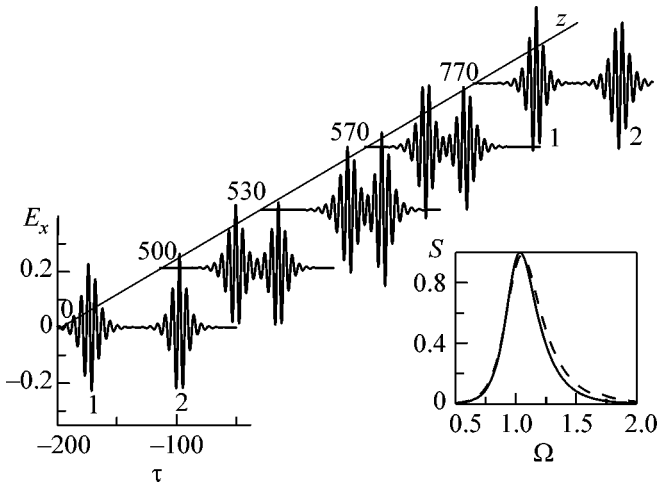

Fig. 2. Regime of the replication of one initial wave structure by another for the parameters ω = 1, a_{s1} = 0.24, τ_{s1} = 9.2 (δ_1 = 0.17), a_{s2} = 0.26, τ_{s2} = 8 (δ_2 = 0.19), and Δφ = 0.5π. The inset shows the spectral powers of the (the solid line before and the dashed line after the interaction) first and (the dashed line before and the solid line after the interaction) second solitons $S(\Omega)$.

the first and second solitons, respectively [see Eq. (4)]. The performed numerical calculations clearly reveal three different regimes of the dynamic interaction between wave solitons, which can be summarized as follows.

If the amplitudes of the colliding solitons differ from each other by more than 40% (the numerical values presented hereinafter are approximate and can generally change in dependence on the interval of the soliton parameters; in particular, the indicated value corresponds to ω ~ 1 and a ~ 0.2), and only the following interaction regime is always observed: the solitons pass through each other with the complete conservation of their wave structure, including their frequency contents. A typical pattern of the regime of passing one wave structure through another is given in Fig. 1.

If the amplitudes of the colliding solitons differ from each other by less than 40%, three different regimes of their interaction are possible in dependence on the phase difference. Figures 1–4 show the typical scenarios of these regimes. In the phase-difference interval $-\pi/8 < \Delta\varphi < \pi/8$, which depends slightly on the amplitudes of the colliding solitons in the general case, the solitons pass through each other without changes (see Fig. 1), as in the case of a noticeable difference between their amplitudes, although their interaction can be long and complex. For close amplitudes, their relative velocity is low, and, therefore, they pass through each other for a long time, likely with a certain energy exchange in some time intervals. In this case, according to the spectral analysis, their frequency contents are virtually unchanged after the interaction. This means that the wave structures remain completely identical in the asymptotic regions, at least disregarding a certain delay with respect to the unperturbed motion. This delay is determined by nonlinear interaction, and it decreases with an increase in the amplitude difference.

If the phase difference lies in the interval $\pi/8 < \Delta\varphi < 5\pi/4$, the soliton with the larger amplitude overtakes the slower soliton but does not pass through the latter soliton and is located behind it, as is shown in Fig. 2. In a certain interaction period, this coupled pair exchanges

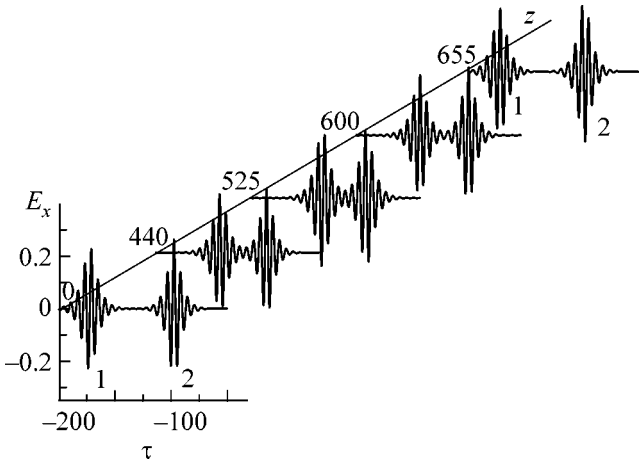

Fig. 3. Regime of the repulsion of a wave soliton pair from each other for the parameters ω = 1, a_{s1} = 0.24, τ_{s1} = 9.2 (δ_1 = 0.17), a_{s2} = 0.26, τ_{s2} = 8 (δ_2 = 0.19), and Δφ = 1.5π.

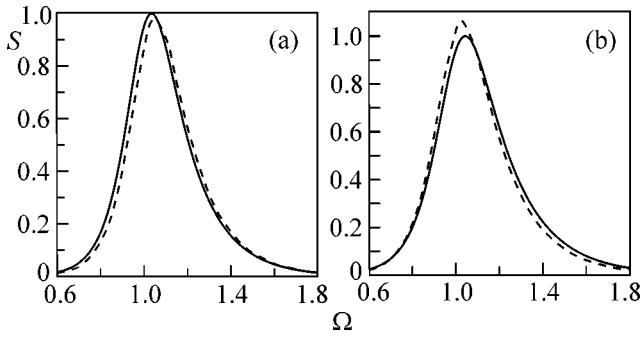

Fig. 4. Spectral powers of the (a) first and (b) second wave solitons $S(\Omega)$ (solid line) before and (dashed line) after the interaction. For the parameters indicated in Fig. 3.

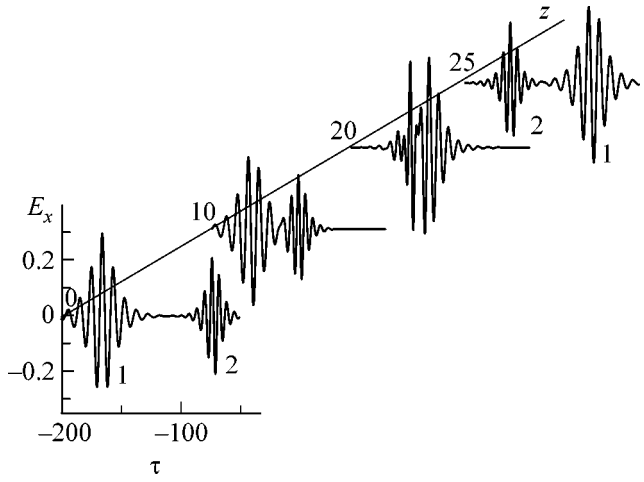

Fig. 5. Regime of the interaction between the wave solitons with different carrier frequencies $\omega = 0.8$ and 1.4 for the parameters $a_{s1} = 0.29$, $\tau_{s1} = 11.5$ ($\delta_1 = 0.16$), $a_{s2} = 0.22$, and $\tau_{s2} = 6.67$ ($\delta_2 = 0.18$).

energy with the complete replication of one soliton by another. Then, the solitons begin to propagate independently, also exchanging velocities; i.e., the enhanced second soliton, which was initially slower, takes the velocity of the first soliton and moves away from it. In this case, the complete copying of the spectral content of the wave field occurs. Figure 2 shows (inset) the spectral powers of the wave solitons $S(\Omega)$ before and after interaction. As seen, they are completely identical to each other within the numerical-calculation errors. Note that, in the two regimes described above, a new wave structure was not produced; i.e., the wave solitons remain asymptotically the same after the interaction, including their high-frequency content.

As seen in Fig. 3, in the phase-difference interval $5\pi/4 < \Delta\varphi < 7\pi/4$, the repulsive regime is observed. This means that, after a certain transient period, when the solitons interact with each other approaching each other but remaining sufficiently separated in space, the solitons scatter from each other. In this case, the parameters, primarily the high-frequency content, of the wave solitons change. This regime only conditionally can be called elastic in application to the wave field, because the wave structures before and after interaction are not strictly the same, although these differences are small for a small difference between the soliton amplitudes when this interaction regime is observed. Figure 4 shows the typical pattern of change in the spectral contents of the solitons (solid lines) before and (dashed lines) after the interaction. We emphasize that the spectral content changes so that the wave structures after the interaction remain solitons according to the solution given by Eqs. (3) and (4). In this case, the spectrum of the first reflected soliton is shifted toward the blue part, whereas the spectrum of the second soliton, which acquires additional "momentum" in the direction of its propagation, is shifted toward the opposite, red part.

In the second run of the calculations, the parameters ω for two colliding solitons are taken different from each other. In this case, as for the case of a noticeable amplitude difference, only one interaction regime is observed: solitons pass through each other, remaining asymptotically unchanged. This regime is observed up to a phase difference of about 5% for $\omega \sim 1$. Figure 5 shows the typical scenario for the parameters $\omega = 0.8$ and 1.4, $a_{s1} = 0.29$, $\tau_{s1} = 11.5$ ($\delta_1 = 0.16$) and $a_{s2} = 0.22$, $\tau_{s2} = 6.67$ ($\delta_2 = 0.18$). In this case, the solitons pass through each other virtually without interaction and change in their spectral content. It is also seen that, owing to a noticeable difference in the group velocities, the effective interaction, i.e., the overlapping of the wave packets, occurs only in a short propagation path ($7 \lesssim z \lesssim 25$), whereas the long-term interaction ($z \sim 700$) between the wave solitons occurs in the above cases (see Figs. 1–3). It should be noted that the generation of nonsoliton components is absent in all the soliton-interaction regimes; i.e., the total energy of the wave structures remains unchanged.

Thus, the performed numerical experiments on the binary collisions between wave solitons provide the following conclusions expressing certain dynamic properties of vector wave equation (1) in the class of circularly polarized fields. First, the soliton-like structure of the wave fields is not broken in collisions; i.e., the wave solitons hold their soliton stricture after collisions. Second, free fields, i.e., the nonsoliton part of the spectrum, are not emitted during collisions and the total energy accumulated in the solitons is thereby conserved. These conclusions are naturally not exact statements, because they are based only on the numerical-simulation results. Nevertheless, they can be useful for both theoretical investigation and practical use of short-duration wave solitons, similarly to the role of the Schrödinger envelop solitons.

This work was supported by the Russian Foundation for Basic Research, project no. 04-02-16420.

REFERENCES

1. S. P. Novikov, S. V. Manakov, L. P. Pitaevskii, and V. E. Zakharov, *Theory of Solitons: the Inverse Scattering Method* (Nauka, Moscow, 1980; Consultants Bureau, New York, 1984).
2. E. M. Gromov and V. I. Talanov, Izv. Vyssh. Uchebn. Zaved., Radiofiz. **41**, 222 (1998).
3. S. A. Kozlov and S. V. Sazonov, Zh. Éksp. Teor. Fiz. **111**, 404 (1997) [JETP **84**, 221 (1997)].
4. D. V. Kartashov, A. V. Kim, and S. A. Skobelev, Izv. Vyssh. Uchebn. Zaved., Radiofiz. **46**, 415 (2003) [Radiophys. Quantum Electron. **45**, 374 (2003)].
5. D. V. Kartashov, A. V. Kim, and S. A. Skobelev, Pis'ma Zh. Éksp. Teor. Fiz. **78**, 722 (2003) [JETP Lett. **78**, 276 (2003)].
6. A. Baltuska, Z. Wei, M. S. Pshenichnikov, and D. A. Wiersma, Opt. Lett. **22**, 102 (1997).
7. M. Nisoli, S. De Silvestri, O. Svelto, *et al.*, Opt. Lett. **22**, 522 (1997).
8. T. Brabec and F. Krausz, Rev. Mod. Phys. **72**, 545 (2000).
9. A. Nazarkin and G. Korn, Phys. Rev. Lett. **83**, 4748 (1999).
10. K. A. Gorshkov, V. A. Kozlov, and L. A. Ostrovskiĭ, Zh. Éksp. Teor. Fiz. **65**, 189 (1973) [Sov. Phys. JETP **38**, 93 (1974)].
11. V. A. Kozlov, A. G. Litvak, and E. V. Suvorov, Zh. Éksp. Teor. Fiz. **76**, 148 (1979) [Sov. Phys. JETP **49**, 75 (1979)].

Translated by R. Tyapaev

JETP Letters, Vol. 80, No. 10, 2004, pp. 628–632. Translated from Pis'ma v Zhurnal Éksperimental'noĭ i Teoreticheskoĭ Fiziki, Vol. 80, No. 10, 2004, pp. 732–736.

A New Class of MO_2 Dioxide Nanotubes (M = Si, Ge, Sn, Pb) Composed of "Square" Lattices of Atoms: Their Structure and Energy Characteristics

L. A. Chernozatonskiĭ

Institute of Chemical Physics, Russian Academy of Sciences, Moscow, 119991 Russia

Received October 7, 2004

New dioxide nanotubes are described. These nanotubes are rolled up of a "square" lattice of atoms differing from the conventional hexagonal lattice isoelectronic to graphite. The dependence of the strain energy on the nanotube diameter D departs from a $1/D^2$ behavior, and the optimum shape at the same diameter corresponds to "zigzag" tubelenes. Two-layer nanotubes consisting of an MO_2 layer bonded to a carbon nanotube (CNT) are characterized by a considerably lower strain energy, which points to the possibility of using CNTs as a template for the synthesis of such MO_2 nanotubes. © *2004 MAIK "Nauka/Interperiodica".*

PACS numbers: 61.46.+w; 68.65.–k

The discovery of dichalcogenide (Mo, W)S_2 nanotubes, which was reported in 1992, in which atoms were arranged on three cylindrical surfaces promoted studies of noncarbon nanotubes [1]. Recently, a group of French researchers has determined the structure of a complex fullerenoid oxide consisting of spherical Al–O–SrBi–O–Bi–O polyhedra built into each other [2], and Bromley *et al.* [3, 4] have considered hypothetic hollow $(SiO_2)_N$ clusters (N = 6–12, 24). The structures of such a complex composition represent a new area for studying the unique physical and chemical properties of not only spheroidal but also tubular nanoclusters.

In this communication, the author draws attention to the possibility of the existence of a new class of energy-stable three-cylinder nanotubes composed of MO_2 oxides (M = Si, Ge, Sn, Pb), which, because of their dielectric, mechanical, and piezoelectric properties, can be used as protective dielectric sheaths of nanowires and also as elements of nanophotonic devices.

It is known that the MO_4 tetrahedron with an M atom at the center and oxygen atoms at the vertices is the basic element of all MO_2 structures (crystalline, amorphous, and polytypic). Such dioxides are dielectrics and semiconductors and can exist in nature (for example, the mineral cassiterite SnO_2). As distinct from the dioxide structures studied previously, consider a three-atomic layer in which the tetrahedra are arranged in such a way that the oxygen and silicon atoms are located only in the three planes of this layer (Fig. 1). Calculations performed showed the stability of such MO_2 layers. The basic structural features of the MO_2 nanotubes will be demonstrated by calculations of nanotubes rolled up of silicon and tin dioxides (calculations of nanotubes composed of Ge or Pb dioxides demonstrate similar features).

Classification of the nanotubes. The structure of the nanotubes will be described in the framework of a model that represents a strip of a planar lattice of atoms rolled up analogously to nanotubes obtained from a layer with a hexagonal lattice [1, 5–7]. Thus, a single-layer (n, m) nanotube will be determined as a layer of a rectangular network of SiO_2 atoms rolled up into a cylinder (Fig. 1). The Si atoms are located in its basic

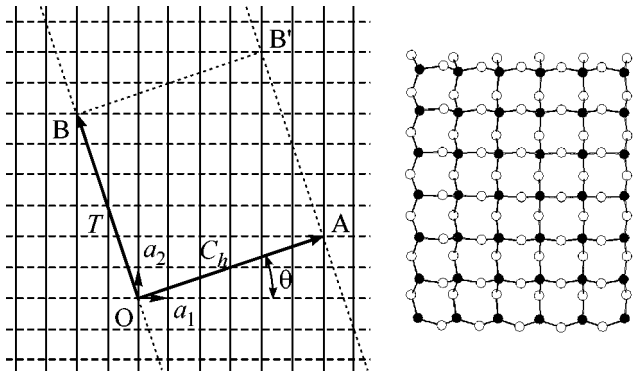

Fig. 1. Schematic diagram of a nonrolled rectangular lattice of MO_2 nanotubes (M = Si, Ge, Sn, Pb). A nanotube can be formed by connecting points O and A and also B and B'. Vectors **OA** and **OB** determine, respectively, the chiral vector $\mathbf{C}_h$ and the translation vector **T** of the nanotube. The rectangle $OAB'B$ determines the unit cell with the number of atoms N for the particular nanotube. The figure corresponds to $\mathbf{C}_h$ = (6, 2), **T** = (–2, 6), and N = 120. A fragment of the modeled SiO_2 layer (5 × 6 cells) is shown on the left side. The oxygen atoms arranged along $\mathbf{a}_1$ (O(○)) come out of the layer of Si atoms forward, and those arranged along $\mathbf{a}_2$ (O(●)) come out of the layer of Si atoms backward.

0021-3640/04/8010-0628$26.00 © 2004 MAIK "Nauka/Interperiodica"

plane, and the oxygen atoms that come out of the plane forward (O(○)) or backward (O(●)) are located on lines parallel to the $\mathbf{a_1}$ or $\mathbf{a_2}$ unit vectors, respectively. In this perfect model, the tube diameter is tightly related to the lattice constant (a, the distance between the nearest Si atoms) and to the numbers (n, m) (chiral vector $\mathbf{C}_h$) similarly into the model for carbon nanotubes [8]:

$$D_t = L/\pi, \quad L = |\mathbf{C}_h| = a\sqrt{n^2 + m^2}, \tag{1a}$$

$$\mathbf{C}_h = n\mathbf{a}_1 + m\mathbf{a}_2 \equiv (n, m)$$
(n and m are integer numbers); (1b)

$$\cos\theta = \mathbf{C}_h \cdot \mathbf{a}_2/|\mathbf{C}_h||\mathbf{a}_2| = m/(\sqrt{n^2 + m^2}); \tag{1c}$$

$$\mathbf{T} = -m\mathbf{a}_1 + n\mathbf{a}_2 \equiv (-m, n). \tag{1d}$$

The chiral angle θ determines the helical symmetry of the nanotube. The translation vector **T**, determined as a unit vector of the nanotube under consideration, is parallel to its axis and normal to the $\mathbf{C}_h$ vector in the nonrolled rectangular lattice in Fig. 1.

Similarly to dichalcogenide tubes [4], the MO_2 nanotubes are formed from three cylinders: the O(○) atoms are located on the outer cylinder and the O(●) atoms are located on the inner cylinder with respect to the median cylinder with silicon atoms (Fig. 2). Because nanotubes differing in diameter and structure differ in curvature, the distances between these cylinders somewhat vary and the diameters of the middle cylinder somewhat differ from the diameter (Eq. (1a)) of the perfect model. The MO_2 nanotubes can be divided by the main symmetry differences into nonchiral (n, 0) and (0, n) tubes and chiral (n, m) tubes (Table 1). These tubes differ from the previously studied nanotubes composed of hexagonal layers [5–8]: in their case, the (n, 0) tubes do not coincide with the (0, n) tubes, the (n, m) tubes do not coincide with the (m, n) tubes, and the (n, n) tubes are chiral. For the SiO_2 and SnO_2 materials under consideration, the layer deformation is significant (compare with diboride nanotubes [7]), which leads to a dependence of the strain energy on the tube diameter differing from a $1/D^2$ behavior (Table 2).

Note that mixed nanotubes can also exist that can be obtained from layers with a changed arrangement of the O(○) and O(●) atoms by layers or even with a disordered arrangement of MO_4 tetrahedra in a layer. These layers can form nonchiral nanotubes that have a polygonal (triangular, square, etc., see Fig. 3) rather than a circular shape in the cross-section. In this case, these nanotubes must have strips of atoms alternating according to the D_{Nh} (N = 2, 3, 4, etc.) symmetry with a change in the arrangement of the rows. These tubes will be considered in more detail in the subsequent paper.

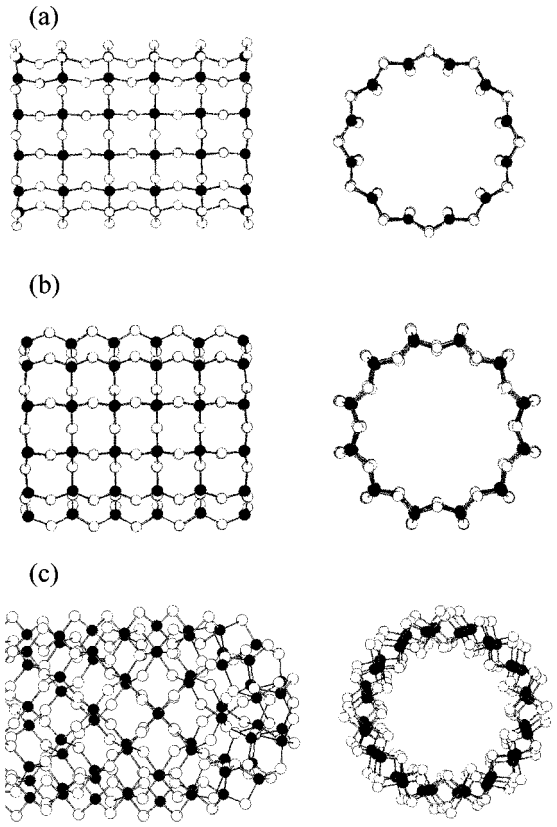

Fig. 2. Models of SiO_2 nanotubes: (a) (12, 0) and (b) (0, 12) (the fragments were calculated by the PM3 method) and (c) (8, 8) tubes "capped" by half of the $(SiO_2)_{72}$ fullerene (the fragment was calculated by the MM+ method.

Table 1. Types of MO_2 nanotubes

Type	θ	C_h	Note
○-Line	0°	(n, 0)	O(○)–Si bonds along generating lines
●-Line	90°	(0, n)	O(●)–Si bonds along generating lines
Chiral cog	45°	(n, n)	Special position
Chiral	0° < θ < 45°	(n, $m < n$)	General position
	45° < θ < 90°	(n, $m > n$)	
Mixed (triangular, square, etc.)	0°, 90°; 0° < θ < 90°	(n, 0), (0, n); (n, m)	Displacement of lines of O(○)–Si and O(●)–Si bonds

Table 2. Main energy characteristics of MO_2 nanotubes

SiO_2	MM + *E* Kcal	*N* (number of atoms)	MM + *E*/*N* Kcal	PM3 *E* Kcal	PM3 *E*/*N* Kcal
layer (7 × 7)	−90.44	208	−0.43481	28050	134.86
n, *m*					
0.12	1667.2	228	7.312	30830.8	135.22
7.0	84.126	252	0.632		
8.0	75.14	152	0.494		
9.0	68.389	171	0.400		
10.0	75.05	190	0.395	27673.6	145.65
11.0	87.55	209	0.419		
12.0	99.9	228	0.438	33042.8	144.92
13.0	112	247	0.453		
14.0	128.62	266	0.484		
15.0	146.96	285	0.516		
16.0	166.267	304	0.547		
17.0	186.51	323	0.577		
18.0	207.51	342	0.607		
19.0	261.676	361	0.725		
20.0	231.98	380	0.610		
22.0	177.7	418	0.425		
24.0	128.9	456	0.283		
2.0	106.12	475	0.223		
5.5	535.38	160	3.346	21940	137.125
6.6	410.85	192	2.140	26452	137.32
7.7	309.7	224	1.383		
8.8	231.446	256	0.904	38461.5	150.24
9.9	167.4	288	0.581		
10.10	120.39	320	0.376		
12.12	22.98	384	0.060		
C10.10@					
(17, 17)	–807.673	1004	−0.804		
C10.10@					
(23, 0)	−458.933	897	−0.512		
C10.10@					
(24, 0)	−444.356	916	−0.485		
SnO_2					
layer (8 × 8)	−405.98	348	–1.167		
n, *m*					
2.0; 2.0 × 3	–72.29	228	−0.317		
0.25	−446.08	475	−0.939		
25.0	−64.64	475	−0.136		
18.18	−496.338	522	−0.951		

Note: The strain energies (E_{strain}) were obtained by the MM+ method; the total energies of the nanotubes (*E*) were obtained by the PM3 method. The value $E_{strain} = 0$ relates to the energy of an unstrained planar graphite sheet (graphene).

Energy characteristics of MO_2 nanotubes. The optimum geometry was calculated for tube fragments of the same length (six unit cells for nonchiral (n, 0) and (0, n) tubes and six cells for the fragment of the layer used to construct a (n, n) tube; hydrogen atoms were placed at the fragment ends) using the molecular dynamics method with the MM+ parametrization and the semiempirical quantum chemical PM3 method, which were used previously, for example, for calculations of the structure of carbon and diboride fullerenes [7, 8] and $(SiO_2)_N$ clusters (N = 6–12) [4]. Note that the calculations of the total energy (E) and E_{strain} for carbon nanotubes and fullerenes using the same program give values close to the results of pseudopotential calculations for single-wall nanotubes (SWNT) and fullerenes [8]. For a fragment of 7×7 cells of the SiO_2 layer, the PM3 calculation gives the bulk energy E equal to –18.9 eV/SiO_2, which is rather close to the value of –19.2 eV/SiO_2 experimentally measured for α-quartz [9], whereas the DFT calculation gives E = –22.4 eV/SiO_2 [10].

The effects of atomic relaxation lead to corrugation of the cylindrical BN (or MgB_2) surface, which leads in its turn to a more stable surface configuration [6, 7]. For the MO_2 nanotubes, the atomic relaxation effects are also exhibited, because the fragment of the MO_2 layer has the optimum shape of a "saddle" rather than plane, as distinct from the graphite layer. Therefore, the chiral tubes of a zigzag (n, n) type turn out to be more stable (see Table 2). The (n, 0) tubes have a minimum strain energy at a certain diameter D_o (in the case of SiO_2, D_o (Si cylinder) = 10.88 Å for the (10, 0) tube). This distinguishes these tubes from single-wall nanotubes with a hexagonal lattice, where $E_{strain}(D) \sim 1/D^2$ [5]. On the other hand, the strain energy $E_{strain}(D) \sim 1/D^2$ for (n, n) nanotubes (D(8, 8) = 9.95 Å, see Fig. 2). With increasing diameter, the Si–Si distance and the configuration of SiO_4 tetrahedra in the limit of a large diameter tend to the value calculated for the SiO_2 layer a = Si–Si ≈ 2.9 Å (Si–O = 1.675 Å). The tube parameters are selected from the geometry of the central cell of the calculated fragment: for example, in the case of SnO_2, the layer parameters are a = Sn–Sn ≈ 3.37 Å, Sn–O ≈ 2.06 Å, and, for the (12, 0) nanotube, the Sn–O and Sn–Sn distances and the O–Sn–O angle are –2.068, 3.378, and 93.9° by a circle and 3.641, 2.063, and 109.1° by a generating line.

The deformation energy is minimal for nanotubes where the M atom and four O atoms nearest to it form a configuration closest to tetrahedral. Thus, the zigzag nanotubes are most stable, followed by the (9, 0)–(12, 0) nanotubes with the inner cylinder of O(●) atoms located in lines parallel to the tube axis (see Table 2). Hence, preferable growth of zigzag-type tubelenes should be expected in the course of the synthesis of MO_2 nanotubes, as well as for BN nanotubes [6].

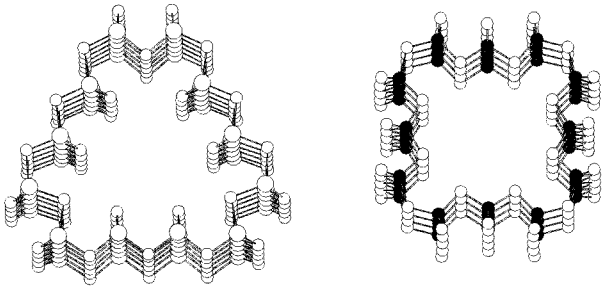

Fig. 3. Models of a "triangular" SnO_2 (2, 0; 2, 0×3) nanotube (on the left) and a "square" SiO_2 (2, 0; 1, 0×4) nanotube (on the right).

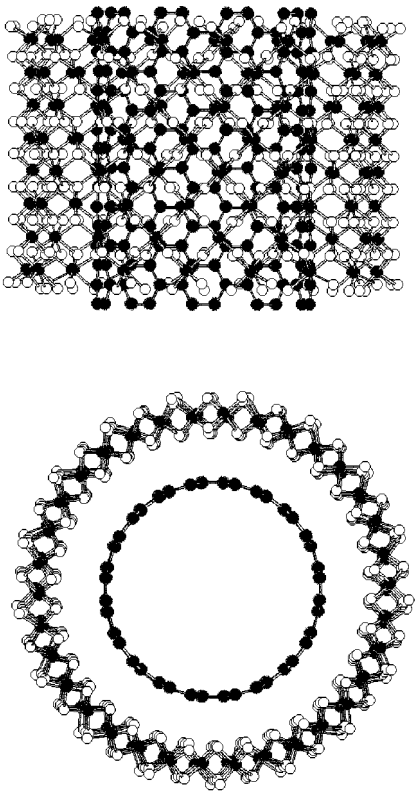

Fig. 4. Models of a double C(10, 10)@SiO_2(17, 17) nanotube.

How can such nanotubes be obtained? The simplest method is to use known nanotubes, for example, carbon ones as templates, as has been done for the formation of nanotubes from boron nitride [6]. Therefore, we modeled a "double" nanotube (Fig. 4) consisting of a single-layer CNT molecularly connected with an SiO_2 nanotube bonded to it and found that the double nanotube possesses a considerably lower strain energy than the SWNT (Table 2), thus, obtaining evidence for the pos-

sibility of this synthesis. The same result can be accomplished through the use of Si nanowires [11] or nanoporous materials [12]. Note that the presence of oxygen at the nanotube ends gives a more energy-stable configuration of the nanotube fragment than the presence of hydrogen. Therefore, it might be suggested that the presence of oxygen during the synthesis of the dioxide nanotubes under consideration would favor their growth.

Why are the MO_2 nanotubes considered above attractive for physical and chemical investigations and for practical applications? First of all, because of their dielectric properties. Because of the occurrence of a rotational symmetry axis, the MO_2 ($n \neq 0$, $m \neq 0$) nanotubes must exhibit piezoelectric properties (as, for example, for quartz crystals). These materials can possess unusual optical properties, so it will be possible to use them as photonic structures. They can also serve as springs and mechanoelectrical elements in micromachines and as building blocks for new nanomaterials. It will be possible to obtain the proposed nanotube structures by the known methods for obtaining nanotubes [1, 5, 6], in particular, by using carbon nanotubes as templates.

This work was performed within the State Scientific and Technical Programs "Atomic Clusters and Fullerenes" and "Low-Dimensional Quantum Structures." The author is grateful to E.G. Gal'pern and, especially, I.V. Stankevich for discussions of the results and to S.V. Lisenkov for indicating works [1–3] that were previously unknown to the author.

REFERENCES

1. R. Tenne and A. K. Zettl, in *Carbon Nanotubes: Synthesis, Structure, Properties, and Applications*, Ed. by M. S. Dresselhaus, G. Dresselhaus, and Ph. Avouris (Springer, Berlin, 2001), Topics in Applied Physics, Vol. 80, p. 55.
2. M. Hervieu, B. Mellune, R. Retoux, *et al.*, Nature Mater. **3**, 269 (2004).
3. S. T. Bromley, Nano Lett. **4**, 1427 (2004).
4. E. Flikkema and S. T. Bromley, J. Phys. Chem. B **108**, 9638 (2004).
5. J. Charlier and S. Iijima, in *Carbon Nanotubes: Synthesis, Structure, Properties, and Applications*, Ed. by M. S. Dresselhaus, G. Dresselhaus, and Ph. Avouris (Springer, Berlin, 2001), Topics in Applied Physics, Vol. 80, p. 81.
6. D. Golberg, Y. Bando, P. Dorozhkin, and Z.-C. Dong, MRS Bull. **29**, 38 (2004).
7. L. A. Chernozatonskiĭ, Pis'ma Zh. Éksp. Teor. Fiz. **74**, 369 (2001) [JETP Lett. **74**, 335 (2001)].
8. D. H. Robertson, D. W. Brenner, and J. W. Mintmire, Phys. Rev. B **45**, 12592 (1992).
9. *CRC Handbook of Chemistry and Physics*, 64th ed. (CRC, Boca Raton, FL, 1983).
10. F. Liu, S. H. Garofalini, D. King Smith, and D. Vanderbilt, Phys. Rev. B **49**, 12528 (1994).
11. A. J. Storm, J. H. Chen, X. S. Ling, *et al.*, Nature Mater. **2**, 537 (2003).
12. D. D. D. Ma *et al.*, Science **299**, 1874 (2003).

Translated by A. Bagatur'yants

JETP Letters, Vol. 80, No. 10, 2004, pp. 633–637. Translated from Pis'ma v Zhurnal Éksperimental'noĭ i Teoreticheskoĭ Fiziki, Vol. 80, No. 10, 2004, pp. 737–742.

Optical Third-Harmonic Generation in Coupled Microcavities Based on Porous Silicon

D. G. Gusev*, M. G. Martemyanov, I. V. Soboleva, T. V. Dolgova, A. A. Fedyanin, and O. A. Aktsipetrov**

Department of Physics, Moscow State University, Vorob'evy gory, Moscow, 119992 Russia

** e-mail: denis@shg.ru*

*** e-mail: fedyanin@shg.ru*

Received July 12, 2004; in final form, October 11, 2004

The resonance features of the third-harmonic generation have been observed in 1D coupled microcavities consisting of three Bragg reflectors and two identical half-wave layers of mesoporous silicon. The third-harmonic intensity increases by a factor of about 10^3 in the resonance of fundamental radiation with each of the modes of coupled microcavities. It has been shown that the resonance positions in the angular spectra of the third-harmonic intensity depend on the coupling between microcavities that is determined by the transmission of the intermediate Bragg reflector. In the framework of the transfer-matrix method with nonlinear sources, it has been shown that the basic mechanism of the enhancement of the third-harmonic generation in coupled microcavities based on porous silicon is the constructive interference of the partial third-harmonic waves that are generated by near-surface layers. © *2004 MAIK "Nauka/Interperiodica".*

PACS numbers: 42.65.Ky; 42.70.Qs; 78.67.–n; 78.67.Pt

The nonlinear optics of microstructures with a photonic band gap is one of the fields of modern optics [1]. The simplest object of this class is a Bragg reflector consisting of layers with a thickness of about optical wavelength and periodically alternating refractive indices. The reflection spectrum of the Bragg reflector contains a frequency band that is characterized by a high reflectance and corresponds to the photonic band gap. A microcavity is obtained by doubling the optical thickness of one of the central layers of the Bragg reflector (1D photonic crystal) and has the resonance state of the electromagnetic field, i.e., a mode whose frequency coincides with the center of the photonic band gap. If the optical thicknesses of several layers in the Bragg reflector are changed, the coupled microcavities with several eigenmodes are formed [2]. The simplest coupled microcavity has two identical microcavity layers separated by the intermediate Bragg reflector. Interchange of electromagnetic-field energy between the microcavities, which is determined by the reflectance of the intermediate reflector; removes the degeneration of modes and leads to their frequency–angular splitting, which is a measure of the coupling between the microcavities [3]. The reflection spectrum of such coupled microcavities has two dips in the photonic band gap, which correspond to resonances of incident light with the modes of coupled microcavities [4].

In coupled microcavities, the enhancement of cubic nonlinear optical processes, such as third-harmonic generation, can be observed. The mechanism of such an enhancement, as in the case of the recently observed effect of the enhancement of second-harmonic generation [5], is an increase in the energy density of the fundamental field within the microcavities due to the spatial localization of the fundamental radiation in resonance with one of the modes of the coupled microcavities. This mechanism is predominant in the case of single microcavities [6], where the contribution to the third-harmonic field from the microcavity layer is much larger than the contributions from the Bragg-reflector layers [7]. In coupled microcavities, an additional mechanism of the enhancement of the third-harmonic generation is possible. It is the constructive interference of the third-harmonic waves from microcavity-layer areas. In this case, the intensity of the third harmonic is maximal in the frequency–angular position shifted from the maximum localization of the fundamental field in a sample.

In this work, we present the observation of the resonance enhancement of the optical third-harmonic generation in 1D coupled microcavities based on mesoporous silicon upon the angular tuning of fundamental radiation near their split modes. It is shown that the angular spectrum of the third-harmonic intensity depends on the coupling of microcavities (the reflectance of the intermediate Bragg reflector). The square susceptibility of mesoporous silicon is low, because the initial silicon crystal is centrosymmetric. This excludes the cascade third-harmonic generation in coupled microcavities and enables one to attribute the detected radiation to the direct generation via the cubic susceptibility $\hat{\chi}^{(3)}$ of mesoporous silicon. A mechanism of the

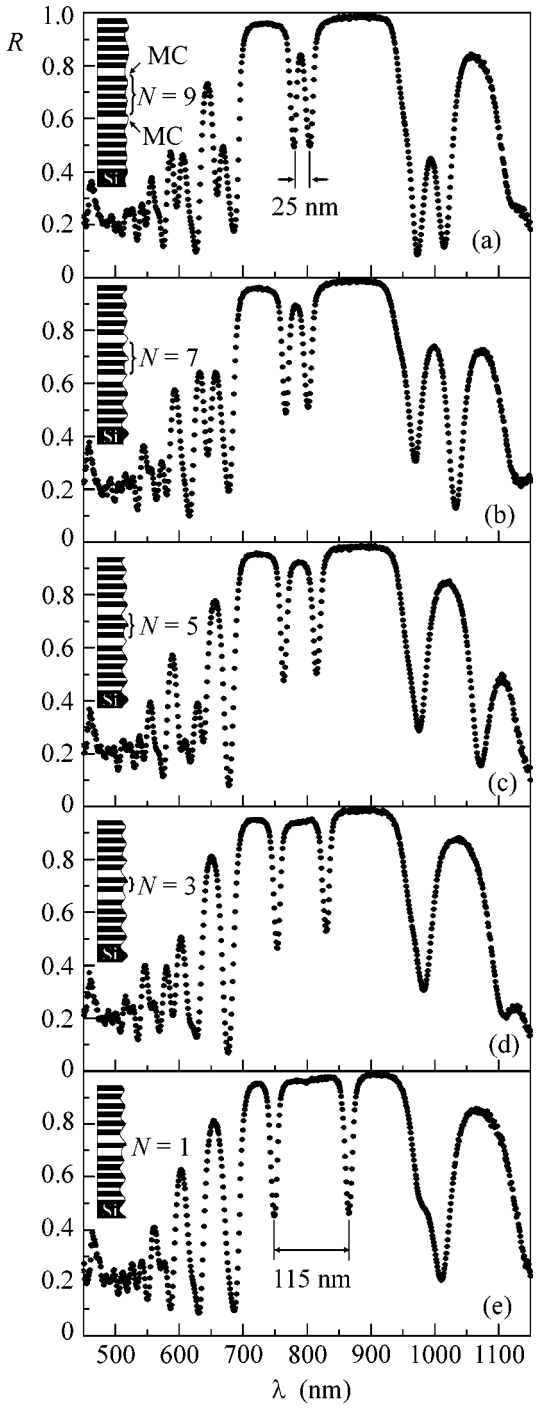

Fig. 1. Reflectance spectra for *s*-polarized radiation from samples of the series of coupled microcavities with N = (a) 9, (b) 7, (c) 5, (d) 3, and (e) 1 for an angle of incidence of 40°. The insets schematically show the structure of coupled microcavities. The white layers correspond to porous silicon with a refractive index of n_L. Microcavity layers are denoted as MC.

enhancement of the third-harmonic generation in the region of the eigenmodes of microcavities is proposed. It is the constructive interference of contributions to the third-harmonic fields from the upper layers. The measured angular spectra of the third-harmonic intensity are approximated using the transfer-matrix method with nonlinear sources in the given fundamental-field approximation.

Coupled microcavities are obtained by electrochemical etching of wafers of highly doped *p*-type silicon (001) with an electrical resistivity of $\rho \sim 6$ mΩ cm in a solution of hydrofluoric acid and ethanol using technology similar to that described in [8]. Samples consist of three distributed reflectors separated by half-wave microcavity layers (insets in Fig. 1). The outer reflectors of the microcavities consist of four pairs of quarter-wave layers (the optical length is equal to $\lambda_0/4$) of mesoporous silicon. The wavelength λ_0 is the center of the photonic band gap upon the normal light incidence. Porous-silicon layers with a high refractive index of $n_H \simeq 1.78$ and a low refractive index of $n_L \simeq 1.42$ are formed by etching with a current density of 6.2 and 20.7 mA/cm^2, respectively. The effective porosities of the layers that are estimated using the reflection spectra of single mesoporous-silicon layers are equal to $f_H \simeq 0.64$ and $f_L \simeq 0.77$ for the high- and low-refractive-index layers, respectively. Cavity layers have a refractive index of $n_{MC} = n_L$. A set of coupled microcavities consists of five samples in which the number N of quarter-wave layers in the intermediate reflector varies from one to nine with a step of two layers.

Figure 1 shows the reflection spectra of coupled microcavities with $\lambda_0 \simeq 850$ nm. The spectra demonstrate the photonic band gap in the wavelength range from 700 to 950 nm with reflectance up to 0.97. When the number of layers in the intermediate reflector changes, the spectral positions of the eigenmodes of the microcavities vary monotonically. With a decrease in N from nine to one, i.e., with an increase in the coupling between microcavities, the spectral splitting Δ of the modes increases from 25 to 115 nm. The dependence of Δ on the intermediate-reflector reflectance R_0, which is determined by the number N of layers, is described by the expression [4]

$$\Delta = \frac{\lambda_0^2}{\alpha n_{MC} \cos\theta_{MC}} \arcsin\sqrt{1 - R_0(\theta_{MC})}, \qquad (1)$$

where α is the length dimension constant determined by the structure of the microcavities and θ_{MC} is the refraction angle in the cavity layers. For large R_0 values, the spectral splitting of modes becomes a root function, i.e., $\Delta \propto (1 - R_0)^{1/2}$.

Experiments on the angular spectroscopy of the third harmonic were conducted with the radiation of a YAG:Nd^{3+} laser generating 1064-nm pulses with a duration of 15 ns and a pulse energy of about 1 mJ. Fundamental radiation polarized in the sample plane (*s* polarization) is directed at an angle of incidence of θ to the normal of the sample. A goniometer ensures the consistent rotation of the sample and detecting system in the incidence-angle range from 15° to 80°. Radiation

reflected in the specular direction passes through a set of UV filters with a total thickness of 12 mm, a diaphragm with an angular aperture of 2.5°, and a Glan prism, which separates the *s* polarized component of the third-harmonic radiation. The third-harmonic signal is detected by a photomultiplier connected with the electronic gated detection system. The angular spectrum of the fundamental-radiation reflectance is measured with the same alignment.

Figure 2 shows the angular spectra of (a) the fundamental-radiation reflectance R and (b) the third-harmonic intensity $I_{3\omega}$ of coupled microcavities with $N = 3$. The angular dependence $I_{3\omega}(\theta)$ exhibits two resonance peaks for the angles of incidence $\theta_2 \simeq 47°$ and $\theta_3 \simeq 69°$, as well as an increase at small angles of incidence, which is indicated as θ_1. The third-harmonic intensities at maxima are approximately equal to each other and are higher than $I_{3\omega}$ in the remaining part of the spectrum by a factor of about 550. The reflectance reaches maxima at the angles of incidence of 24° and 63°, which correspond to the resonance of the incident radiation with each mode of the coupled microcavities. For used refractive indices of porous silicon layers, the range of variation in the angle of incidence θ lies completely within the photonic band gap. The shift of the angular position of the third-harmonic resonances from the modes of the microcavities is observed for all the samples of coupled microcavities. For the sample with $N = 3$, the angular position θ_3 of the right third-harmonic resonance is shifted by 6° from the right dip of the reflectance that corresponds to the long-wavelength mode of microcavities and is denoted as θ_0. The $I_{3\omega}$ peak at $\theta = \theta_3$ is located between the dips in the reflection spectrum at a distance of 16° from θ_0. Such deviation of the positions of the third-harmonic resonances from the modes of coupled microcavities was found for all the samples of the series. In particular, two peaks at $\theta_1 \simeq 25°$ and $\theta_3 \simeq 56°$ are observed in the angular spectrum of the third-harmonic intensity of the coupled microcavities with $N = 7$ (Fig. 3). The amplitude of the right resonance is sevenfold larger than that of the left resonance. In this case, $I_{3\omega}$ for the left and right resonances increases with respect to the remaining part of the spectrum by a factor of 200 and 1500, respectively. The peaks of $I_{3\omega}$ are located on the outer sides of the dips in the angular spectrum of the fundamental-radiation reflectance. The angular positions θ_1 and θ_3 are shifted from the reflectance minima by 4.5° and 9°, respectively.

The fundamental-field amplitude in coupled microcavities reaches a maximum for the angles of incidence that correspond to the minima in the reflectance spectra; i.e., when the fundamental radiation is in resonance with the modes of the microcavities. If the fundamental-field localization inside the microcavities were the only mechanism of enhancement of the third-harmonic generation, the angular positions of the peaks in the third-harmonic intensity would coincide with the positions of the microcavity modes. However, the third-harmonic resonances in the experiment do not coincide with the modes of the coupled microcavities, but they correlate with the change in their angular position with an increase in the coupling between microcavities. For this reason, to interpret the origin of enhancement of the third-harmonic generation, it is also necessary to analyze the behavior of the relative phases of the third-harmonic fields from individual layers of microcavities in the resonance region. The experimental angular spectra and third-harmonic intensity were simultaneously approximated using the transfer-matrix method with nonlinear sources [7, 9]. The electromagnetic fundamental field in each *j*th layer of coupled microcavities is a superposition of two plane waves propagating in the positive and negative directions of the *z* axis coinciding with the normal to the microcavities:

$$\mathbf{E}_j^{\omega}(z,t) = \mathbf{E}_j^{+}\exp[+ik_{z,j}^{\omega}z + (ik_{x,j}^{\omega}x - i\omega t)] + \mathbf{E}_j^{-}\exp[-ik_{z,j}^{\omega}z + (ik_{x,j}^{\omega}x - i\omega t)]. \quad (2)$$

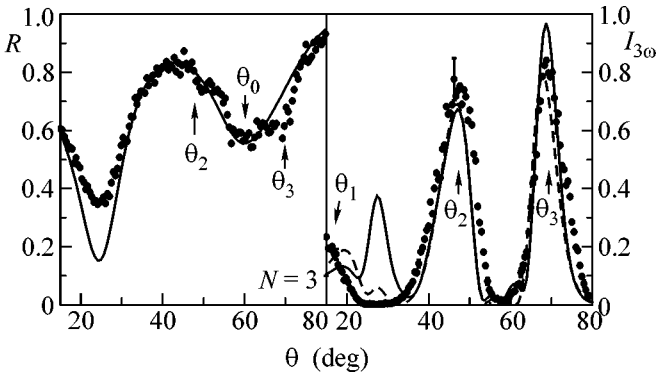

Fig. 2. Angular spectra of the (a) reflectance and (b) third-harmonic intensity of coupled microcavities with $N = 3$ and $\lambda_0 \simeq 1200$ nm. The arrows show the angles of incidence θ_1, θ_2, and θ_3 at which the intensity reaches maxima. The solid lines are the approximations with the identical set of fitting parameters for the whole series of coupled microcavities. The dashed line is the approximation made only for the sample with $N = 3$.

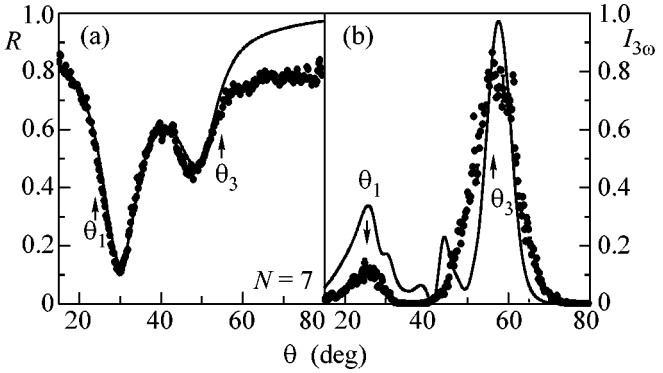

Fig. 3. Angular spectra of the (a) reflectance and (b) third-harmonic intensity of coupled microcavities with $N = 7$ and $\lambda_0 \simeq 1200$ nm. The solid lines are the approximations.

Here, ω is the fundamental-radiation frequency, $k^{\omega}_{z,j} = |\mathbf{k}_j|\cos\theta_j$, $k^{\omega}_{x,j} = |\mathbf{k}_j|\sin\theta_j$, where $\mathbf{k}_j$ is the wave vector and θ_j is the angle of the fundamental-wave refraction in the *j*th layer that is measured from the normal to the surface. The amplitudes of the $\mathbf{E}^{+}_j$ and $\mathbf{E}^{-}_j$ waves are related to the amplitude of the fundamental wave, which is incident on the sample, by the product of the transfer matrices [10] expressing the boundary conditions for the fundamental waves at each interface of the multilayer structure of coupled microcavities. The dipole cubic polarization at the third-harmonic frequency that is induced in the *j*th layers is given by the convolution of the nonzero components of the dipole cubic susceptibility $\hat{\chi}^{(3),j}$ of the layer with the fundamental field:

$$\begin{aligned}\mathbf{P}^{3\omega}_j &= \hat{\chi}^{(3),j}\vdots(\mathbf{E}^{+}_j\exp(ik^{\omega}_{z,j}z) + \mathbf{E}^{-}_j\exp(-ik^{\omega}_{z,j}z))^3 \\ &= \mathbf{P}^{I+}_j\exp(ik^{s,I}_{z,j}z) + \mathbf{P}^{I-}_j\exp(-ik^{s,I}_{z,j}z) \\ &+ \mathbf{P}^{II+}_j\exp(ik^{s,II}_{z,j}z) + \mathbf{P}^{II-}_j\exp(-ik^{s,II}_{z,j}z).\end{aligned} \tag{3}$$

Cubic polarization (3) includes terms of two types. The terms of type *I* are obtained by the convolution of three fundamental waves propagating in the same direction, and the *z* component of their wave vector is equal to $k^{s,I}_{z,j} = 3k^{\omega}_{z,j}$. The terms of type *II* are induced by three fundamental waves, and the *z* component of the wave vector of one of these waves is opposite to the projections of the wave vectors of two other waves. Therefore, $k^{s,II}_{z,j} = k^{\omega}_{z,j}$ for them. The propagation of the inhomogeneous third-harmonic waves induced by cubic polarization is determined by the effective dielectric constant $\epsilon^{I,II}_j$ calculated from the expression $k^{s,I,II}_j = \frac{3\omega}{c}\sqrt{\epsilon^{I,II}_j}$. For the waves of type *I*, $k^{s,I}_j = 3k_{\omega,j} = \frac{3\omega}{c}\sqrt{\epsilon_j(\omega)}$, where ϵ_j is the dielectric constant of the *j*th layer at the fundamental frequency. Then, $\epsilon^{I}_j = \epsilon_j(\omega)$ and the inhomogeneous wave propagates in the medium collinearly to the fundamental wave at an angle of $\theta^I = \theta_j$. Similar calculations for the inhomogeneous wave of type *II* give the expression $\epsilon^{II}_j = \epsilon_j(\omega)(1 + 8\sin^2\theta_j)/9$. The angle between the propagation direction of the inhomogeneous wave of type *II* and the *z* axis differs from θ_j and it is equal to $\theta^{II} = \arctan(3k^{\omega}_x/k^{\omega}_z)$. It is convenient to group the components of the cubic-polarization vector $\mathbf{P}^{I,II}_j = \mathbf{P}^{I,II}_{x,j} + \mathbf{P}^{I,II}_{y,j} + \mathbf{P}^{I,II}_{z,j}$ as

$$\begin{aligned}\mathbf{P}^{I,II}_{\parallel,j} &= \mathbf{P}^{I,II}_{x,j}\sin(\theta^{I,II}) + \mathbf{P}^{I,II}_{z,j}\cos(\theta^{I,II}), \\ \mathbf{P}^{I,II}_{\perp,j} &= \mathbf{P}^{I,II}_{x,j}\cos(\theta^{I,II}) - \mathbf{P}^{I,II}_{z,j}\sin(\theta^{I,II}), \\ &\mathbf{P}^{I,II}_{y,j}.\end{aligned} \tag{4}$$

The *y* axis lies in the layer surface plane, it is perpendicular to the plane of incidence, and the *x* axis is parallel to the plane of incidence. The components $\mathbf{P}_{\parallel}$ and $\mathbf{P}_{\perp}$ in Eqs. (4) are polarized across and along the cubic-polarization wave vector, respectively, and they determine the generation of the *p* polarized third-harmonic wave. The $\mathbf{P}_y$ component is responsible for the generation of the *s* polarized third-harmonic wave. The amplitude of the coupled wave of the third harmonic is given as [11]

$$\begin{aligned}\mathbf{E}^{(s)I,II}_{3\omega,j} &= \frac{4\pi}{\epsilon^{I,II}_j - \epsilon_j(3\omega)}(\mathbf{P}^{I,II}_{y,j} + \mathbf{P}^{I,II}_{\perp,j}) \\ &- \frac{4\pi}{\epsilon_j(3\omega)}\mathbf{P}^{I,II}_{\parallel,j}.\end{aligned} \tag{5}$$

Then, these expressions for the coupled waves are substituted into the modified transfer matrices that express the boundary conditions for the third-harmonic waves at the interface of the layers and take into account the interference between the homogeneous and inhomogeneous waves [9], which makes it possible to determine the partial field $\mathbf{E}^{(j)}_{3\omega}$ of the third harmonic from the *j*th nonlinear layer at the exit from the multilayer structure. The total field of the third harmonic is determined by summing the fields $\mathbf{E}^{(j)}_{3\omega}$ at the exit from the sample taking their phases into account, and the third-harmonic intensity is determined as $I_{3\omega} = \left|\sum_j \mathbf{E}^{(j)}_{3\omega}\right|^2$. Each mesoporous-silicon layer within the microcavities is treated as isotropic in its plane. Then, owing to the symmetry, the cubic polarization generating the *s* polarized radiation of the third harmonic in the presence of the *s* polarized fundamental radiation is determined only by the component $\hat{\chi}^{(3)}_{yyyy}$ [7]. The refractive indices of porous-silicon layers at a frequency of 3ω, whose initial values are calculated using the effective-medium model, are adjustable parameters for the approximation of the experimental spectra $R(\theta)$ and $I_{3\omega}(\theta)$. The refractive indices at the fundamental frequency and the optical thicknesses of the layers are obtained from the calibration of single porous-silicon layers. In addition, a small linear depth modulation of the optical thicknesses is introduced such that the optical thickness of the deepest layer differs from the value for the first layer by about 5%. This modulation expresses the depth dependence of the silicon etching rate [12]. Since the number of fitting parameters is large, the joint approximation of the angular spectra of the reflection and the third-harmonic intensity was conducted with identical values of the fitting parameters for all the samples of coupled microcavities. The quality of the approximation was determined by the minimum of the standard deviation for the entire series of the spectra. This approximation shows good agreement between the model and experimental angular distributions. The model distributions shown in Figs. 2 and 3 for samples with $N = 3$ and 7, respectively, corroborate the existence of the characteristic features in the angular spectra of the third-harmonic generation.

The third-harmonic resonances at θ_1 and θ_3 are located on the outer sides of the dips in the angular spectrum of the reflection, and the angular position of the third-harmonic resonance at θ_2 lies between the microcavity modes. For the sample with $N = 7$, the resonances at θ_2 and θ_3 cannot be separated in the experiment, because the splitting of the modes is small and the Q factor of the microcavities is insufficient. Deviations of the model dependences from the experimental data, e.g., the shift of the third-harmonic resonance at θ_1 for the sample with $N = 3$, and the significant, almost twofold, difference in the amplitudes of the resonance at θ_1 for the sample with $N = 7$ are associated with the chosen approximation procedure, where the identical values of the fitting parameters are used for all the samples. Only the approximation of the angular spectrum of the third harmonic for the sample with $N = 3$ (Fig. 2, dashed line) provides significantly better agreement between the model distribution and the experimental data.

The origin of the third-harmonic resonances can be illustrated in the polar diagrams of the complex amplitudes $E_{3\omega}^{(j)} \equiv \left|\mathbf{E}_{3\omega}^{(j)}\right|$ of the partial third-harmonic fields from each jth layer of coupled microcavities. Figure 4 shows the partial contributions to the third-harmonic field for the sample with $N = 3$ as calculated in the reflectance minimum at $\theta = \theta_0$ and in the third-harmonic maximum at $\theta = \theta_3$. In the exact resonance of the fundamental radiation with a mode of the microcavities, the phases of the partial fields of the third harmonic from the neighboring layers are opposite to each other. Thus, their destructive interference occurs, and the amplitude of the total field of the third harmonic at the exit from the microcavities is small. In a certain angular vicinity of the fundamental–mode resonance, where the fundamental field is still strongly localized but the distribution of the partial-field phases is asymmetric, the partial contributions from neighboring layers do not compensate for each other. At the minimum phase detuning between the partial fields $E_{3\omega}^{(j)}$, their constructive interference occurs and the third-harmonic intensity reaches a maximum. In this case, $E_{3\omega}^{(j)}$ is maximal for the porous-silicon layers near the sample surfaces.

Thus, an increase in the intensity of the third optical harmonic has been found upon the tuning of the fundamental radiation to the frequency–angular vicinity of the eigenmodes of 1D coupled microcavities based on porous silicon. In the framework of the transfer-matrix method with nonlinear sources, it has been shown that the constructive interference between the partial fields of the third harmonic from the upper layers of the microcavities is the basic enhancement mechanism. Such relations between the phases of the third-harmonic waves from the layers of coupled microcavities are determined by the effective dispersion relation at the fundamental-field frequency and mean that the quasi-phase-matching conditions are fulfilled upon the third-harmonic generation in coupled microcavities.

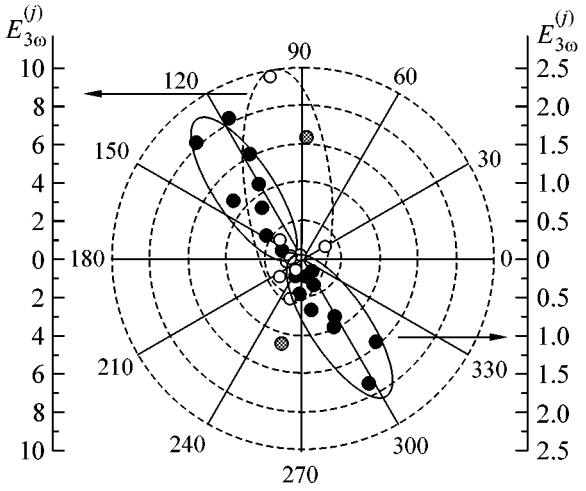

Fig. 4. Partial contributions of individual layers of coupled microcavities to the third-harmonic field as calculated for the angles of incidence corresponding to the (solid circles) mode of coupled microcavities and (open circles) third-harmonic generation resonance. The shaded circles are the contributions from the cavity layers at $\theta = \theta_0$. The ovals are the polar-diagram domains, where the phases of the partial fields of the third harmonic are concentrated.

This work was supported by the Russian Foundation for Basic Research, the Council of the President of the Russian Federation for Support of Young Russian Scientists and Leading Scientific Schools (project no. NSh-1604.2003.2), Deutsche Forschungsgemeinschaft (grant no. 436 RUS 113/640/0-1), NATO (grant no. PST.CLG.979406), and INTAS (grant no. 03-51-3784).

REFERENCES

1. *Nonlinear Photonic Crystals*, Ed. by R. E. Slusher and B. J. Eggleton (Springer, Berlin, 2003).
2. R. P. Stanley, R. Houdre, U. Oesterle, *et al.*, Appl. Phys. Lett. **65**, 2093 (1994).
3. M. Bayindir, C. Kural, and E. Ozbay, J. Opt. A: Pure Appl. Opt. **3**, S184 (2001).
4. L. Pavesi, G. Panzarini, and L. C. Andreani, Phys. Rev. B **58**, 15794 (1998).
5. D. G. Gusev, I. V. Soboleva, M. G. Martemyanov, *et al.*, Phys. Rev. B **68**, 233303 (2003).
6. T. V. Dolgova, A. I. Maĭdykovski, M. G. Martemyanov, *et al.*, Pis'ma Zh. Éksp. Teor. Fiz. **75**, 17 (2002) [JETP Lett. **75**, 15 (2002)].
7. M. G. Martemyanov, T. V. Dolgova, and A. A. Fedyanin, JETP **98**, 463 (2004).
8. O. Bisi, S. Ossicini, and L. Pavesi, Surf. Sci. Rep. **38**, 1 (2000).
9. D. S. Bethune, J. Opt. Soc. Am. B **6**, 910 (1989).
10. A. Yariv and P. Yeh, *Optical Waves in Crystals: Propagation and Control of Laser Radiation* (Wiley, New York, 1984; Mir, Moscow, 1989).
11. N. Bloembergen and P. S. Pershan, Phys. Rev. **128**, 606 (1962).
12. M. Ghulinyan, C. J. Oton, Z. Gaburro, *et al.*, Appl. Phys. Lett. **82**, 1550 (2003).

Translated by R. Tyapaev

JETP Letters, Vol. 80, No. 10, 2004, pp. 638–641. Translated from Pis'ma v Zhurnal Éksperimental'noĭ i Teoreticheskoĭ Fiziki, Vol. 80, No. 10, 2004, pp. 743–747.

Effects of Exchange Interaction in Bilayer Dy_xCo_{1-x}/NiFe Films in the Vicinity of Compensation Compositions of Amorphous DyCo Alloys

R. S. Iskhakov[1, *], V. A. Seredkin[1], S. V. Stolyar[1, 2], G. I. Frolov[1], and V. Yu. Yakovchuk[1]

[1] *Kirenskiĭ Institute of Physics, Siberian Division, Russian Academy of Sciences, Krasnoyarsk, 660036 Russia*

[2] *Krasnoyarsk State University, Krasnoyarsk, 660041 Russia*

* *e-mail: rauf@iph.krasn.ru*

Received September 6, 2004; in final form, October 11, 2004

The displacement field of the hysteresis loop due to exchange anisotropy in planar DyCo/NiFe systems is studied experimentally as a function of the concentration of the rare-earth element. The bilayer DyCo/NiFe film system is characterized by an orthogonal arrangement of the effective magnetizations of separate layers under the condition that the amorphous DyCo layer is prepared in the region of magnetic compensation. An analysis of the dependence of the displacement field on the Dy concentration has led to an understanding of the physical mechanism of the formation of the exchange anisotropy in these planar systems. © *2004 MAIK "Nauka/Interperiodica".*

PACS numbers: 75.47.Np; 78.55.Qr; 78.67.Pt

At present, studies of the effects of the exchange interaction at the boundary between two different magnetic ordered systems are experiencing a kind of renaissance (see, e.g., [1–3]). This fact is, in many respects, due to the development of the technology of obtaining new varieties of composites. Thus, the formation of multilayer films from layers of soft and hard ferromagnets has significantly improved the characteristics of planar permanent magnets [4]. The phenomenon of so-called exchange anisotropy [5] caused by the effects of the exchange interaction at the boundary between a ferromagnet and an antiferromagnet, which manifest themselves in a hysteresis loop shift with respect to the origin of the coordinates, turned out to be useful in spintronics and for the development of numerous sensors [6]. The phenomenological description of these effects is rather simple and is based on the suggestion that the magnetic moments at the boundary of the different phases are collinear: $\mathbf{JM}_1\mathbf{M}_2 = JM_1M_2\cos(M_1\hat{}M_2)$. In this light, the result obtained in [7] seems especially remarkable. In this work, exchange anisotropy was observed in bilayer TbFe/NiFe and DyCo/NiFe film systems characterized by the orthogonal arrangement of the effective magnetizations of separate layers under the condition that the amorphous REE–TM layer was synthesized in the region of magnetic compensation. In these planar systems, the ratio of the displacement field H_E of the hysteresis loop to the coercive field H_c (characterizing this field) attains 1200%, whereas this ratio equals ~200% in the widely used NiFe/NiFeMn system. Such large values of the H_E/H_c ratio suggest that planar (TbFe, DyCo)/NiFe systems can be used in numerous applications (see, e.g., [8]), naturally, under the condition that the physical mechanism of the formation of the exchange anisotropy in these systems is understood.

In our works [9–11], a model of the microheterophase structure of amorphous DyCo alloys was suggested based on the results of measuring the dynamic (and static) magnetic characteristics of these composite systems. The features of the magnetic microstructure of these alloys in the compensation region following from this model allowed a number of experimental results on ferromagnetic resonance (FMR) and spin-wave resonance (SWR). In order to detect these features, we (i) obtained three-layer NiFe/DyCo/NiFe film structures with magnetic anisotropy and an orthogonal orientation of the effective magnetizations of the layers, (ii) studied the FMR and SWR spectra of such structures, and (iii) found that the spin system of amorphous DyCo alloys in the concentration region of the magnetic compensation can be presented as two subsystems such that the magnetization of the TM sublattice dominates in one of them (magnetic nanophase Φ_1) and the magnetization of the REE sublattice dominates in the other (magnetic nanophase Φ_2).

The goal of this work is to demonstrate that the effects of the hysteresis loop shift in planar DyCo/NiFe systems can be explained using this model within the framework of conventional notions.

Actually, the model proposed reflects the main property of the structure of amorphous alloys, namely, their

natural fluctuation (topological and compositional) heterogeneity. It is known that chemical (phase) nanoscale heterogeneities exist in amorphous alloys. The magnitude of the concentration fluctuations on these scales can reach several atomic percent of the average concentration. Therefore, the magnetic microstructure of amorphous ferrimagnetics in the concentration region $x_i \pm \Delta x(r) \ll x_{comp}$, $x_i \pm \Delta x(r) \gg x_{comp}$ will significantly differ from the magnetic microstructure in the concentration region $x_i - \Delta x < x_{comp} < x_i + \Delta x$. The magnetic compensation point x_{comp} itself will be determined in this case by the condition $\langle M \rangle = p\mathbf{M}_{eff}^{(\Phi 1)} + q\mathbf{M}_{eff}^{(\Phi 2)} = 0$, where p and q are the volume fractions of the Φ_1 and Φ_2 nanophases and $\mathbf{M}_{eff}^{(\Phi 1)}$ and $\mathbf{M}_{eff}^{(\Phi 2)}$ are their effective magnetizations at $x_i - \Delta x$ and $x_i + \Delta x$, respectively.

To accomplish this goal, we carried out investigations on the quasistatic magnetization reversal of planar Dy_xCo_{1-x}/NiFe structures at various concentrations x_i of the RE element. It was found that the features of the concentration dependences of the displacement field H_E of the hysteresis loop not only were well described within the framework of the model proposed above but also allowed the value of some parameters of this model to be estimated.

SAMPLE PREPARATION AND EXPERIMENTAL PROCEDURE

Bilayer exchange-coupled $Ni_{80}Fe_{20}/Dy_xCo_{1-x}$ films were obtained by thermal evaporation in a vacuum of 3×10^{-6} Torr by successively sputtering the NiFe and DyCo layers from independent evaporators with a ring cathode onto cover-glass substrates. The thickness of the permalloy layer in the planar system was varied from 40 to 300 nm, and the thickness of the DyCo layer, from 10 to 80 nm. Single-layer Dy_xCo_{1-x} films 70 nm thick were used as reference samples. The amorphous state of DyCo was monitored by electron microscopy, and the thickness and chemical composition of the layers, by x-ray spectroscopic analysis. The following experimental techniques were used: magneto-optical Kerr effect measurements in fields up to 15 kOe, a torque magnetometer in fields up to 12 kOe, and a loop meter with fields up to 250 Oe (applied in the film plane) at the frequency $f = 50$ Hz. The main magnetic characteristics of the reference Dy_xCo_{1-x} films were studied in the Dy concentration region from 17 to 30 at. % (see Fig. 1). The dependences measured indicate that the compensation composition, in our case, is the $Dy_{22}Co_{78}$ alloy. The measurement results also show that the effective magnetization in these films is orthogonal to the plane. This is indicated by the absence of a magneto-optical signal in fields up to 15 kOe at fields oriented in the film plane, the detection of the hysteresis loop with the use of the polar Kerr effect (caused by the normal magnetization component), and the inversion of the

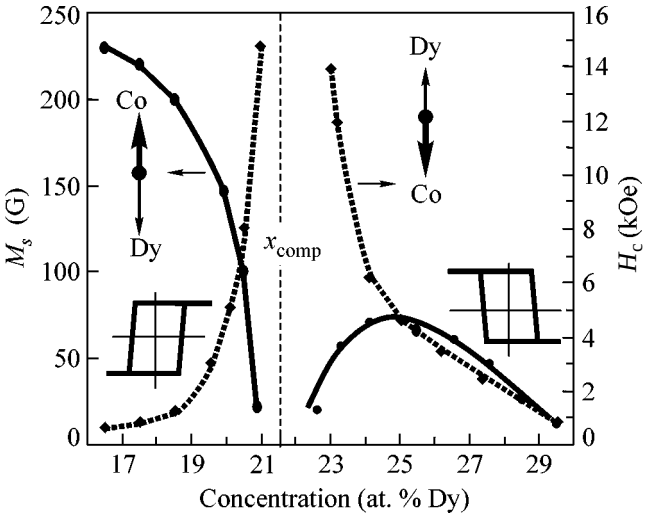

Fig. 1. Concentration dependence of the effective saturation magnetization M_s and the coercive force H_c of amorphous ferrimagnetic Dy_xCo_{1-x} films. The inversion of the form of the magneto-optical signal loop points to the orthogonal orientation of the effective magnetization.

form of the hysteresis loop (see Fig. 1). Measurements on the torque magnetometer allowed the uniaxial anisotropy constant to be evaluated. It was found to be 5×10^{-5}–10^{-6} erg/cm^3 for DyCo films in the concentration region 17–30 at. % Dy, which substantially exceeded the values of $2\pi M_s^2$ presented in Fig. 1. The main magnetic characteristics of the bilayer film structures were also measured as functions of the REE concentration, the thickness of the NiFe layer, and the temperature [12]. Below, as reference values, we will present the results of measuring the hysteresis loop shift field for two series of planar structure samples: substrate/ferrimagnetic Dy_xCo_{1-x} layer (70 nm)/ferromagnetic NiFe layer (150 nm) and substrate/ferromagnetic NiFe layer (150 nm)/ferrimagnetic Dy_xCo_{1-x} layer (70 nm). The ferrimagnetic layer of amorphous DyCo was synthesized with a perpendicular magnetic anisotropy (see Fig. 1), and the ferromagnetic NiFe layer was manufactured with a magnetization in the sample plane oriented along the uniaxial anisotropy (the field $H_k = 7$–8 Oe). This magnetization was formed by applying a constant external magnetic field $H_0 = 50$ Oe in the film plane.

RESULTS AND DISCUSSION

Experimental dependences of the displacement field H_E of the hysteresis loop on the REE concentration in the planar DyCo/NiFe structure and schematic diagrams of the distribution of the Φ_1 and Φ_2 nanophases in the DyCo layer are presented in Fig. 2. The analogous dependence $H_E(x)$ and analogous schematic diagrams for the planar NiFe/DyCo structure are presented

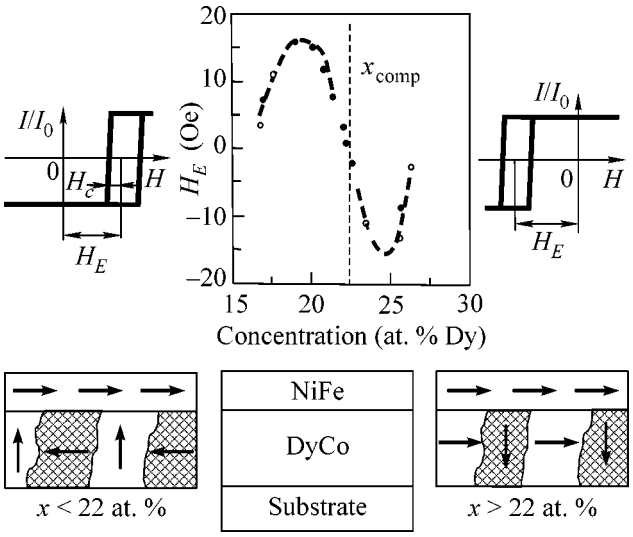

Fig. 2. Hysteresis loops and concentration dependence of the displacement field $H_E(x)$ in exchange-coupled DyCo/NiFe film structures. The schematic diagram presents the orientations of the magnetization vectors of the 3*d* metals of the structures under consideration. In the DyCo layer, the Φ_2 phase ($M_{Co} < M_{Dy}$) is hatched and the Φ_1 phase ($M_{Co} > M_{Dy}$) is not.

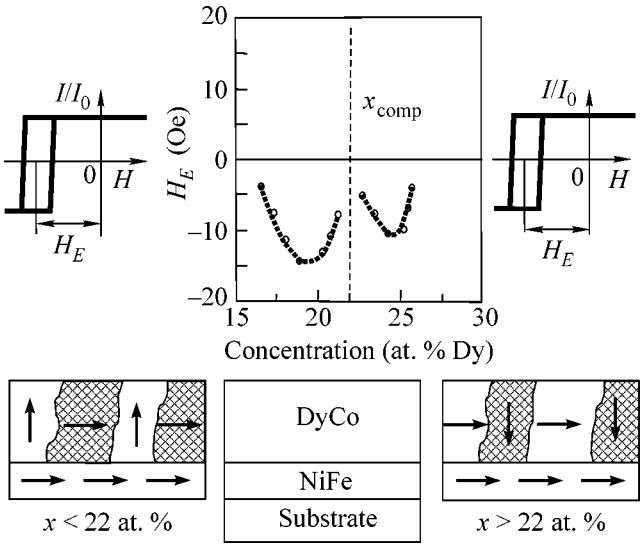

Fig. 3. Hysteresis loops and concentration dependence of the displacement field $H_E(x)$ in exchange-coupled NiFe/DyCo film structures. The schematic diagram presents the orientations of the magnetization vectors of the 3*d* metals of the structures under consideration. In the DyCo layer, the Φ_2 phase ($M_{Co} < M_{Dy}$) is hatched and the Φ_1 phase ($M_{Co} > M_{Dy}$) is not.

in Fig. 3. (The coercive field H_c of the NiFe layer at a selected thickness of 150 nm was 2 Oe and did not depend on either the Dy concentration or the sequence of the layer sputtering.) Let us discuss the similarity and distinction of the presented experimental dependences $H_E(x)$.

In the presented figures, it is evident that the $H_E(x)$ curves are described by different functions, depending on the sequence in which the layers are sputtered: $H_E(x - x_{comp})$ is an antisymmetric function for the Dy_xCo_{1-x}/NiFe films (see Fig. 2), and $H_E(x - x_{comp})$ is a symmetric function for the NiFe/Dy_xCo_{1-x} films (see Fig. 3). However, the singular points of these functions (coordinates of zeros and extremum points) are independent of the sequence of layer sputtering. It is evident that the hysteresis loop shift along the field axis is absent ($H_E = 0$) at $x = x_{comp}$, $x \le 16$ at. % Dy, $x \ge 27$ at. % Dy in both cases. It is also seen that the displacement fields H_E reach maximum values in these planar structures at $x \approx 19$ at. % for precompensation DyCo compositions and at $x \approx 24$ at. % for postcompensation DyCo compositions.

The results of our experiment are naturally interpreted within the framework of the model of the structure of amorphous DyCo alloys in the region of magnetic compensation proposed in [10] and described at the beginning of this article and also within the framework of the schematic diagrams presented in Figs. 2 and 3. (The arrows here indicate the possible orientation of the magnetization of the 3*d* metals.) Actually, in the range of the REE–TM concentrations $x \le 16$ at. % ($x \ge 27$ at. %), the magnetic structure of amorphous DyCo is unambiguously attributed to the magnetic Φ_1 (Φ_2) nanophase. Hence, the magnetic moments of the Co sublattice and the Dy sublattice are collinear with the axis perpendicular to the DyCo layer anisotropy, and the effective magnetization vectors of the DyCo and NiFe vectors are mutually orthogonal, which means that magnetic coupling is absent here. A different situation occurs in the concentration region $x_i - \Delta x < x_{comp} < x_i + \Delta x$. Here, the magnetic structure of the DyCo layer is formed by the randomly mixed Φ_1 and Φ_2 nanophases. If the Φ_1 phase belongs to the matrix, the Φ_2 phase is the impurity phase (if Φ_2 is the matrix phase, Φ_1 is the impurity phase). An exception is the compensation point x_{comp}, where the volume fractions of the Φ_1 and Φ_2 nanophases are approximately equal.

For all the concentrations x_i in this region, the effective magnetization of the matrix Φ_i phase in the DyCo layer is aligned with the perpendicular anisotropy field (M_{Co} and M_{Dy} are collinear with this axis, which is detected by the polar Kerr effect). In this case, the magnetization M_{Co} in the impurity Φ_j phase must have an in-plane component because of the strong exchange interaction of the transition elements in the impurity and matrix phases, and the effective magnetization of the Φ_j nanophase gains the possibility of orienting itself along the external field. In our opinion, it is the exchange interaction of M_{Co} in the DyCo layer of the impurity Φ_j phase with the magnetization of the NiFe layer that leads to the exchange anisotropy of NiFe. The

magnitude of this exchange anisotropy, which is characterized by the value of H_E, will be determined by the product of M_{Co} in the impurity Φ_j phase and the area of its contact with the NiFe layer. It is evident from the data presented in Figs. 2 and 3 that this product reaches optimum values at 19 at. % Dy and 24 at. % Dy. At 19 at. % < x < x_{comp} (x_{comp} < x < 24 at. %), the area of the impurity Φ_j phase contact with the NiFe layer continues to grow, but the decrease in H_E indicates that the projection of the magnetization of the Co sublattice onto the plane of the NiFe layer decreases. Finally, at x_{comp}, it follows from the experimental result $H_E = 0$ that the mean value of the projection of the magnetization of the Co sublattices onto the plane of the NiFe layer equals zero, which points to the collinearity of M_{Co} and M_{Dy} with the axis of perpendicular anisotropy.

As the concentration x_i increases (16 at. % < x_i < x_{comp}), the morphology of the impurity phase changes: disperse inclusions appear, the number of these disperse inclusions increases, percolation over the disperse inclusions arises, the volume of the formed infinite cluster increases, etc. Therefore, it is natural to associate the singular points of the $H_E(x)$ dependence with the characteristics of this morphological series. In our opinion, the maximum values of H_E correspond to the establishment of percolation over disperse inclusions. Thus, the singular points of the $H_E(x)$ dependences gain an appropriate description within the framework of the proposed model. Also, note that the $H_E(x)$ dependences allow the amplitudes of the concentration fluctuations in DyCo to be evaluated. For example, $|\Delta x| \geq 4$ at. % Dy in the precompensation amorphous DyCo alloy, and $|x| \geq 3$ at. % Dy in the postcompensation amorphous DyCo alloy (see Figs. 2, 3).

Let us show now that the form of these dependences (antisymmetric or symmetric with respect to x_{comp}) is naturally interpreted within the framework of the proposed model. Consider the antisymmetric dependence $H_E(x - x_{comp})$ presented in Fig. 2 and obtained for planar Dy_xCo_{1-x}/NiFe systems. First, the Dy_xCo_{1-x} layer in which the effective magnetization of the main phase is oriented along the perpendicular magnetic anisotropy axis is formed in these planar systems, and the effective magnetization of the impurity phase is oriented in the layer plane. Upon the synthesis of the NiFe layer, a constant field is switched on, and the effective magnetization of the impurity phase in the Dy_xCo_{1-x} layer is oriented along the direction of this field and, hence, along the anisotropy axis formed in NiFe. However, the impurity phase is characterized by the inequality $M_{Co} < M_{Dy}$ in the region $x < x_{comp}$ and by the inequality $M_{Co} > M_{Dy}$ in the region $x > x_{comp}$. The latter means that the magnetization vectors of the Co sublattice and the NiFe layer are anticollinear in the region $x < x_{comp}$, whereas these vectors are unidirectional in the region $x > x_{comp}$ (see the scheme in Fig. 2). It is due to this fact that the displacement field H_E changes its sign at the concentration transition through x_{comp}. The situation is different for the planar NiFe/Dy_xCo_{1-x} system. First, the NiFe layer is formed, in which the external field not only forms uniaxial anisotropy but also determines the direction of the layer magnetization. Next, the field is switched off, and the Dy_xCo_{1-x} layer is synthesized. In this case, only the "exchange field" from the magnetization of the NiFe layer exerts an orienting action on the magnetic moments of the Co sublattice of the impurity phase. Therefore, regardless of the composition of the Dy_xCo_{1-x} layer, the magnetization M_{Co} of the impurity phase and the magnetization of the NiFe layer have the same direction. The latter means that the displacement field H_E will not change its sign when the concentration passes through x_{comp}, which is confirmed by the experimental results (see Fig. 3).

Thus, the physical mechanism of the formation of the exchange anisotropy in bilayer DyCo(TbFe)/NiFe film systems with the orthogonal arrangement of the effective magnetizations of separate layers has been understood in the course of the performed studies. The REE concentrations in the ferrimagnetic layers have been found at which the maximum exchange anisotropy acts on the ferromagnetic layers.

This work was supported by the Russian Foundation for Basic Research, project no. 04-02-16099-a.

REFERENCES

1. J. Nogues and I. K. Schuller, J. Magn. Magn. Mater. **192**, 203 (1999).
2. A. E. Berkowitz and K. Takano, J. Magn. Magn. Mater. **200**, 552 (1999).
3. P. Grunberg, Acta Mater. **48**, 239 (2000).
4. M. E. McHenry and D. E. Laughlin, Acta Mater. **48**, 223 (2000).
5. W. H. Meiklejohn and C. P. Bean, Phys. Rev. **105**, 904 (1957).
6. R. Jansen, J. Phys. D: Appl. Phys. **36**, R289 (2003).
7. V. A. Seredkin, G. I. Frolov, and V. Yu. Yakovchuk, Pis'ma Zh. Tekh. Fiz. **9** (23), 1446 (1983) [Sov. Tech. Phys. Lett. **9**, 621 (1983)].
8. V. A. Seredkin, S. V. Stolyar, G. I. Frolov, and V. Yu. Yakovchuk, Pis'ma Zh. Tekh. Fiz. **30** (10), 46 (2004) [Tech. Phys. Lett. **30**, 820 (2004)].
9. R. S. Iskhakov, V. Yu. Yakovchuk, S. V. Stolyar, *et al.*, Fiz. Tverd. Tela (St. Petersburg) **43**, 1462 (2001) [Phys. Solid State **43**, 1522 (2001)].
10. R. S. Iskhakov, V. A. Sederkin, S. V. Stolyar, *et al.*, Pis'ma Zh. Éksp. Teor. Fiz. **76**, 779 (2002) [JETP Lett. **76**, 656 (2002)].
11. V. A. Seredkin, R. S. Iskhakov, V. Yu. Yakovchuk, *et al.*, Fiz. Tverd. Tela (St. Petersburg) **45**, 883 (2003) [Phys. Solid State **45**, 927 (2003)].
12. V. Yu. Yakovchuk, Candidate's Dissertation (Krasnoyarsk, 2003).

Translated by A. Bagatur'yants

JETP Letters, Vol. 80, No. 10, 2004, pp. 642–645. Translated from Pis'ma v Zhurnal Éksperimental'noĭ i Teoreticheskoĭ Fiziki, Vol. 80, No. 10, 2004, pp. 748–751.

Observation of the Time Variation of the Magnetic-Field-Induced Polarization of Triplet Exciton Emission in GaSe

A. N. Starukhin, B. S. Razbirin, and A. S. Yakunenkov

Ioffe Physicotechnical Institute, Russian Academy of Sciences, St. Petersburg, 194021 Russia

Received October 11, 2004

The magnetic-field-induced linear polarization of the triplet bound-exciton emission has been studied by means of time-resolved spectroscopy in uniaxial GaSe crystals under unpolarized pumping conditions. It is found that the magnetic-field dependence of the linear-polarization degree of the exciton luminescence varies during the lifetime of the excited state. The degree of polarization significantly increases with increasing the delay of the emission measurement. For delay times $t > 1$ μs, the exciton emission in the applied magnetic field is virtually completely polarized. A theoretical description is proposed for the observed time variation of the magnetic-field-induced polarization of the triplet bound-exciton emission. © *2004 MAIK "Nauka/Interperiodica".*

PACS numbers: 71.35.Ji; 78.20.Ls; 78.47.+p; 78.55.Hx

The method of polarized luminescence has been widely used in investigations of the properties of electronic states in various atomic systems, including exciton spectroscopy [1, 2]. When light propagates along the principal (optical) axis of a uniaxial crystal, all the polarization states are equivalent and the polarized luminescence appears only if the crystal is subjected to an external anisotropic action (polarized excitation, an external magnetic field, etc.). In particular, a magnetic field applied perpendicularly to the optical axis of the crystal reduces the symmetry of the system and may induce polarized luminescence from the crystal even under unpolarized pumping conditions.

In the case of exciton luminescence, this phenomenon (not attributed to exciton thermalization between various Zeeman sublevels) was observed in hexagonal GaSe crystals [3]. Under continuous excitation conditions for a crystal [3], the degree of radiation polarization is averaged over the lifetime of the excited state. In this case, the degree of polarization and its dependence on the magnetic field at various times remain unknown.

The aim of this study was to use time-resolved spectroscopy for determining the degree of linear polarization of the exciton emission in a GaSe crystal as a function of the transverse magnetic field at various moments of the exciton lifetime.

EXPERIMENTAL METHOD

The experiments were performed on Bridgman-grown GaSe crystals that were not doped intentionally. The samples were cleaved from the ingot by cleavage along the crystal planes perpendicular to the optical axis c. The exciton luminescence was excited by the radiation of a pulsed copper-vapor laser with a pulse duration of $\tau_p = 20$ ns. The excitation density was about 200 W/cm^2. The exciting photons with the energy $h\nu_{exc} = 2.140$ eV (exceeding the bandgap width E_g of the crystal) were incident at a small angle relative to the normal to the sample surface. The emitted light (exciton luminescence) was detected along the normal, that is, in the direction parallel to the optical axis of the crystal. The luminescence spectra were recorded using a grating spectrometer equipped with a photon counting system with a time resolution of ~30 ns. In order to study the emission at various moments of the exciton lifetime, the detection gate pulse of the photon counting system was delayed relative to the excitation pulse. During the experiment, the sample, immersed in liquid helium, was at a temperature of 2 K. The external magnetic field was generated by a superconducting coil and oriented perpendicularly to the optical axis c.

EXPERIMENTAL RESULTS AND DISCUSSION

Figure 1 shows the typical spectrum of emission from GaSe in the region of the fundamental absorption edge, which was measured within the first 30 ns after the excitation laser pulse. The shortest-wavelength emission component, which peaked at $h\nu = 2.108$ eV, is due to the radiative recombination of free direct excitons. The emission lines α and β with the maxima at 2.096 and 2.089 eV, respectively, represent the emission due to triplet excitons bound to ionized centers (or isoelectronic traps) [4]. The long-wavelength line β is followed by an intense acoustic wing. In a transverse magnetic field with an induction of $B \geq 2$ T ($\mathbf{B} \perp c$, $\mathbf{B} \perp \mathbf{k}_{photon}$: Voigt geometry), the resonance absorption lines of the bound excitons exhibit splitting into triplets. The extreme components in each triplet are linearly polarized with $\mathbf{E} \parallel \mathbf{B}$, while the central component has

the linear polarization $\mathbf{E} \perp \mathbf{B}$. The position of the central component in each triplet is virtually independent of the magnetic field, while the extreme components are shifted in opposite directions. In the fields with $B <$ 2 T, the splitting is not revealed because of the relatively large widths of the α and β lines. Since the character of the magnetooptical effects for the α and β emission lines is the same, the consideration below will be restricted to the behavior of the β line.

Figure 2 presents the degree of linear polarization $P_{\text{lin}}(B)$ of the bound-exciton emission line β measured as a function of the magnetic induction B under the conditions of continuous excitation of the sample crystal at $h\nu_{\text{exc}} = 2.54\ \text{eV} > E_g$. The $P_{\text{lin}}(B)$ value was calculated as

$$P_{\text{lin}}(B) = \frac{I_{\parallel}(B) - I_{\perp}(B)}{I_{\parallel}(B) + I_{\perp}(B)}, \quad (1)$$

where $I_{\parallel}(B)$ and $I_{\perp}(B)$ are the intensities of the exciton emission components polarized with $\mathbf{E} \parallel \mathbf{B}$ and $\mathbf{E} \perp \mathbf{B}$, respectively. As can be seen, a substantial magnetic-field-induced variation in $P_{\text{lin}}(B)$ [as well as in the component intensities $I_{\parallel}(B)$ and $I_{\perp}(B)$] is observed in the interval of magnetic fields from 0 to 0.2 T. As the field increases further, the $P_{\text{lin}}(B)$ value remains virtually unchanged. Under the conditions of the stationary excitation of the crystal, the maximum degree of linear polarization of the exciton emission in the applied magnetic field in Fig. 2 is ~0.2.

It was established that, under the conditions of excitation by short light pulses, the degree of linear polarization of the exciton emission as a function of the magnetic field varies significantly with the time t during the lifetime of the excited state. This is illustrated in Fig. 3, which shows the degree of linear polarization of the exciton emission, $P_{\text{lin}}(B, t) = [I_{\parallel}(B, t) - I_{\perp}(B, t)]/[I_{\parallel}(B, t) + I_{\perp}(B, t)]$, as measured for various delay times t between the termination of the excitation pulse and the arrival of the detection gate pulse. The time interval for the measurement of the luminescence (the detection gate width) was $\Delta t = 30$ ns. As can be seen from Fig. 3, the magnetic-field dependence of the degree of linear polarization of the exciton emission observed for small delay times ($t \le 0.2$ μs) is nonmonotonic: at a fixed t, $P_{\text{lin}}(B, t)$ first increases with B, reaches a maximum, and then decreases with increasing of the field (see curves for $t = 0.1$ and 0.2 μs). As the delay time t increases, the behavior of $P_{\text{lin}}(B, t)$ changes. The rate of the initial buildup of the degree of polarization in the magnetic field increases sharply but, reaching almost the maximum level in a relatively small field, the $P_{\text{lin}}(B, t)$ value virtually ceases to change (Fig. 3, $t = 0.5$ μs) or changes rather weakly ($t = 1$ μs) when the field increases further. The maximum degree of linear polarization reached in the applied field monotonically increases with the delay time from $P_{\text{lin}}(B, t) \approx <0.15$ for $t = 0.1$ μs to $P_{\text{lin}}(B, t) \approx 1$ for $t = 1$ μs. In other words, the maximum value of $P_{\text{lin}}(B, t)$ increases with the time during which the

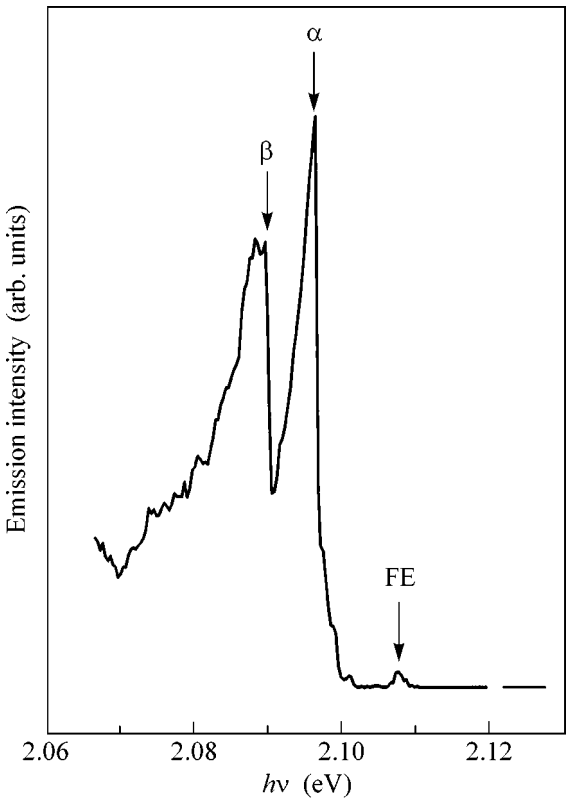

Fig. 1. Emission spectrum of a GaSe crystal at $T = 2$ K.

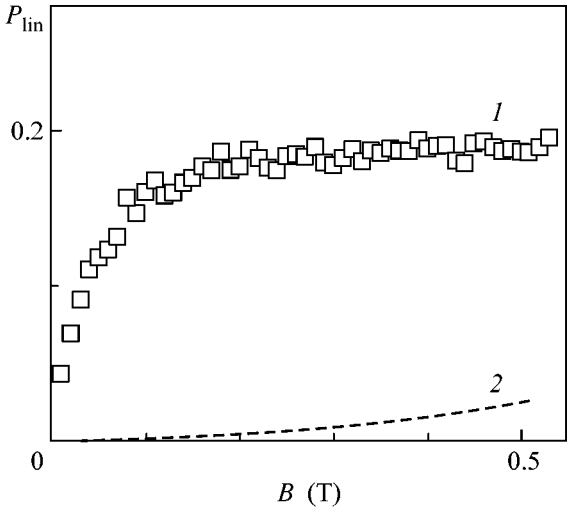

Fig. 2. Degree of linear polarization $P_{\text{lin}}(B)$ of the triplet bound β exciton emission versus the magnetic induction B obtained under the conditions of the continuous excitation of luminescence ($\mathbf{B} \perp c$, $\mathbf{B} \perp \mathbf{k}_{\text{photon}}$ geometry; $T = 2$ K): (*1*) the experimental data and (*2*) theoretical dependence for the Boltzmann distribution of triplet excitons over Zeeman sublevels.

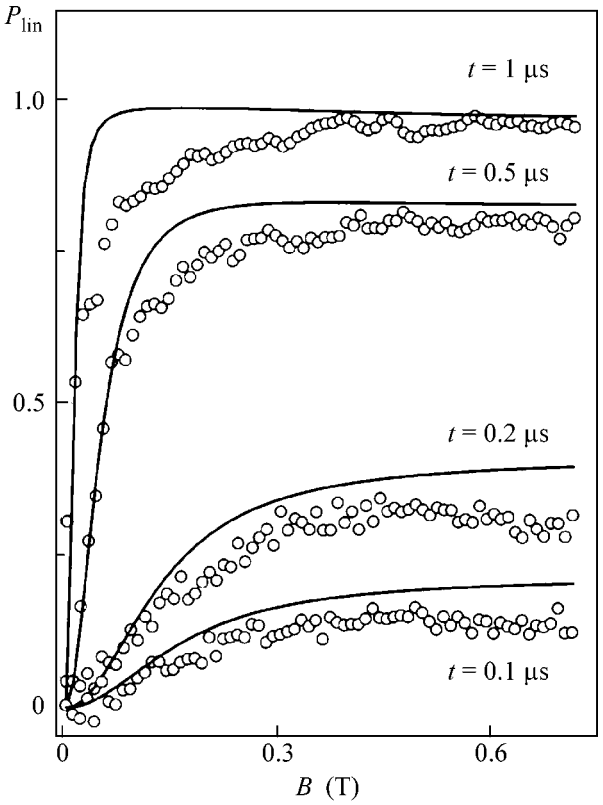

Fig. 3. Magnetic-field dependences of the degree of linear polarization $P_{lin}(B, t)$ of the triplet bound β exciton emission observed at various moments t of the excited state lifetime (indicated in the figure) ($\mathbf{B} \perp c$, $\mathbf{B} \perp \mathbf{k}_{photon}$ geometry; T = 2 K): the points present the experimental data and the curves show the results of the theoretical calculation.

bound excitons are exposed to the magnetic field and reaches, virtually, a 100% level for sufficiently large delay times t.

In order to explain the observed evolution of the $P_{lin}(B, t)$ curve with the delay time, let us consider the structure of the energy levels of the triplet bound excitons in GaSe. In these crystals, the orbitally nondegenerate state Γ_4 of excitons bound at ionized centers (or isoelectronic traps), as well as the ground state of a free direct exciton [5], split into two states, singlet and triplet. For the free exciton, this singlet–triplet splitting amounts to $\Delta_1 \approx 2$ meV. The triplet excitons are characterized by the total spin $S = 1$ and the spin projections $S_z = 0, \pm 1$ onto the optical axis c. Transitions to the states with $S_z = \pm 1$ are allowed for the $\mathbf{E} \perp c$ polarization, while the state with $S_z = 0$ is optically inactive [5]. Owing to the anisotropy of the crystal, the state with $S_z = 0$ is split from the states with $S_z = \pm 1$ by the energy Δ [6].

The transverse magnetic field ($\mathbf{B} \perp c$) produces mixing of the states with $S_z = \pm 1$ and the state with $S_z = 0$, which makes the latter state optically active and results in the splitting of the exciton emission line into triplet. The energies of the triplet exciton states in a magnetic field, calculated using perturbation theory, are given by the expression [3]

$$E_{1,2} = E_0 - 0.5\{\Delta \mp [\Delta^2 + \Omega^2(B)]^{0.5}\}, \quad E_3 = E_0, \quad (2)$$

where $\Omega(B) = g_\perp \mu_0 B$, $g_\perp \equiv g_{xx} = g_{yy}$ is the transverse component of the exciton g factor, and μ_0 is the Bohr magneton. The optical transitions from states 1 and 2 are allowed for the $\mathbf{E} \parallel \mathbf{B}$ polarization, and from state 3, for the $\mathbf{E} \perp \mathbf{B}$ polarization. The radiative lifetimes of the excitons in states 1–3 are $\tau_{ir}(B) = C_i(B)\tau_r$ (i = 1, 2, 3), where $C_{1,2}(B) = 2\{1 \pm \Delta/[\Delta^2 + \Omega^2(B)]^{0.5}\}^{-1}$, $C_3(B) = 1$, and τ_r is the radiative lifetime of the initial states with $S_z = \pm 1$. The intensities of the radiative transitions from states 1–3 are determined by the transition probability and the population of the corresponding state, which, in turn, depends on the total lifetime of the excitons. The total lifetimes of the excitons in states 1–3 are $\tau_i(B) = [\tau_{ir}^{-1}(B) + \tau_0^{-1}]^{-1}$ (i = 1, 2, 3), where τ_0 is the nonradiative lifetime (assumed to be independent of the spin state of a triplet bound exciton).

When the crystal is excited by unpolarized light with $h\nu_{exc} > E_g$, the intensities of the emissions due to the excitons in states 1–3 can be expressed as

$$I_i(B, t) = I_0 \tau_{ir}^{-1}(B) \exp\left[-\frac{t}{\tau_i(B)}\right], \quad (3)$$

where I_0 is proportional to the rate of the exciton production (which is the same for i = 1, 2, 3). The intensities of the π and σ emission components [$I_\parallel(B, t)$ and $I_\perp(B, t)$, respectively] are related to $I_i(B, t)$ as

$$I_\parallel(B, t) = I_1(B, t) + I_2(B, t), \quad I_\perp(B, t) = I_3(B, t). \quad (4)$$

The curves of $P_{lin}(B, t)$ calculated using relations (4) are depicted by the solid lines in Fig. 3. As can be seen, these theoretical curves satisfactorily describe the experimentally observed features in the behavior of the magnetic-field-induced linear polarization of the exciton emission during the lifetime of the excited states. The curves in Fig. 3 were calculated for the following parameters of triplet bound β excitons: $g_\perp = 3.7$ [4]; $\tau_r = 115 \times 10^{-9}$ s; $\tau_0 = 7 \times 10^{-6}$ s; $\Delta = 0.04$ meV (these values virtually coincide with the data obtained in experiments on the anticrossing of the spin sublevels of bound β excitons in a longitudinal magnetic field [7]).

The above considerations can be, in principle, generalized so as to take into account the thermalization of excitons caused by their spin relaxation. The effect of spin relaxation on the population of various Zeeman sublevels of triplet excitons was studied in [8, 9]. Figure 2 (dashed line) shows the curve of $P_{lin}(B)$ for completely thermalized excitons (corresponding to the Boltzmann distribution of excitons over Zeeman sublevels). As can be seen, this $P_{lin}(B)$ value is quite small as compared to

the experimentally observed degree of linear polarization, which justifies the neglect of the spin relaxation of excitons in deriving formula (3).

In conclusion, we have demonstrated that the maximum degree of the magnetic-field-induced linear polarization of the triplet bound-exciton emission varies depending on the time of the exciton exposure to the applied magnetic field (rather than remains constant during the lifetime of the exciton states), increasing from nearly zero up to ~100%. An analysis of the time variation of the magnetic-field-induced polarized luminescence of the triplet excitons emission makes it possible to determine the radiative and nonradiative lifetimes of various spin states of the triplet excitons and their dependence on the external magnetic field, as well as the parameters of the fine structure of these exciton states.

REFERENCES

1. P. P. Feofilov, *Polarized Luminescence of Atoms, Molecules, and Crystals* (Fizmatgiz, Moscow, 1959) [in Russian].
2. *Excitons*, Ed. by E. I. Rashba and M. Sturge (North-Holland, Amsterdam, 1982; Nauka, Moscow, 1985).
3. E. M. Gamarts, E. L. Ivchenko, G. E. Pikus, *et al.*, Fiz. Tverd. Tela (Leningrad) **22**, 3620 (1980) [Sov. Phys. Solid State **22**, 2119 (1980)].
4. E. M. Gamarts, E. L. Ivchenko, G. E. Pikus, *et al.*, Fiz. Tverd. Tela (Leningrad) **24**, 2325 (1982) [Sov. Phys. Solid State **24**, 1320 (1982)].
5. E. Mooser and M. Schlüter, Nuovo Cimento B **18**, 164 (1973).
6. E. L. Ivchenko, G. E. Pikus, B. S. Razbirin, and A. N. Starukhin, Zh. Éksp. Teor. Fiz. **72**, 2230 (1977) [Sov. Phys. JETP **45**, 1172 (1977)].
7. A. N. Starukhin, D. K. Nelson, and B. S. Razbirin, Phys. Rev. B **65**, 193204 (2002).
8. K. Morigaki, Jpn. J. Appl. Phys. **22**, 375 (1983).
9. W. M. Chen, M. Godlewski, B. Monemar, and J. P. Berman, Phys. Rev. B **41**, 5746 (1990).

Translated by P. Pozdeev

JETP Letters, Vol. 80, No. 10, 2004, pp. 646–650. Translated from Pis'ma v Zhurnal Éksperimental'noĭ i Teoreticheskoĭ Fiziki, Vol. 80, No. 10, 2004, pp. 752–757.

Investigation of a Nonequilibrium Electron Subsystem in Low-Temperature Microwave Detectors

I. A. Devyatov* and M. Yu. Kupriyanov

Institute of Nuclear Physics, Moscow State University, Vorob'evy gory, Moscow, 119899 Russia

**e-mail: idev@pn.sinp.msu.ru*

Received October 19, 2004

The electron energy distributions arising in small-size metal absorbers of microwave radiation detectors operating at ultralow temperatures have been calculated using the kinetic equation. It is shown that the electron distributions are nonequilibrium, significantly different from the Fermi distribution, and are determined by the ratio of the rates of electron–electron and electron–phonon relaxation and by the effect of the measuring element (superconductor–insulator–normal metal junction) on the absorber. The response of such a bolometer is calculated and compared to the experimental data. © *2004 MAIK "Nauka/Interperiodica".*

PACS numbers: 85.35.–p

In recent years, much attention has been devoted to theoretical and experimental investigations of nonequilibrium processes induced in a normal metal by electromagnetic radiation with a frequency much lower than that of the interband transitions. Direct experimental observation of such processes has become possible after the creation of lasers generating ultrashort (femtosecond) output radiation pulses. The results of direct measurements of the laser-induced emission current showed that, immediately after the laser pulse, the electron energy distribution function in the metal has a substantially nonequilibrium shape different from that of the Fermi function [1].

A different experimental arrangement is possible with the use of low-temperature bolometers based on the Andreev reflection of electrons [2, 3], where a thin, narrow, and short normal-metal stripe is confined between superconducting electrodes or low-transparency tunneling barriers. The element is kept at an ultralow temperature (on the order of ~0.1 K) and exposed to a continuous electromagnetic signal, mostly in the terahertz or infrared range. The resulting deviations in the electron energy distribution function from the equilibrium one in the normal metal absorber are manifested by a change in the current–voltage characteristic of an additional superconductor–insulator–normal metal (SIN) junction [2, 3].

The aim of this study was to develop a theory describing the absorption of electromagnetic radiation in the submillimeter wavelength range in a normal metal at ultralow temperatures and to apply this theory to calculation of the response characteristics of an Andreev-type bolometer.

A kinetic equation for the electron distribution function $f(\mathbf{k})$ in a metal absorber of the Andreev-type bolometer can be written as

$$\frac{df(\mathbf{k})}{dt} = \left.\frac{\partial f(\mathbf{k})}{\partial t}\right|_{e-e} + \left.\frac{\partial f(\mathbf{k})}{\partial t}\right|_{e-ph} + \left.\frac{\partial f(\mathbf{k})}{\partial t}\right|_{e-pt} + \left.\frac{\partial f(\mathbf{k})}{\partial t}\right|_{SIN}, \quad (1)$$

where $\mathbf{k}$ is the electron wavevector. The first and second terms on the right-hand side of Eq. (1) reflect the electron–electron (e–e) and electron–phonon (e–p) collisions, respectively; the third term describes the absorption of photons by electrons in the absorber with the momentum transfer to ions in the metal [4, 5]; and the fourth term takes into account the effect of the measuring element (SIN junction) on the absorber.

The right-hand side of Eq. (1) does not contain diffusion terms, since the geometric dimensions of the absorber in the typical experimental situation [2, 3] are small as compared to the characteristic lengths of the energy relaxation. In what follows, we will also ignore the effects associated with the loss of quasiparticles in the bolometer electrodes.

Let us assume that, prior to the onset of the radiation action, the distribution functions of the electrons $f(\mathbf{k})$ and phonons $g(\mathbf{q})$ were described by the equilibrium Fermi function $f_F(k) = 1/\left[1 + \exp\left(\frac{\varepsilon(k)-\mu}{k_B T}\right)\right]$ and the equilibrium Bose function $g_B(q) = 1/\left[\exp\left(\frac{\varepsilon(q)}{k_B T}\right) - 1\right]$, respectively, where μ is the chemical potential, k_B is the Boltzmann constant, and T is the absolute temperature of the absorber. The electrons are assumed to obey the

0021-3640/04/8010-0646$26.00

quadratic dispersion law, $\varepsilon(k) = \hbar^2k^2/2m$, the while phonons obey the linear law $\varepsilon(q) = \hbar v_s q$ ($\mathbf{q}$ is the phonon wavevector, m is the electron mass, and v_s is the speed of sound in the metal); the latter dispersion law implies that only acoustic phonons are taken into consideration. The above assumptions are quite natural for copper, the typical absorber material [2].

The phonon subsystem of the absorber will be considered as a thermostat, so that the phonon distribution remains in equilibrium after the onset of the electromagnetic radiation action on the absorber. This assumption is justified by the small thickness of the absorber film [2, 3], the low working temperatures, the relatively small signal frequency (on the order of 1 THz), and the small Kapitza resistance at the film boundary [6], which allows the phonon subsystem to be considered as common for the film–substrate system. In this respect, the case under consideration differs from that studied in [7] within the framework of a model of the "phonon bubble" appearing under the action of an x-ray photon in a metal (or superconducting) absorber.

Owing to the energy continuously pumped to the electron subsystem of the normal metal film as a result of the absorption of electromagnetic radiation, the electrons in the absorber must acquire a quasi-stationary energy distribution described by the function $f(\mathbf{k})$. This function is determined by the balance between the energy absorbed by the electron subsystem and the energy transferred by the electrons to the phonon thermostat and to the measuring element (SIN junction). The function $f(\mathbf{k})$ can be found by equating the right-hand side of Eq. (1) to zero.

In what follows, we proceed from the standard form of the electron–electron and electron–phonon collision terms [5, 8]. The electron–photon–ion interaction in kinetic equation (1) will be adopted in the form proposed in [4]. Passing in the conventional way [8] from summation to integration with respect to momentum in the aforementioned collision terms, we arrive [5] at a system involving two two-dimensional integrals and one six-dimensional integral. The integrals can be restricted to two-dimensional by assuming the signal to be unpolarized and averaging over all the polarization directions.

Further simplification of the collision integrals is possible due to the smallness of the electromagnetic signals acting on the Andreev-type bolometers intended for radio-astronomy observations. For this reason, the unknown electron distribution function can be represented as $f(\mathbf{k}) = f_F(k) + \delta f(\mathbf{k})$, where $\delta f(\mathbf{k})$ is a small nonequilibrium correction to the equilibrium Fermi function $f_F(k)$. Moreover, taking into account the ultralow working temperatures of the absorbers in the bolometers under consideration (~0.1 K [2, 3]), it is possible to replace (in most of the calculations carried out below) the equilibrium Fermi functions $f_F(\varepsilon)$ entering into the collision integrals by the Heaviside step function $\Theta(\mu-\varepsilon)$.

In the terahertz frequency range of electromagnetic signals, the photon energy $\hbar\omega$ (ω is the signal frequency) is about 50 K, which is much higher than the absorber temperature but significantly lower than the characteristic energy parameters $\hbar v_s q_D$ and μ (q_D is the Debye momentum). Taking this circumstance into account, the linearized electron–electron and electron–phonon collision integrals can be transformed as

$$\left.\frac{\partial f(\mathbf{k})}{\partial t}\right|_{e-e} = \tau_{e-e}^{-1}\left[-\nu^2 z^2 - \alpha_{e-e}t^2 + 2\nu^2\left\{\Theta(z)\left(2\int_z^1 ds\varphi(s)(s-z) + \int_{-1}^{-z} ds\varphi(s)(s+z)\right) + \Theta(-z)\left(2\int_{-1}^{z} ds\varphi(s)(z-s) - \int_{-z}^{1} ds\varphi(s)(s+z)\right)\right\}\right], \quad (2)$$

$$\left.\frac{\partial f(\mathbf{k})}{\partial t}\right|_{e-ph} = \tau_{e-p}^{-1}\left[-\nu^3 z^3 - \alpha_{e-p}t^3 + 3\nu^3\left\{\Theta(z)\int_z^1 ds\varphi(s)(s-z)^2 + \Theta(-z)\int_{-1}^{z} ds\varphi(s)(s-z)^2\right\}\right], \quad (3)$$

where $z = \varepsilon/\hbar\omega$ is the normalized energy variable, $\varphi(z) = \delta f((\varepsilon - \mu)/\hbar\omega)$, $\tau_{e-p}^{-1} = \pi\mu^3/4\hbar(k_B T_D)^2$, $\alpha_{e-p} = 21\xi(3)$, $\nu = \hbar\omega/\mu$, $\tau_{e-e}^{-1} \cong 1.47\sqrt{\pi}\,\mu/32\hbar\sqrt{a_B k_F}$, $\alpha_{e-e} \cong 9.84$, $t = k_B T/\mu$, a_B is the Bohr radius, T_D is the Debye temperature, and $\xi(3) \cong 1.2$ is the Riemann zeta function.

In view of the considerations used in deriving the linearized electron–electron collision term (2) and the electron–phonon collision term (3), the term describing the electron–photon–ion interaction (source function) [4, 5] can be written as

$$\left.\frac{\partial f(\mathbf{k})}{\partial t}\right|_{e-pt} = \tau_{e-pt}^{-1}\{\Theta(1-z)\Theta(z) - \Theta(-z)\Theta(z+1)\}, \quad (4)$$

$$\tau_{e-pt}^{-1} = 2^{-5.5}\pi^{-2}\hbar^{-2}m^{-1.5}V_a^{-1}e^6E^2\omega^{-4}\varepsilon_0^{-2}\varepsilon(k)^{-0.5},$$

where V_a is the absorber volume, ε_0 is the permittivity of free space, and E is the electric field strength in the wave. When deriving Eq. (4), we ignored the insignificant dependence of the source function on the direction of the electromagnetic wave propagation, since elastic scattering on impurities produces unavoidable isotropization of the source. The energy dependence of the source function has the characteristic stepwise shape.

Using our previous results [9], it can be shown that the term describing the effect of a measuring element

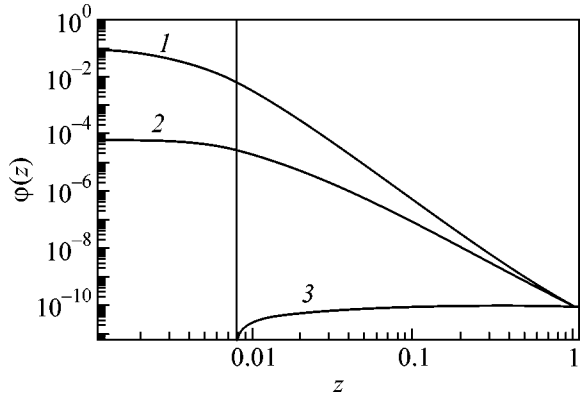

Fig. 1. Nonequilibrium electron energy distribution formed in the absorber under the action of electromagnetic radiation: (*1*) distribution function numerically calculated in the limit $\tau_{SIN}^{-1} \ll \tau_{e-p}^{-1}, \tau_{e-e}^{-1}$ for the parameters $\nu\tau_{e-p}/\tau_{e-e} = 0.023$, $(\tau_{e-e}^{-1}\alpha_{e-e}t^2 + \tau_{e-p}^{-1}\alpha_{e-p}t^3)\tau_{e-p}\nu^{-3} = 1.3 \times 10^{-6}$, an absorber temperature of 0.1 K, a signal frequency of 10^{12} Hz, and a signal power of 10^{-13} W; (*2*) distribution function calculated for the same limit in the τ approximation; (*3*) distribution function calculated in the opposite limit ($\tau_{SIN}^{-1} \gg \tau_{e-p}^{-1}, \tau_{e-e}^{-1}$) when the electron distribution in the absorber is determined by the distribution of the quasiparticle excitations in the superconductor of the SIN junction (for a SIN junction voltage corresponding to $eV/\hbar\omega = 0.05$ and a relative superconducting gap of $\Delta/\hbar\omega = 0.058$).

(SIN junction) on the electron distribution function in Eq. (1) has the form

$$\left.\frac{\partial f(\mathbf{k})}{\partial t}\right|_{SIN} = -\tau_{SIN}^{-1}N_s(z + eV/\hbar\omega)\varphi(z), \qquad (5)$$

where $\tau_{SIN}^{-1} = e^2R_NV_aN(\varepsilon_F)$, V is the voltage across the SIN junction, $N_s(\varepsilon) = \{\Theta(\varepsilon - \Delta) + \Theta(-\varepsilon - \Delta)\}|\varepsilon|/\sqrt{\varepsilon^2 - \Delta^2}$ is the normalized density of states of the superconductor, Δ is the gap in the superconductor excitation spectrum, $N(\varepsilon_F)$ is the density of states at the Fermi level, and R_N is the normal resistance of the SIN junction.

It can be readily verified that, in the absence of the measuring-element-related term ($\left.\frac{\partial f(\mathbf{k})}{\partial t}\right|_{SIN} = 0$) or for zero voltage across the SIN junction ($V = 0$), a solution of kinetic equation (1) determined by relations (2)–(4) is antisymmetric: $\varphi(z) = -\varphi(-z)$. In this case, the electron–electron collision term converts into an expression previously obtained in [10, 11], and the electron–phonon collision term (3) reduces to a result reported in [7]. It should be noted that the electron–phonon collision term introduced in [11] is valid for energies much higher than the Debye energy and, hence, is inapplicable in the case under consideration. It was pointed out in [12] that the nonintegral electron–electron and electron–phonon collision terms (τ-terms) can be well approximated by quadratic and cubic polynomials, respectively.

It should be noted that the presence of integrals (entering together with the τ-terms) in the linearized electron–electron collision term (2) and electron–phonon collision term (3) is attributed to the nonlocal character of the source term (4) with respect to the energy. The need for introducing integral terms into the linearized Boltzmann equation with a nonlocal source was also pointed out in [12].

Upon substituting the linearized collision integrals (2)–(5) into the stationary kinetic equation (1), we obtain a Volterra integral equation of the second kind, which has to be considered on the interval $z \in [-1, 1]$, where this equation is inhomogeneous. Physically, this implies the impossibility of sequential absorption of several photons in the case of a weak signal described by the linearized equation.

Numerical solution of the integral equation determined by relations (1)–(5) on the interval $z \in [-1, 1]$ reduces to constructing the corresponding recurrence relation proceeding from the boundaries. The results of the numerical calculations of the electron distribution function are presented in Fig. 1, where curve *1* corresponds to the case of a weak effect of the SIN junction on the absorber, that is, to the condition $\tau_{SIN}^{-1} \ll \tau_{e-p}^{-1}, \tau_{e-e}^{-1}$. In this case, the parameters of the integral equation, calculated based on the experimental data [2, 3], were as follows: $\nu\tau_{e-p}/\tau_{e-e} = 0.023$; $(\tau_{e-e}^{-1}\alpha_{e-e}t^2 + \tau_{e-p}^{-1}\alpha_{e-p}t^3)\tau_{e-p}\nu^{-3} = 1.3 \times 10^{-6}$; absorber temperature, 0.1 K; signal frequency, 10^{12} Hz; and signal power, 10^{-13} W. As can be seen, this electron distribution function is close to the power dependence $(\varepsilon - \mu)^{-4}$ for energies z that are not too low—namely, for those higher than $[(\tau_{e-e}^{-1}\alpha_{e-e}t^2 + \tau_{e-p}^{-1}\alpha_{e-p}t^3)\tau_{e-p}]^{1/3}\nu^{-1}$. This behavior was predicted [7] for the case where only the electron–phonon interaction is taken into account. The results of our numerical analysis showed that the power dependence of the electron distribution on the energy with an exponent close to –4 is valid in a broad range of the ratios of the characteristic relaxation times of the electron–electron and electron–phonon interactions. For an energy close to that of the absorbed radiation quantum, the power dependence changes from $(\varepsilon - \mu)^{-3}$ for the strong electron–phonon interaction to $(\varepsilon - \mu)^{-2}$ for the strong electron–electron interaction.

Curve *2* in Fig. 1 shows the results of numerical solution of the kinetic equation in the same limit $\tau_{SIN}^{-1} \ll \tau_{e-p}^{-1}, \tau_{e-e}^{-1}$ but with neglect of the integrals in the collision terms given by relations (2) and (3), that is, in the τ approximation. A comparison between curves *1* and *2* shows that the inclusion of the integral terms into the kinetic equation leads to a significant increase in the

electron distribution function in the region of low energies.

In this opposite limit, $\tau_{SIN}^{-1} \gg \tau_{e-p}^{-1}, \tau_{e-e}^{-1}$, the electron distribution function in the region of energies $|\varepsilon| > \Delta$ is determined by the effect of a superconductor of the SIN junction on the absorber and is proportional to $N_s^{-1}(\varepsilon + eV)$. The results of numerical calculations in this case are presented by curve *3* in Fig. 1. It should be noted that the condition $\tau_{SIN}^{-1} \gg \tau_{e-p}^{-1}, \tau_{e-e}^{-1}$ can be satisfied only for extremely small values of R_N (below 0.1 Ω) in the SIN junction.

It should be emphasized that the calculated electron distribution function in all cases has proved to be nonequilibrium and substantially different in shape from the Fermi function.

The response $\eta = I/P$ of the Andreev-type bolometer is determined by the electron energy distribution in the absorber at $|\varepsilon| > \Delta$. The current I through the measuring element (SIN junction) is calculated using the standards formula obtained in the tunneling theory: $I = (eR_N)^{-1}\int d\varepsilon\,[f(\varepsilon - eV) - f_s(\varepsilon)]N_s(\varepsilon)$, where $f(\varepsilon)$ is the solution to Eq. (1) and $f_s(\varepsilon)$ is the distribution function for quasiparticles in the superconductor. The power P absorbed in a quasi-stationary regime is determined by source function (4), which yields $P = \tau_{e-pt}^{-1} N(\varepsilon_F) V_a (\hbar\omega)^2$. When the distribution function is determined by the effect of the SIN junction on the absorber ($\tau_{SIN}^{-1} \gg \tau_{e-p}^{-1}, \tau_{e-e}^{-1}$), which is represented by curve *3* in Fig. 1, both the analytical estimates and direct numerical calculations show that the response is described by the relations

$$\eta = \beta\eta_{fc}, \quad \eta_{fc} = \frac{e}{\hbar\omega}, \quad \beta \cong \frac{2eV}{\hbar\omega}. \qquad (6)$$

In the experiments reported in [2, 3], the voltage across the SIN junction was slightly below the superconducting energy gap, which, in turn, was much smaller than the typical energy quantum: $eV \lesssim \Delta \ll \hbar\omega$. Therefore, the detector response is much lower than that in the "photon counter limit" $e/\hbar\omega$ [13], in which case each absorbed energy quantum $\hbar\omega$ induces the tunneling of an electron e through the junction. The suppression factor ($\beta \cong 2eV/\hbar\omega \ll 1$) in the above expression for the detector response appears due to the relatively high signal frequency ($\hbar\omega \gg \Delta$), which leads to a significant current of hole excitations in the junction. A similar (but half as small) suppression factor appears in the usual detectors based on the quasiparticle nonlinearity [13] and restricts their high-frequency applications. Under the conditions of low frequencies ($\hbar\omega \lesssim \Delta$) and $\tau_{SIN}^{-1} \gg \tau_{e-p}^{-1}, \tau_{e-e}^{-1}$, the detector response reaches the photon counter limit $e/\hbar\omega$.

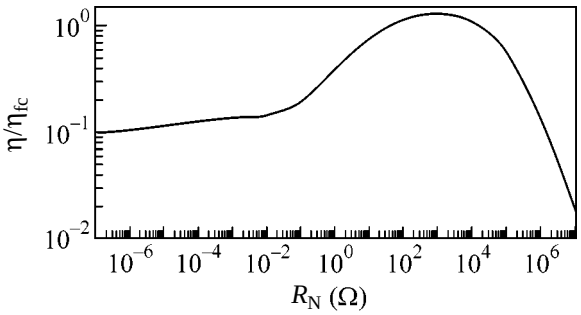

Fig. 2. Bolometer response vs. the SIN junction resistance (for a SIN junction voltage corresponding to $eV/\hbar\omega = 0.05$ and a relative superconducting gap of $\Delta/\hbar\omega = 0.058$; the response is normalized to $\eta_{fc}(1\ \text{THz}) = e/\hbar\omega \approx 241.3$ A/W; $\omega = 2\pi \times 10^{12}\ \text{s}^{-1}$).

For bolometric detectors, the response (in the bias voltage set regime) is restricted to a value of $\eta \lesssim e/k_BT$ [2, 14], whereby each thermalized electron tunneling with the energy k_BT via the measuring junction transfers the charge e. At a sufficiently low temperature of the absorber ($k_BT \ll \hbar\omega$), the "bolometric" response limit e/k_BT is much higher than the photon counter limit $e/\hbar\omega$. For the small-size low-temperature microwave detectors under consideration, the complete thermalization is impossible. Figure 2 shows the results of numerical calculations of the bolometric detector response as a function of the SIN junction resistance R_N for the material parameters of the absorber corresponding to the experiment described in [2]. As can be seen, the response is determined by relation (6) at small R_N ($\beta = 0.1$) and tends to zero as $R_N \longrightarrow \infty$. Thus, there is an optimum resistance (R_{opt}) of the SIN junction for which the bolometer response exhibits a maximum. According to Fig. 2, the maximum response is observed for $R_N \approx 10^3$ Ω. The maximum calculated value of the bolometer response is close to the recent experimental data [15].

It was also of interest to study the detector response as a function of the ratio of the characteristic times of the electron–electron and electron–phonon relaxation. Figure 3 shows the response of a bolometer with $R_N = R_{opt} = 10^3$ Ω as a function of the normalized electron–electron relaxation rate, τ_{SIN}/τ_{e-e} at a fixed total relaxation rate ($\tau_{SIN}/\tau_{e-e} + \tau_{SIN}/\tau_{e-p} = \text{const}$). As can be seen, an increase in the τ_{SIN}/τ_{e-e} ratio leads to an increase in the response, which is explained by the effective multiplication of quasiparticles as a result of the electron–electron collisions [10]. Although the number of electrons upon electron–phonon collisions in the absorber does not increase, these interactions convert high-energy excitations to the region of the superconducting gap that increases the response above the photon counter limit (6) even at $\tau_{SIN}/\tau_{e-e} = 0$.

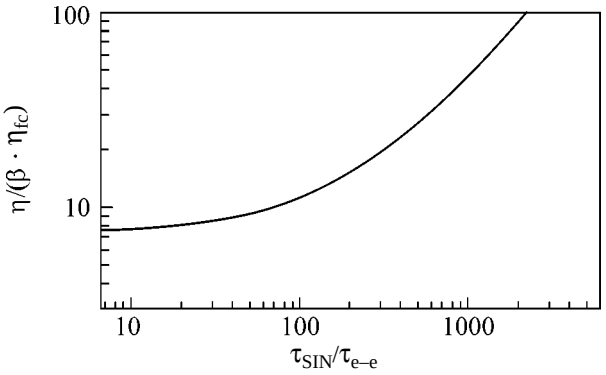

Fig. 3. Bolometer response vs. the ratio of the characteristic times of the electron–electron relaxation (τ_{SIN}/τ_{e-e}) and electron–phonon relaxation (τ_{SIN}/τ_{e-p}) at a fixed total relaxation rate ($\tau_{SIN}/\tau_{e-e} + \tau_{SIN}/\tau_{e-p} = 6550$. The measuring SIN junction has a nearly optimum resistance of $R_N = 1000\ \Omega$; the response is normalized to $\beta\eta_{fc}(1\ \text{THz}) = \beta e/\hbar\omega \approx 24.13$ A/W; $\beta = 0.1$; $\omega = 2\pi \times 10^{12}\ \text{s}^{-1}$.

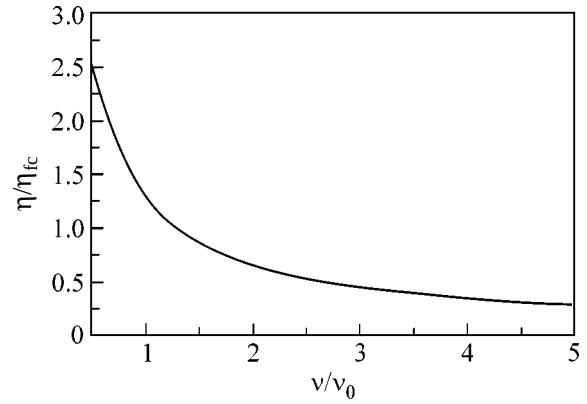

Fig. 4. Frequency dependence of the bolometer response numerically calculated for $\tau_{SIN}/\tau_{e-e} = 150$, $\tau_{SIN}/\tau_{e-p} = 6400$, and $R_N = 1000\ \Omega$. The frequency ν is normalized to $\nu_0 = 1$ THz; the response is normalized to $\eta_{fc}(1\ \text{THz}) = e/\hbar\omega \approx 241.3$ A/W.

Figure 4 presents the results of numerical calculations of the frequency dependence of the detector response. These data show that the response decreases with increasing the signal frequency. The calculated curve is close to the experimental frequency dependence of the ω^{-1} type observed in [15].

In summary, the calculations of the electron energy distribution function in a metal absorber of the Andreev-type bolometer [2, 3] under the action of electromagnetic radiation in the terahertz range showed that the electron distribution is substantially nonequilibrium. In the case of a weak effect of the measuring element (SIN junction) on the absorber (that is, for $\tau_{SIN}^{-1} \ll \tau_{e-p}^{-1}, \tau_{e-e}^{-1}$), the distribution function is well approximated by the power dependence $(\varepsilon - \mu)^N$ with the exponent $N \approx -4$; in the opposite limit $\tau_{SIN}^{-1} \gg \tau_{e-p}^{-1}, \tau_{e-e}^{-1}$, the distribution function in the region of energies $|\varepsilon| > \Delta$ is determined by the effect of the SIN junction on the absorber and is proportional to $N_s^{-1}(\varepsilon + eV)$.

The detector response calculated using the obtained electron distribution function falls between the photon counter limit $\beta e/\hbar\omega$ [$\beta \ll 1$ is the suppression factor given by formula (6)] and the bolometric response limit e/k_BT and is close to the experimental data reported in [15]. The calculated response decreases with increasing signal frequency as described by a function close to the experimental dependence of the ω^{-1} type [15]. Based on the obtained results, we suggest using metals with strong electron–electron interactions as the absorber materials.

We are grateful to N. Arnold and P. Krutitskiĭ for fruitful discussions. This study was supported by the International Science and Technology Foundation (grant no. 11-95) and the Ministry of Education of the Russian Federation.

REFERENCES

1. R. Fann, H. Storz, K. Tom, *et al.*, Phys. Rev. Lett. **68**, 2834 (1992).
2. M. Nahum and J. Martines, Appl. Phys. Lett. **63**, 3075 (1993).
3. A. Vistavkin, D. Shuvaev, L. Kuzmin, *et al.*, Zh. Éksp. Teor. Fiz. **115**, 1085 (1999) [JETP **88**, 598 (1999)].
4. J. F. Seely and E. G. Harris, Phys. Rev. A **7**, 1064 (1973).
5. B. Rethfeld, A. Kaiser, M. Vicanek, *et al.*, Phys. Rev. B **65**, 214303 (2002).
6. F. C. Wellstood, C. Urbina, and J. Clarke, Phys. Rev. B **49**, 5942 (1994).
7. A. G. Kozorezov, A. F. Volkov, J. K. Wigmore, *et al.*, Phys. Rev. B **61**, 11807 (2000).
8. N. W. Ashcroft and N. D. Mermin, *Solid State Physics* (Holt, Rinehart, and Winston, New York, 1976; Mir, Moscow, 1979).
9. I. A. Devyatov and M. Yu. Kupriyanov, Pis'ma Zh. Éksp. Teor. Fiz. **65**, 159 (1997) [JETP Lett. **65**, 171 (1997)].
10. R. H. Ritchie, J. Appl. Phys. **37**, 2276 (1980).
11. V. E. Gusev and O. B. Wright, Phys. Rev. B **57**, 2878 (1998).
12. V. F. Gantmakher and Y. B. Levinson, *Carrier Scattering in Metals and Semiconductors* (Nauka, Moscow, 1984; North-Holland, Amsterdam, 1987).
13. J. R. Tucker and M. J. Feldman, Rev. Mod. Phys. **57**, 1055 (1985).
14. L. S. Kuzmin, Physica B (Amsterdam) **284–288**, 2129 (2000).
15. M. Tarasov, L. Kuzmin, E. Stepantsov, *et al.*, Pis'ma Zh. Éksp. Teor. Fiz. **79**, 356 (2004) [JETP Lett. **79**, 298 (2004)].

Translated by P. Pozdeev

JETP Letters, Vol. 80, No. 10, 2004, pp. 651–654. Translated from Pis'ma v Zhurnal Éksperimental'noĭ i Teoreticheskoĭ Fiziki, Vol. 80, No. 10, 2004, pp. 758–762.

Properties of Josephson Junctions in the Inhomogeneous Magnetic Field of a System of Ferromagnetic Particles

S. N. Vdovichev*, B. A. Gribkov*, S. A. Gusev*, E. Il'ichev, A. Yu. Klimov*, Yu. N. Nozdrin*, G. L. Pakhomov*, V. V. Rogov*, R. Stolz**, and A. A. Fraerman***

** Institute of Physics of Microstructures, Russian Academy of Sciences, Nizhni Novgorod, 603950 Russia*
e-mail: vdovichev@ipm.sci-nnov.ru
*** Institute for Physical High Technology, 07702 Jena, Germany*
Received September 21, 2004; in final form, October 21, 2004

The effect of a system of ferromagnetic particles on the field-dependent critical current of a Josephson junction is experimentally studied for junctions of different geometries. For edge junctions, the effect of commensurability between the periodic magnetic field of the particles and the Josephson vortex lattice is observed. The effect manifests itself in additional maxima of the field-dependent critical current. For overlap junctions, giant (greater than sixfold) variations of the maximum critical current are observed depending on the magnetic state of the particles. The changes in the "Fraunhofer" pattern of the overlaped Josephson junctions are attributed to the formation of Abrikosov vortices due to the effect of uniformly magnetized particles. The effects revealed in the experiments can be used to analyze the inhomogeneous magnetic field of a system of submicron particles and to control the transport properties of Josephson junctions. © *2004 MAIK "Nauka/Interperiodica".*

PACS numbers: 68.37.Rt; 74.50.+r; 75.75.+a

A lattice of ferromagnetic nanoparticles is a unique source of an inhomogeneous magnetic field with an amplitude of about the saturation magnetic moment of the ferromagnet and with a scale of variation that is determined by the lattice period. For typical transition metals (Fe, Ni, and Co), the magnetic moment is $M_s \sim$ 1000 G. The modern lithographic techniques allow one to vary the particle lattice period d over a wide range from 10 to 1000 nm. In addition, the magnetic field of the particles can be varied by magnetizing or demagnetizing the whole lattice or some of its parts. This property of ferromagnetic nanoparticle lattices opens up new possibilities for controlling the properties of superconductors. Studies of ferromagnetic nanoparticles–superconductor hybrid systems revealed a number of interesting phenomena manifested in the oscillatory dependence of the resistance (or the critical current) of the superconductor on the external magnetic field [1]. Specific features appear in the characteristics of the superconductor when the particle lattice with a period d is commensurable with the Abrikosov vortex lattice, whose period d_a is determined by the external magnetic field ($d_a \sim (\Phi_0/H)^{0.5}$, where Φ_0 is the magnetic flux quantum and H is the magnetic field strength). The observation of the commensurability effects in these systems is complicated by the presence of defects in real superconducting films, which leads to distortions of the Abrikosov vortex lattice. To reduce the influence of these distortions, experiments are carried out at a temperature very close to the superconducting transition temperature T_c: $\tau = (T_c - T)/T_c \sim 0.01$. This hampers the use of a ferromagnetic particle lattice for controlling the pinning of Abrikosov vortices.

In this context, we propose to study the effect of the inhomogeneous magnetic field of a system of ferromagnetic particles on "weak" superconductors, i.e., Josephson junctions. One can expect that the effects of the commensurability between the periodic magnetic field of the particles and the Josephson vortex lattice will also be observed in such a system and that they will manifest themselves as additional maxima arising in the dependence of the Josephson critical current on the external field [2, 3]. Owing to the weak pinning of Josephson vortices, this system is preferable over "strong" superconductors. In this paper, we present the results of the first observation of the commensurability effect in Josephson junctions with ferromagnetic particles. Figure 1 shows two types of Josephson junctions with ferromagnetic particles: (a) the edge junction and (b) the overlap junction. We assume that the dependence of the supercurrent through a junction on the

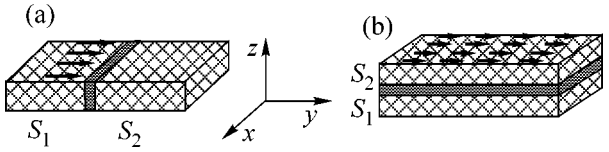

Fig. 1. Schematic diagram of (a) edge and (b) overlap Josephson junctions with ferromagnetic particles.

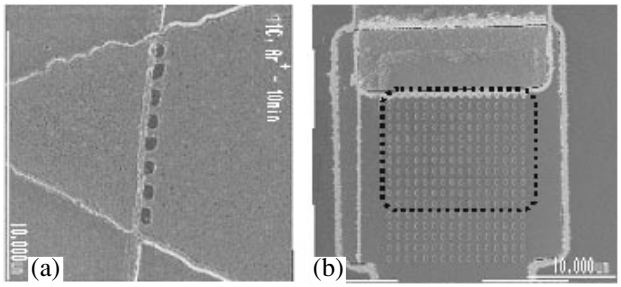

Fig. 2. SEM image of the system under study: (a) edge and (b) overlap junctions with ferromagnetic particles (the dashed line indicates the junction region).

phase difference between the wave functions of the two superconducting electrodes has a simple harmonic form $j = j_c \sin(\varphi)$. The appearance of the phase difference in the Josephson junction is possible due to the penetration of the scattering fields from the ferromagnetic particles into the junction region. Estimates show that the magnetic field induced by uniformly magnetized particles, when averaged over the junction area, is proportional to the particle thickness and inversely proportional to the junction size in the corresponding direction. In the case of the edge junction (Fig. 1a), the *z* component of the magnetic field induced by the particles is inversely proportional to the size of the junction along the *Z* axis. This size is small (~100 nm in our case), and the mean magnetic field in the junction is about the mean magnetic moment of the particle lattice. The calculation of the phase difference induced by the particles in the edge junction confirms this assumption [3]. In the case of the overlap junction (Fig. 1b), the *y* component of the magnetic field is inversely proportional to the junction size along the *Y* axis (~10 μm). Hence, the mean field induced by the particles proves to be approximately one hundredth of that in the previous case. If we ignore this edge effect, the only possibility for a phase difference to appear in the overlap junction due to the effect of ferromagnetic particles is the formation of Abrikosov vortices in the superconductor. The effect of Abrikosov vortices on the field-dependent critical current of the Josephson junction was discussed in [4, 5]. Below, we present the results of an experimental study of the effect produced by a system of ferromagnetic particles on the dependence of the critical current I_c on the external magnetic field for edge and overlap Josephson junctions.

1. EDGE JUNCTIONS

For the experimental study of the effect of particles on the critical current of the Josephson junction, we fabricated Nb/SiN_x/Nb edge junctions with a chain of Co ferromagnetic particles positioned in the immediate vicinity of the junction region. Figure 2a shows an SEM image of the system under study. The method of fabrication and the properties of the edge junctions based on Nb films are described in [6]. The ferromagnetic particles were obtained by electron lithography [7] and had lateral dimensions of 300 × 600 nm and a thickness of 25 nm. The magnetic state of the particles was monitored by a Solver scanning probe microscope. It is well known [8] that the ground state of such large particles is a vortex state. Investigations have shown that a uniformly magnetized (along the long axis) state is metastable in zero external field if the particle thickness does not exceed some critical value, which is equal to 27 nm in our case. Thus, particles with the aforementioned dimensions can be in both vortex and uniformly magnetized states. In the first case, the magnetic field produced by a particle is absent or very small, whereas the field produced by a uniformly magnetized particle in the junction region is about 100 Oe according to our estimates. This situation is optimal for our purposes, because we can control the magnetic field in the junction by preliminarily magnetizing or demagnetizing the system of particles with the use of an external field applied in the easy (along the long particle axis) or hard (along the short particle axis) magnetization direction.

The dependence $I_c(H)$ was measured by the standard four-probe method at a temperature of $T = 4.2$ K (the critical temperature of the superconducting transition in the niobium electrodes was about 9 K). The external magnetic field was perpendicular to the surface of the superconducting electrodes. Figure 3 shows the results of measuring $I_c(H)$ in two different cases: when the chain of particles is uniformly magnetized (Fig. 3a) and when the particles are in the vortex state (Fig. 3b). The magnetic state was prepared by magnetizing the system in different directions at room temperature and was monitored by the scanning probe microscope (the magnetic force images are shown in the insets). In the case of the uniformly magnetized chain, additional maxima are observed. Their positions are determined by the period of the chain of particles and satisfy the relation

$$H_n = n\Delta H(W/d), \qquad (1)$$

where n is the number of a maximum, ΔH is the period of the critical current oscillations in the Josephson junction without the particles, W is the width of the junction, and d is the distance between the particles. This result confirms the theoretical predictions of [2, 3] and can be explained as follows. For a short Josephson junction, the critical current is determined by the expression

$$I_c = j_c l \left| \int_0^W \exp\left(\frac{2\pi i H l x}{\Phi_0}\right) \exp(i\varphi_p(x))\, dx \right|, \qquad (2)$$

where l is the effective thickness of the junction, $\varphi_p(x)$ is the phase difference induced by the particles, and

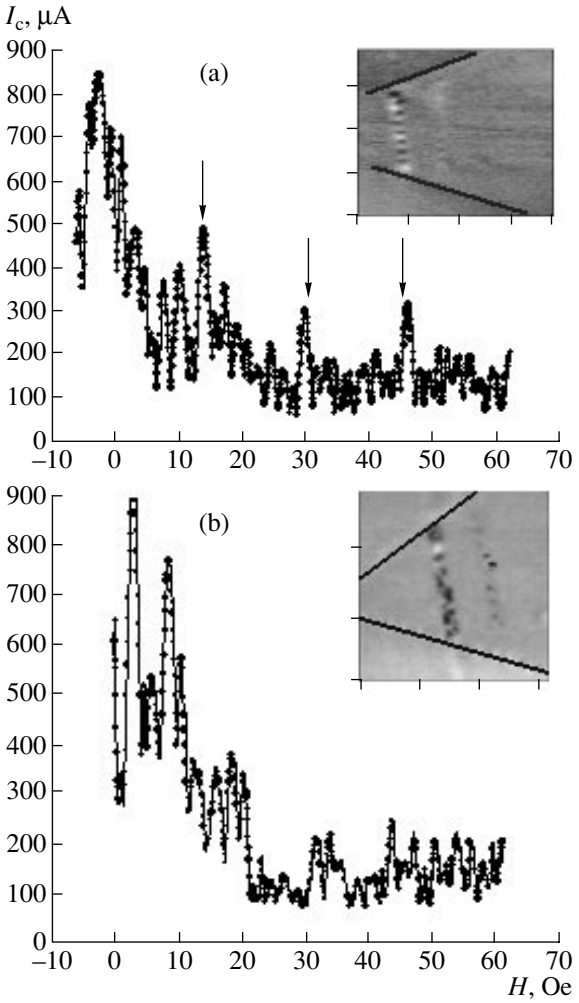

Fig. 3. Dependence $I_c(H)$ for an edge junction with (a) a homogeneously magnetized chain of particles and (b) particles in the vortex state.

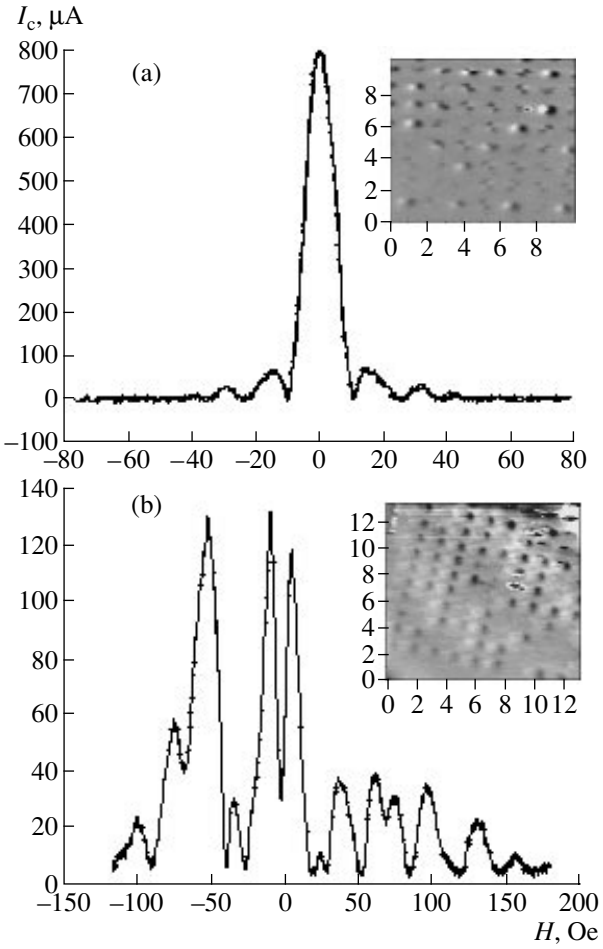

Fig. 4. Dependence $I_c(H)$ for an overlap junction when the particles are (a) in the vortex state (the dependences $I_c(H)$ for the junction without the particles and with particles in the vortex state coincide with each other) and (b) magnetized.

$\varphi_p(x + d) = \varphi_p(x)$. It follows from Eq. (2) that the positions of the maxima of the critical current are determined by the condition of commensurability between the spatial wave of the Josephson current, Φ_0/lH, and the periodic distribution of the phase difference induced by the particles, d. One can say that the short Josephson junction is a Fourier analyzer of the inhomogeneous magnetic field produced by the particles. In our experiment, the Josephson penetration depth is $\lambda_J \sim 3$ μm while $W \sim 8$ μm, and, strictly speaking, the condition of the smallness of the junction is not satisfied. However, the commensurability effects, which lead to the appearance of additional maxima, occur in this case as well. If the particles are demagnetized (i.e., in the vortex state), additional maxima are absent (Fig. 3b) and the dependence $I_c(H)$ is close to that observed for the junction without the particles. This result indicates that the process of the hybrid system fabrication did not damage the junction.

2. OVERLAP JUNCTIONS

For our experiments, a series of Nb/Al/AlO_x/Nb overlap junctions were fabricated using the technology described in [9]. The junctions were characterized by the following parameters: the thickness of both the lower electrode and the leads was about 100 nm, the thickness of the upper electrode was about 30 nm, the thickness of the Al/AlO_x interlayer between the electrodes of the Josephson junction was about 12 nm, and the lateral dimensions of the junction were 20×15 μm. On the upper electrode of the junction, a Co particle lattice was fabricated with characteristic dimensions of 300×600 nm and a thickness of 27 nm. The dimensions of the particle cell were 1×1.5 μm. Figure 2b shows the SEM image of the system under study. A part of the particle lattice lies on the lead, but this is unimportant for our measurements. The measurements of the critical current were performed at a temperature of 4.2 K, and the magnetic field was applied in the junc-

tion plane, along the supercurrent in the electrodes. Figure 4 shows the results obtained by measuring the dependence of the critical current on the external magnetic field for different magnetization states of the particle lattice. When the particles are in the vortex state, the dependence $I_c(H)$ has the same form as that obtained for the junction without the particles (Fig. 4a). A qualitatively different situation is observed when most of the particles in the lattice are uniformly magnetized (Fig. 4b). First, the central peak of the Fraunhofer pattern is split into two and displaced with respect to the zero magnetic field, while its amplitude is smaller by a factor of more than six as compared to the previous case. Second, the behavior of the critical current becomes nonmonotonic in high magnetic fields. However, the positions of the maxima do not satisfy the commensurability condition, i.e., Eq. (1). Note that, after the particles are demagnetized to the vortex state, the critical current and the whole Fraunhofer pattern are restored. Thus, we observe a strong dependence of $I_c(H)$ of the overlap Josephson junction on the magnetic state of the particles.

As discussed above, the considerable effect of the particles on the overlap junction may be attributed to the penetration of the Abrikosov vortices that are induced by the particles into the upper electrode. Experimental studies of the effect of single Abrikosov vortices were performed earlier (see, e.g., [5]). However, in our case, the magnetic particles may induce Abrikosov vortices of different signs, the effect of which on the properties of Josephson junctions has never been studied. The mechanism of the vortex–antivortex pair formation under the action of a particle magnetized along the surface of a superconductor was studied in [10]. For the formation of Abrikosov vortices, the magnetic field of the particle must exceed the upper critical field H_{c2}, because the freezing of the sample occurs in the field of the particle: $H > H_{c2} \sim \Phi_0\tau/\xi_0^2$, where ξ_0 is the coherence length at zero temperature. In this case, the scale of variation of the wave function, $\xi = \xi_0/\sqrt{\tau}$, should be smaller than the distance between the positive and negative magnetic poles, which is about the particle size a: $\xi > a$. When these two conditions are satisfied simultaneously, they lead to the relation $H > \Phi_0/a^2$. The latter condition is satisfied for our particles, which allows us to attribute the changes observed in the Fraunhofer pattern of an overlap Josephson junction to the formation of Abrikosov vortices in the upper electrode under the effect of uniformly magnetized particles.

Thus, we have studied the effect of a lattice of ferromagnetic particles on the field dependence of the critical current in Josephson junctions of different structures. Unlike in the previous publications [11], where the effect of the modulation of the critical current density j_c was investigated, we studied the effect of the "phase" modulation of the Josephson current under the effect of the inhomogeneous magnetic field produced by a system of ferromagnetic particles. For edge junctions, we present the results of the first observation of the commensurability effects, which manifest themselves in the presence of additional maxima in the dependence $I_c(H)$. In principle, this allows one to use a Josephson junction as a Fourier analyzer for the inhomogeneous magnetic field of a system of submicron-size particles. For overlap junctions, we revealed the substantial effect of the magnetic state of the particles on the dependence $I_c(H)$, which manifests itself as the suppression of the critical current in the absence of the magnetic field and a noticeable change in the Fraunhofer pattern. Estimates show that the changes observed in the experiment may be attributed to the formation of Abrikosov vortices in the upper electrode under the effect of homogeneously magnetized particles. This fact can be used to control the transport properties of such junctions.

We are grateful to A.S. Mel'nikov and A.V. Samokhvalov for useful discussions. This work was supported by the Russian Foundation for Basic Research (project nos. 03-02-16774 and 02-02-16764) and the Russian Academy of Sciences (Program "Quantum Macrophysics").

REFERENCES

1. Y. Otani, B. Pannetier, J. P. Nozieres, and D. Givord, J. Magn. Magn. Mater. **126**, 622 (1993); O. Geoffroy, D. Givord, Y. Otany, *et al.*, J. Magn. Magn. Mater. **121**, 223 (1993); J. I. Martin, M. Velez, J. Nogues, and I. K. Shuller, Phys. Rev. Lett. **79**, 1929 (1997); A. V. Silhanek, L. Van Look, S. Raedts, *et al.*, Phys. Rev. B **68**, 214504 (2003).
2. A. Y. Aladyshkin, A. A. Fraerman, S. A. Gusev, *et al.*, J. Magn. Magn. Mater. **258–259**, 406 (2003).
3. A. V. Samokhvalov, Pis'ma Zh. Éksp. Teor. Fiz. **78**, 822 (2003) [JETP Lett. **78**, 369 (2003)].
4. A. A. Golubov and M. Yu. Kupriyanov, Zh. Éksp. Teor. Fiz. **92**, 1512 (1987) [Sov. Phys. JETP **65**, 849 (1987)].
5. O. B. Hyun, J. R. Clem, and D. K. Finnemore, Phys. Rev. B **40**, 175 (1989).
6. S. N. Vdovichev, A. Yu. Klimov, Yu. N. Nozdrin, and V. V. Rogov, Pis'ma Zh. Tekh. Fiz. **30** (9), 52 (2004) [Tech. Phys. Lett. **30**, 374 (2004)].
7. A. A. Fraerman, S. A. Gusev, L. A. Mazo, *et al.*, Phys. Rev. B **65**, 64424 (2002).
8. R. P. Cowburn and M. E. Welland, Appl. Phys. Lett. **72**, 2041 (1998).
9. R. Stolz, L. Fritzsch, and H.-G. Meyer, Supercond. Sci. Technol. **12**, 806 (1999).
10. M. J. Van Bael, J. Bekaert, K. Temst, *et al.*, Phys. Rev. Lett. **86**, 155 (2001).
11. I. L. Serpuchenko and A. V. Ustinov, Pis'ma Zh. Éksp. Teor. Fiz. **46**, 435 (1987) [JETP Lett. **46**, 549 (1987)]; B. A. Malomed and A. V. Ustinov, Phys. Rev. B **41**, 254 (1990); M. A. Itzler and M. Tinkham, Phys. Rev. B **51**, 435 (1995).

Translated by E. Golyamina

JETP Letters, Vol. 80, No. 10, 2004, pp. 655–657. Translated from Pis'ma v Zhurnal Éksperimental'noĭ i Teoreticheskoĭ Fiziki, Vol. 80, No. 10, 2004, pp. 763–765.

Superconducting Transition Temperature in Hafnium under Pressures up to 64 GPa

I. O. Bashkin*, M. V. Nefedova, V. G. Tissen, and E. G. Ponyatovsky

Institute of Solid State Physics, Russian Academy of Sciences, Chernogolovka, Moscow region, 142432 Russia

**e-mail: bashkin@issp.ac.ru*

Received October 11, 2004; in final form, October 27, 2004

The superconducting transition temperature T_c of hafnium is measured as a function of pressure up to 64 GPa. The character of the pressure dependence of T_c observed at α–ω–β transitions in Hf is found to be similar to that observed for Zr. In the regions of α and β phases, T_c increases with pressure with the slopes $dT_c/dP = 0.05$ and 0.16 K/GPa, respectively. At the α–ω transition, $T_c(P)$ exhibits a tendency to a decrease, while at the ω–β transition, T_c increases stepwise from 5.8 to 8.0 K. The α–ω transition occurs at pressures between 31.2 and 35.9 GPa, and the ω–β transition, at a pressure of 62 ± 2 GPa. © *2004 MAIK "Nauka/Interperiodica".*

PACS numbers: 64.70.Kb; 74.62.–c; 74.62.Fj

1. INTRODUCTION

Under normal conditions, the group IV transition metals Ti, Zr, and Hf have a hexagonal close-packed structure (the hcp α phase), whereas, under pressure, all three elements undergo polymorphic transitions [1]. Titanium first transforms to the hexagonal ω phase and then, under $P \le 116$ GPa, to the γ and δ phases with orthorhombic structures [2, 3]. The α–ω–β series of structural transitions including the bcc β phase was first observed for Zr [4] and later, for Hf [5]. For Zr, the pressure corresponding to the ω–β transition lies within 30 [6] to 33 GPa [4]; for Hf, this pressure was found to be $P = 71$ GPa [5]. A correct description of the α–ω–β transition series was obtained as a result of theoretical calculations of the structural stability under pressure [7–9], which attributed the structural changes to the *s*–*d* electron transfer and the corresponding increase in the *d* band population. The measurements of the superconducting transition temperature T_c under pressures up to 48 GPa revealed a stepwise increase in T_c at the ω–β transition in zirconium [10]. Akahama *et al.* [6] noted the closeness of the temperature T_c and the specific volume of bcc niobium under atmospheric pressure to the respective values obtained for β-Zr under $P = 30$ GPa. These facts were explained by an increase in the *d* band population to a value typical of the group V elements.

Later, structural measurements and measurements of T_c under pressure were carried out for a number of Zr–Ti [11, 12] and Zr–Hf [13] binary alloys. In all the alloys studied, T_c also increased stepwise at the ω–β transition. The isobaric dependences of T_c on the alloy composition, which were obtained from high-pressure experimental data, had a dome like shape similar to that of the corresponding curves obtained for group IV–V alloys at atmospheric pressure [14].

In the framework of the concept of interband electron transfer under pressure, the similarity between the behaviors of Zr and Hf structures under pressure suggests that the pressure dependence of T_c for Hf should be similar to that previously observed for Zr. However, the dependence of T_c on pressure up to the ω–β transition has never been studied experimentally for Hf. In this paper, we describe the measurements of the dependence of T_c on pressure up to 64 GPa for hafnium. In the experimental dependence $T_c(P)$, we reveal anomalies and attribute them to the α–ω–β structural transitions.

2. EXPERIMENT

The metallic Hf used in the experiment was prepared by the zone melting of an iodide Hf bar in vacuum. The purity of the initial metal was no lower than 99.95 at. % with allowance for interstitial impurities. The samples were made by grinding chips of the initial metal to a thickness of ~0.02 mm.

High pressures were obtained using a diamond anvil system made of nonmagnetic materials [15]. The measuring cell is shown in Fig. 1 (the scales are approximately retained). The measuring coil was mounted symmetrically around the anvils, and the reference coil lay in the same plane with the measuring one, at a distance of about 1 mm. The secondary coils were connected against each other. The diameter of the working area of the anvils was about 0.4 mm. The sample and the reference ruby crystals were placed between the anvils in the opening of a metal gasket 0.12 mm in diameter. The pressure medium was a 4 : 1 methanol–ethanol mixture. The pressure was determined by the displacement of the ruby luminescence line with an accuracy of ±0.05 GPa after low-temperature measure-

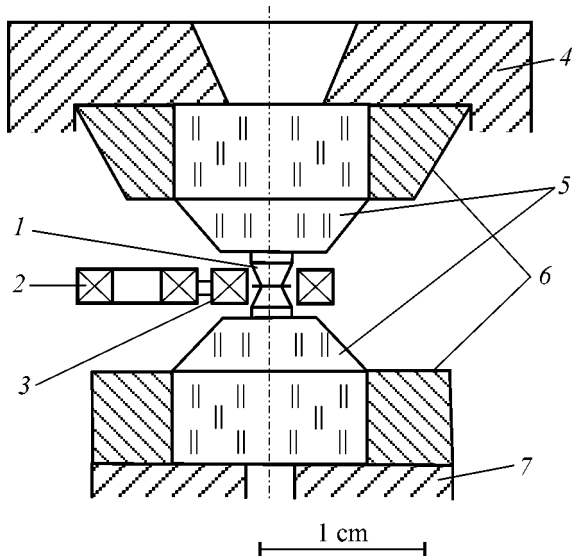

Fig. 1. Pressure cell of the diamond anvil system: (*1*) diamond anvils, (*2*) reference coil, (*3*) measuring coil, (*4*) cylinder of the press, (*5*) sapphire supports, (*6*) supporting rings, and (*7*) piston of the press.

ment cycles with the subsequent heating of the press to room temperature.

The superconducting transitions were detected as anomalies in the temperature dependence of magnetic susceptibility $\chi(T)$, which was measured with a 5.2-kHz alternating current as the sample was heated from the minimum temperature. The minimum temperature equal to 1.3 K was achieved by the vacuum pumping of helium from the cryostat containing the high-pressure system. The temperature was measured with an accuracy of ±0.2 K by a (Cu–Fe)–Cu thermocouple.

The T_c values were determined as the intersection points of the tangent to the steeply dropping part of the $\chi(T)$ curve and the extension of its high-temperature horizontal part.

3. RESULTS

Figure 2 shows typical magnetic susceptibility curves $\chi(T)$ measured by heating the sample in different pressure intervals, and Fig. 3 represents the experimental data as the dependence $T_c(P)$.

At atmospheric pressure, Hf has $T_c = 0.128$ K [1], which is far below the limit of our measurements. For the first time, the anomaly arising in the $\chi(T)$ curve at the beginning of the superconducting transition was observed at a pressure of 31.2 GPa. At the next pressure value of 35.9 GPa, the superconducting transition also occurred near the lower boundary of the measurement range. In the pressure interval P = 40–60.2 GPa, both the beginning and the end of the superconducting transition could be detected in the $\chi(T)$ curves. For all the pressures within this interval, the superconducting transition was spread in temperature over ~1 K. In the pressure interval from 35.9 to 60.2 GPa, the transition points determined as indicated above proved to lie on a single straight line within the measurement accuracy (Fig. 3), and the slope of this line was $dT_c/dP = 0.16 \pm 0.01$ K/GPa. According to the x-ray structural data [5], the α–ω transition in Hf occurs within 38 ± 8 GPa. Hence, the linear dependence in the interval of 35.9–60.2 GPa reflects the behavior of the superconducting transition temperature in ω-Hf. The point determined at 31.2 GPa lies far from this dependence and, presumably, represents the higher temperature of the superconducting transition in α-Hf. In this case, for α-Hf, the slope is $dT_c/dP \approx 0.05$ K/GPa. According to Fig. 3, the

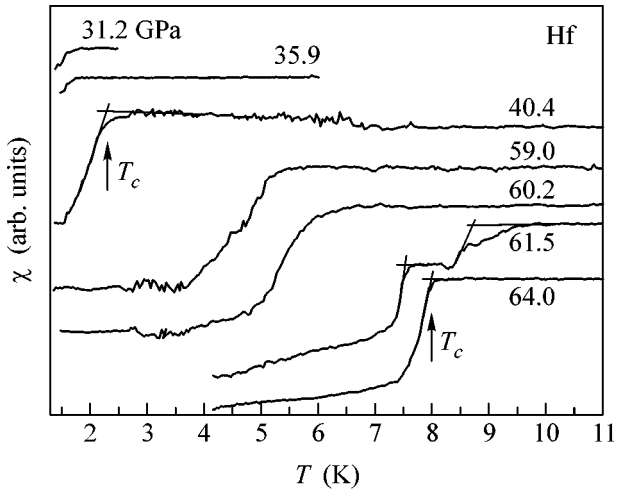

Fig. 2. Magnetic susceptibility curves $\chi(T)$ measured by heating the sample under the different pressures indicated in the plot. The straight lines illustrate the graphical determination of T_c.

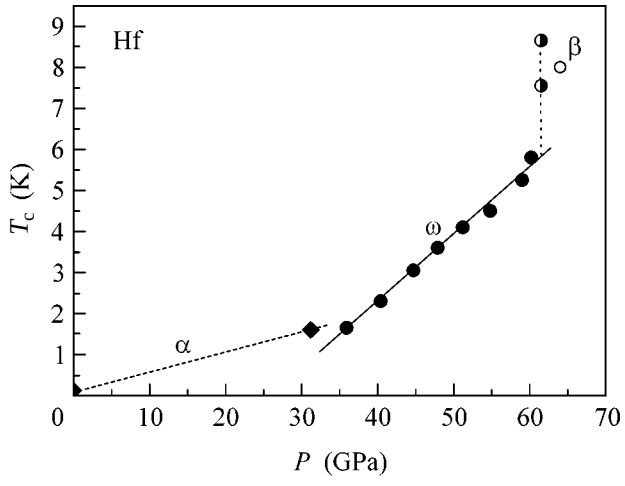

Fig. 3. Pressure dependence of the superconducting transition temperature for Hf. The different kinds of points refer to different phase states of Hf (see the body of the paper).

α–ω structural transformation occurs in Hf between 31.2 and 35.9 GPa. Thus, the pressure and the interval of the α–ω transition that we observed in Hf are noticeably smaller than those obtained from structure studies [5], but the narrow interval of this transition agrees well with the data obtained for Zr [4, 6, 10] and for Zr–Ti and Zr–Hf alloys [11–13].

Under higher pressures, the anomaly of $\chi(T)$ changes. The two-step shape of the jump in $\chi(T)$, which is observed at $P = 61.5$ GPa in Fig. 2 at $T_c = 7.55$ and 8.65 K, is an indication of a two-phase ω + β state of the sample under these conditions. The next measurement at $P = 64.0$ GPa revealed an abrupt jump of $\chi(T)$ at $T_c = 8.0$ K within an interval smaller than 0.5 K. The latter value of T_c lies far above the linear dependence $dT_c(P)$ obtained for ω-Hf and indicates a transition to a new single-phase state of Hf, i.e., to the β phase. The fracture of the pressure cell did not allow us to study the behavior of T_c in the β-Hf stability region.

4. CONCLUSIONS

The α–ω–β structural transitions in Hf are accompanied by changes in T_c, which are similar to those observed in Zr and in Zr–Ti and Zr–Hf alloys. In the regions of stability of the α and ω phases of Hf, the superconducting transition temperatures increase with pressure. The α–ω transition is presumably accompanied by a small decrease in T_c, whereas the ω–β transition is accompanied by a stepwise increase in T_c from 5.8 to 8.0 K.

This work was supported by the Russian Foundation for Basic Research (project no. 03-02-17005) and the Branch of General Physics and Astronomy, Russian Academy of Sciences (Program “Thermal Physics and Mechanics of Intense Pulsed Actions”).

REFERENCES

1. E. Yu. Tonkov, *High Pressure Phase Transformations, A Handbook* (Metallurgiya, Moscow, 1988; Gordon and Breach, Philadelphia, 1992), Vol. 2.
2. Y. K. Vohra and P. T. Spencer, Phys. Rev. Lett. **86**, 3068 (2001).
3. Y. Akahama, K. Nakano, S. Umemoto, *et al.*, Phys. Rev. Lett. **87**, 275503 (2001).
4. H. Xia, S. J. Duclos, A. L. Ruoff, and Y. K. Vohra, Phys. Rev. Lett. **64**, 204 (1990).
5. H. Xia, G. Parthasarathy, H. Luo, *et al.*, Phys. Rev. B **42**, 6736 (1990).
6. Y. Akahama, M. Kobayashi, and H. Kawamura, J. Phys. Soc. Jpn. **60**, 3211 (1991).
7. J. S. Gyanchandani, S. C. Gupta, S. K. Sikka, and R. Chidambaram, J. Phys.: Condens. Matter **2**, 6457 (1990).
8. R. Ahuja, J. M. Wills, B. Johansson, and O. Eriksson, Phys. Rev. B **48**, 16269 (1993).
9. S. A. Ostanin and V. Yu. Trubitsin, Phys. Rev. B **57**, 13485 (1998).
10. Y. Akahama, M. Kobayashi, and H. Kawamura, J. Phys. Soc. Jpn. **59**, 3843 (1990).
11. I. O. Bashkin, V. G. Tissen, M. V. Nefedova, *et al.*, Pis’ma Zh. Éksp. Teor. Fiz. **73**, 80 (2001) [JETP Lett. **73**, 75 (2001)].
12. I. O. Bashkin, V. K. Fedotov, M. V. Nefedova, *et al.*, Phys. Rev. B **68**, 054401 (2003).
13. I. O. Bashkin, M. V. Nefedova, E. G. Ponyatovsky, and V. G. Tissen, Pis’ma Zh. Éksp. Teor. Fiz. **78**, 91 (2003) [JETP Lett. **78**, 80 (2003)].
14. *Superconducting Materials*, Ed. by E. M. Savitskiĭ, Yu. V. Efimov, N. D. Kozlova, *et al.* (Metallurgiya, Moscow, 1976) [in Russian].
15. V. G. Tissen, E. G. Ponyatovskiĭ, V. M. Kulakov, *et al.*, Prib. Tekh. Éksp. **5**, 175 (1986).

Translated by E. Golyamina

JETP Letters, Vol. 80, No. 10, 2004, pp. 658–662. Translated from Pis'ma v Zhurnal Éksperimental'noĭ i Teoreticheskoĭ Fiziki, Vol. 80, No. 10, 2004, pp. 766–770.

Spin–Fluid Approach in the Theory of a Classical Fluid

A. V. Mikheenkov*, A. F. Barabanov*, and L. A. Maksimov**

** Institute for High Pressure Physics, Russian Academy of Sciences, Troitsk, Moscow region, 142190 Russia*
e-mail: mikheenkov@gazeta.ru

*** Russian Research Centre Kurchatov Institute, pl. Kurchatova 1, Moscow, 123182 Russia*

Received September 14, 2004; in final form, October 28, 2004

The simplest model of a two-dimensional fluid is proposed. It is based on the frustrated Heisenberg model that allows qualitative description of the behavior of a pair correlation function for different forms of a two-step potential $U(r)$. The tendency toward the formation of a quasi-bound state is demonstrated for a potential with a local minimum at its repulsive part. It is shown that the fluid can undergo a phase transition upon changing temperature in the case of the two-step potential. © *2004 MAIK "Nauka/Interperiodica".*

PACS numbers: 61.20.Gy; 75.10.Jm

The determination of a pair correlation function (PCF) is an important problem in the theory of fluids. Of particular interest is the determination of a PCF in the case of a potential with a nonmonotonic repulsive part. In this case, the PCF was calculated, e.g., by molecular dynamics simulation [1]. It is believed that such calculations give a considerable insight into the theory of phase transitions even in the 1D and 2D systems, e.g., in water under pressure. The typical forms of the potential in fluid models discussed in the literature [1–3] are shown in Figs. 1a and 1b. Both potentials refer to the class of core-softened potentials, and it is precisely this fact that allows the phase transitions in fluids to be studied using such potentials.

In this work, the simplest lattice model based on the frustrated antiferromagnetic 2D Heisenberg model of a two-dimensional fluid is suggested to qualitatively describe the behavior of the PCF in relation to the form of a two-step potential $U(r)$ (Figs. 1c, 1d). This model is the development of the well-known lattice-gas model [4] that is equivalent to the Ising model and is exactly soluble only for a one-step potential. In contrast to the Ising model, the approach suggested in this work is not static and, moreover, it is applicable to the more complicated potentials.

Figure 1c corresponds to the repulsive potential. The potential shown in Fig. 1d has a minimum at short distances that corresponds to a weak attraction between particles and their covalent bonding.

Let us consider a two-dimensional fluid with the average density ρ_0 and represent the density operator in the form $\hat{\rho} = \rho_0 + \Delta\hat{\rho}$ at each point i, where $\Delta\hat{\rho} = \gamma\hat{S}_i^z$ and the operator $\hat{S}_i^z$ is the spin-projection operator for spin 1/2.

Therefore, we assume that the density fluctuation at each point i is described by the spin wave function; i.e., the density fluctuation for $\Psi = \begin{pmatrix} 1 \\ 0 \end{pmatrix}$ or $\begin{pmatrix} 0 \\ 1 \end{pmatrix}$ is positive or negative, respectively. We are interested in the density–density correlation function $\langle \Delta\hat{\rho}_i \Delta\hat{\rho}_j \rangle$. Since the coefficient γ cannot be calculated within the framework of the suggested approach, the correlation function $\langle \Delta\hat{\rho}_i \Delta\hat{\rho}_j \rangle$ will be determined to an accuracy of a proportional factor.

In the lattice model, the points i are defined on a square lattice. The sites i of this lattice correspond to

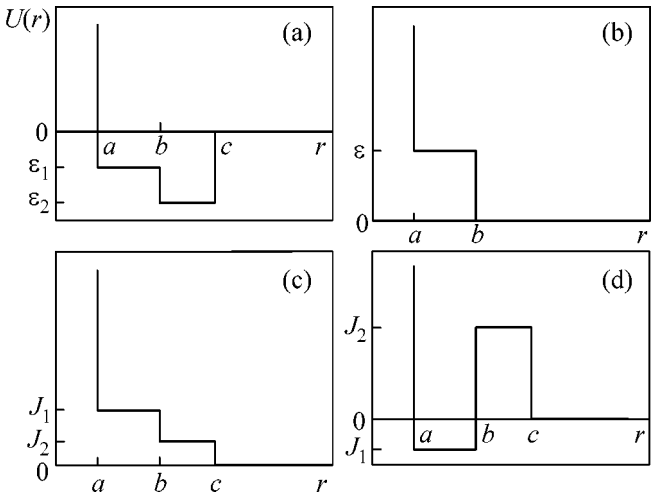

Fig. 1. (a, b) Typical forms of a step potential in the works on the theory of fluids; (c) a two-step potential in the frustrated Heisenberg model with the frustration parameter p = 0.3 (the spin-exchange constants for the first and second nearest neighbors are $J_1 = 0.7$, $J_2 = 0.3$); (d) a two-step potential in the frustrated Heisenberg model with the frustration parameter $p = 1.5$ ($J_1 = -0.5$, $J_2 = 1.5$).

the "probe" points on the plane, so that the lattice constant l should be chosen so as to describe in reasonable detail the significant potential-variation region. Below, we employ the least detailed description of the potential; i.e., $l > a$, $\sqrt{2}\,l > b$, and $2l > c$ (see Fig. 1).

For the system where the density fluctuations can move, the Hamiltonian can be introduced as

$$\hat{H} = \frac{1}{2}J_1\sum_{\mathbf{i},\mathbf{g}}\left\{S_{\mathbf{i}}^z S_{\mathbf{i}+\mathbf{g}}^z + \frac{1}{2}(S_{\mathbf{i}}^+ S_{\mathbf{i}+\mathbf{g}}^- + S_{\mathbf{i}}^- S_{\mathbf{i}+\mathbf{g}}^+)\right\}$$

$$+\frac{1}{2}J_2\sum_{\mathbf{i},\mathbf{d}}\left\{S_{\mathbf{i}}^z S_{\mathbf{i}+\mathbf{d}}^z + \frac{1}{2}(S_{\mathbf{i}}^+ S_{\mathbf{i}+\mathbf{d}}^- + S_{\mathbf{i}}^- S_{\mathbf{i}+\mathbf{d}}^+)\right\} \qquad (1)$$

$$= \frac{1}{2}J_1\sum_{\mathbf{i},\mathbf{g}}\mathbf{S}_{\mathbf{i}}\mathbf{S}_{\mathbf{i}+\mathbf{g}} + \frac{1}{2}J_2\sum_{\mathbf{i},\mathbf{d}}\mathbf{S}_{\mathbf{i}}\mathbf{S}_{\mathbf{i}+\mathbf{d}}.$$

Here, the longitudinal terms correspond to the fluctuation interactions for the nearest J_1 and next-to-nearest J_2 neighbors in the probe lattice (**g** and **d** are the vectors of the first and second neighbors). For the potentials drawn in Figs. 1c and 1d and with the above-mentioned choice of l, the interaction with more distant neighbors is zero.

To characterize the relative heights of the potential steps J_1 and J_2, we use the variable p (frustration parameter) that is adopted in the magnetic problems: $p = J_2/(J_1 + J_2)$, $J_1 = (1-p)J$, $J_2 = pJ$, and, in what follows, $J = 1$.

The transverse terms in the Hamiltonian describe the fluctuation motion. Below, we consider a particular case, where the coefficients of the longitudinal terms and the corresponding transverse terms are identical. Note that the on-site fluctuation repulsion in the model considered is infinite due to the constraints in the spin wave-function space.

Thus, the problem of calculating the fluctuation part of the PCF is reduced to the evaluation of the spin correlation functions $c_{\mathbf{i},\mathbf{j}} = c_{\mathbf{i}-\mathbf{j}} = \langle S_{\mathbf{i}}^z S_{\mathbf{j}}^z\rangle$.

It is essential that, to describe the fluid, the spin problem for a frustrated 2D Heisenberg antiferromagnet should be analyzed within the framework of the approach in which the average values of both the longitudinal and transverse spin components are zero at each site, i.e., within the spin-fluid approach.

For potentials more complicated than the two-step potential, the lattice constant l should be reduced and the model should be generalized to the case of interaction with a large number of nearest neighbors (so that $J_1, J_2, J_3, \ldots, J_n$ adequately describe the potential region corresponding to the first coordination spheres in the fluid). Note that, generally speaking, the probe-lattice sites have no relation to the most probable positions of the particles in the fluid. These positions, in principle, are determined after the calculation of the radial distribution function and correspond to its maxima.

It should be emphasized that the information obtained on the PCF is, generally speaking, sufficient for determining the angle-averaged PCF $h(r)$ and, hence, for determining the isothermal compressibility.

We now briefly describe the computational procedure for the spin correlation functions c_{ij} in our model [5]. The equation of motion for the Green's function $G_{\mathbf{nm}}^z = \langle S_{\mathbf{n}}^z \big| S_{\mathbf{m}}^z\rangle_\omega$ has the form

$$\omega\langle S_{\mathbf{n}}^z | S_{\mathbf{m}}^z\rangle_\omega = i\varepsilon_{z\beta\gamma}\sum_{\mathbf{f}=\mathbf{g},\mathbf{d}} J_f\langle S_{\mathbf{n}+\mathbf{f}}^\beta S_{\mathbf{n}}^\gamma | S_{\mathbf{m}}^z\rangle_\omega, \qquad (2)$$

where $J_g = J_1$ and $J_d = J_2$. At the second step, the Green's function on the right-hand side of Eq. (2) is obtained in the form

$$\omega i\varepsilon_{z\beta\gamma}\sum_{\mathbf{f}=\mathbf{g},\mathbf{d}} J_f\langle S_{\mathbf{n}+\mathbf{f}}^\beta S_{\mathbf{n}}^\gamma | S_{\mathbf{m}}^z\rangle_\omega$$

$$= -2J_1 c_g\sum_{\mathbf{g}}(\delta_{\mathbf{nm}} - \delta_{\mathbf{n}+\mathbf{g},\mathbf{m}})$$

$$-2J_2 c_d\sum_{\mathbf{d}}(\delta_{\mathbf{nm}} - \delta_{\mathbf{n}+\mathbf{d},\mathbf{m}}) \qquad (3)$$

$$+ i\varepsilon_{z\beta\gamma}\sum_{\substack{\mathbf{f}_1=\mathbf{g}_1,\mathbf{d}_1\\ \mathbf{f}_2=\mathbf{g}_2,\mathbf{d}_2}} J_{f_1}J_{f_2}$$

$$\times\langle i\varepsilon_{\beta jl}S_{\mathbf{n}+\mathbf{f}_1+\mathbf{f}_2}^j S_{\mathbf{n}+\mathbf{f}_1}^l S_{\mathbf{n}}^\gamma + i\varepsilon_{\gamma jl}S_{\mathbf{n}+\mathbf{f}_1}^\beta S_{\mathbf{n}+\mathbf{f}_2}^j S_{\mathbf{n}}^l | S_{\mathbf{m}}^z\rangle_\omega.$$

For the three-site terms on the right-hand side of Eq. (3), we use the approximation

$$S_{\mathbf{n}+\mathbf{g}_1+\mathbf{g}_2}^j S_{\mathbf{n}+\mathbf{g}_1}^l S_{\mathbf{n}}^\gamma \approx \alpha_{\mathbf{g}} c_{\mathbf{g}}(\delta_{jl}S_{\mathbf{n}}^\gamma + \delta_{l\gamma}S_{\mathbf{n}+\mathbf{g}_1+\mathbf{g}_2}^j)$$
$$+ \alpha_{\mathbf{g}_1+\mathbf{g}_2}c_{\mathbf{g}_1+\mathbf{g}_2}\delta_{j\gamma}S_{\mathbf{n}+\mathbf{g}_1}^l. \qquad (4)$$

Here, $\mathbf{g}_1 + \mathbf{g}_2 \neq 0$; the trivial term with $\mathbf{g}_1 + \mathbf{g}_2 = 0$ is found exactly; and α are the vertex corrections, whose choice is discussed in detail in [5]. In this approach, the damping of the Green's function is absent; i.e., this approach corresponds to the mean-field approximation in the spin-fluid model. Note that, beyond the mean-field approximation and with allowance for the damping, this problem encounters considerable difficulties [6] (similarly to the case of a traditional two-sublattice state [7]).

In the **k** space, the Green's function G^z takes the form

$$G_{\mathbf{k},\omega}^z = \langle S_{\mathbf{k}}^z | S_{-\mathbf{k}}^z\rangle_\omega = \frac{F(\mathbf{k})}{\omega^2 - \omega^2(\mathbf{k})}, \qquad (5)$$

where

$$F(\mathbf{k}) = -2[J_1 c_g z_g(1-\gamma_g(\mathbf{k})) + J_2 c_d z_d(1-\gamma_d(\mathbf{k}))],$$

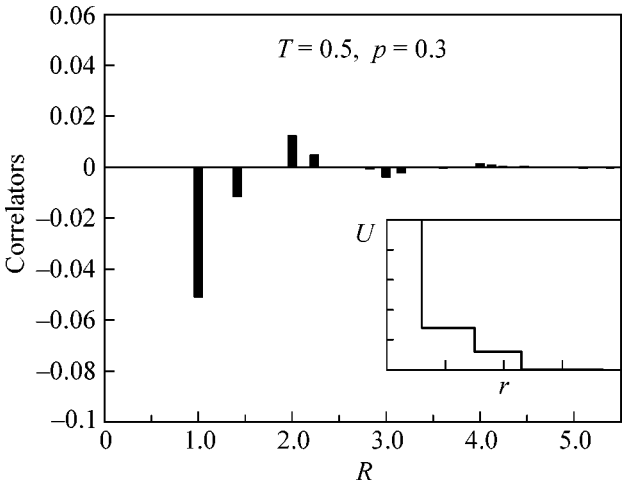

Fig. 2. Spin correlation function (proportional to the pair density–density correlation function) vs. the distance R between the lattice sites (in the units of the lattice constant l) for $T = 0.5J$ and $p = 0.3$. The form of the potential is shown in the inset.

$$\omega^2(\mathbf{k}) = 2[(\gamma_1 K_1 + \gamma_2 K_2) - (\gamma_3 K_3 - \gamma_4 K_4) - (\gamma_5 K_5 + \gamma_6 K_6)].$$

The quantities K_1–K_6 in the expression for the spectrum are

$$K_1 = J_1 J_2 K_{gd} + J_1^2 \tilde{c}_g z_g (z_g - 1) + \frac{z_g}{4} + K_{gg},$$

$$K_2 = J_1 J_2 K_{gd} + J_2^2 \tilde{c}_d z_d (z_d - 1) + \frac{z_d}{4} + K_{dd},$$

$$K_3 = J_1^2 \tilde{c}_g z_g^2; \quad K_4 = J_2^2 \tilde{c}_d z_d^2,$$

$$K_5 = J_1 J_2 \tilde{c}_g z_g z_d,$$

$$K_6 = J_1 J_2 \tilde{c}_d z_g z_d,$$

$$K_{gg} = \sum_{\substack{\mathbf{r} = \mathbf{g}_1 + \mathbf{g}_2 \\ \mathbf{g}_1 \neq -\mathbf{g}_2}} \tilde{c}_r; \quad K_{dd} = \sum_{\substack{\mathbf{r} = \mathbf{d}_1 + \mathbf{d}_2 \\ \mathbf{d}_1 \neq -\mathbf{d}_2}} \tilde{c}_r; \quad K_{gd} = \sum_{\mathbf{r} = \mathbf{g} + \mathbf{d}} \tilde{c}_r,$$

where $\tilde{c}_r = \alpha_r c_r$ are the correlation functions including the vertex corrections; α_r, z_g, and z_d are the numbers of the nearest and next-to-nearest neighbors in the probe lattice (in our case, $z_g = z_d = 4$); and

$$\gamma_g(\mathbf{k}) = \frac{1}{z_g}\sum_{\mathbf{g}} e^{-i\mathbf{k}\mathbf{g}} = \frac{1}{2}(\cos(k_x) + \cos(k_y)),$$

$$\gamma_d(\mathbf{k}) = \frac{1}{z_d}\sum_{\mathbf{d}} e^{-i\mathbf{k}\mathbf{d}} = \cos(k_x) * \cos(k_y).$$

The functions $F(\mathbf{k})$ and $\omega^2(\mathbf{k})$ include correlation functions $c_\mathbf{r}$ for the first five coordination spheres. Expressing them in terms of the Green's function $G^z_\mathbf{q}$

$$c^z_\mathbf{q} = \langle S^z_\mathbf{q} S^z_{-\mathbf{q}} \rangle = -\frac{1}{\pi}\int d\omega m(\omega) \mathrm{Im} G^z_\mathbf{q}$$

$$= \frac{F(\mathbf{q})}{2\omega(\mathbf{q})}(2m(\omega_\mathbf{q}) + 1); \quad m(\omega) = (e^{\omega/T} - 1)^{-1},$$

one obtains the system of self-consistent equations that can be solved numerically:

$$c_\mathbf{r} = \frac{1}{(2\pi)^2}\int d\mathbf{q} c^z_\mathbf{q} \gamma_{n,m}(\mathbf{q}); \quad \mathbf{r} = n\mathbf{g}_x + m\mathbf{g}_y,$$

$$\gamma_{n,m}(\mathbf{q}) = \frac{1}{z}\sum e^{-i\mathbf{q}\mathbf{r}}$$

$$= \frac{1}{2}(\cos(nk_x)\cos(mk_y) + \cos(mk_x)\cos(nk_y)).$$

After determining $c^z_\mathbf{q}$ from these expressions, one can find the correlation function $c_\mathbf{r}$ for any $\mathbf{r}$.

Below, we present the results obtained for c_{ij} for two potential types: the first corresponds to the net repulsion (Fig. 1c; $J_1 > J_2 > 0$ and $p = 0.3$) and the second corresponds to the potential with a local minimum at short distances (Fig. 1d; $J_1 < 0$, $J_2 > 0$, and $p = 1.5$). Unless otherwise indicated, all the further results are presented for the temperature $T = 0.5J$. Physically, the second case corresponds to the situation where the particles tend to form covalent bonds upon their approaching each other. The correlation functions $c(\mathbf{r})$ ($\mathbf{r}$ is the probe-lattice site) for the first case are given in Fig. 2. Their behavior corresponds to the standard $h(r)$ dependence; at short distances (in our case, for the first two nearest neighbors in the probe lattice), $c_1 = c(\mathbf{g}) < 0$ and $c_2 = c(\mathbf{d}) < 0$; and the positive values of the next correlation functions $c_3 = c(2\mathbf{g})$ and $c_4 = c(\mathbf{g} + \mathbf{d})$ describe the first maximum of the function $h(r)$. In the second case (Fig. 3), c_1 changes sign and becomes positive, though small, while c_3 remains positive. This fact can be treated as the splitting of the first maximum of $h(r)$, indicating a tendency to the formation of a quasi-bound state by two particles when going from the potential in Fig. 1c to the potential in Fig. 1d.

Note that a similar situation occurring in the two-dimensional case with a fixed two-step core-softened potential of the form shown in Fig. 1a (both steps are negative) and the variable density was discussed in [1, 2]. The problem was solved by the molecular dynamics methods. With an increase in the density, the transition was observed from "open" structures to "dense" structures in which particles could penetrate into the soft core. For the dense structure, the first peak of $h(r)$ splits into two peaks and the intensity of the near peak increases with the density. The possibility of transition

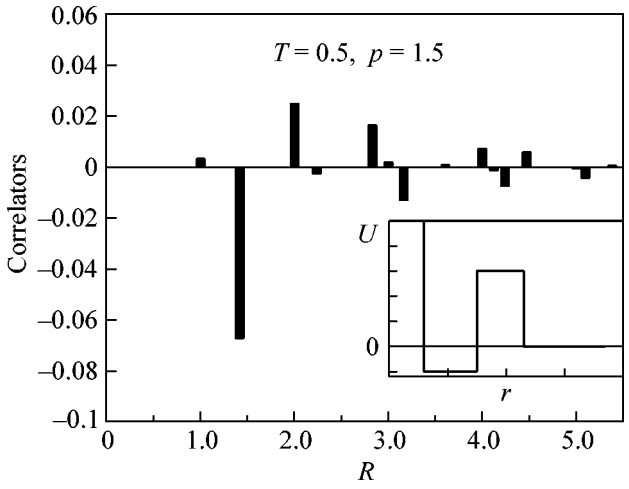

Fig. 3. Same as in Fig. 2, but for $p = 1.5$.

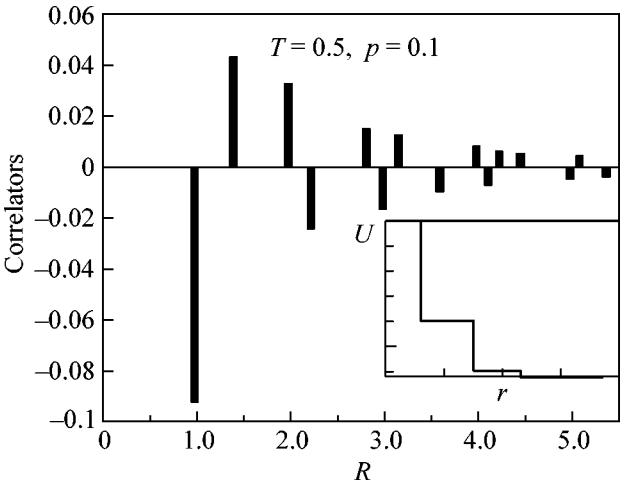

Fig. 4. Same as in Fig. 2, but for $p = 0.1$.

in the fluid for the core-softened (one-step) potential was also discussed in [3] using the thermodynamic perturbation theory.

We now demonstrate what happens if the height J_2 of the second step in the two-step potential decreases relative to J_1, e.g., if one goes from the case shown in Fig. 1c ($p = 0.3$) to $p = 0.1$. The comparison of Figs. 2 and 4 shows that a change in $h(r)$ mainly leads to a noticeable leftward shift of the first maximum. In addition, the oscillations in $c(\mathbf{r})$ become more pronounced.

Let us consider the influence of temperature on the behavior of $c(\mathbf{r})$ in a fixed potential (i.e., frustration in our case). In Fig. 5, the correlation functions are drawn for several temperatures and $p = 0.6$ (the corresponding potential is shown in the inset). One can see that, as the temperature increases from $T = 0.25$ to $T = 0.75$, the absolute values of c_2 and c_1 decrease and increase, respectively. This behavior corresponds to the increase in the population of the second step. No self-consistent solution exists in the temperature interval $T \simeq 0.75$–1.0. However, the solution again appears at $T \gtrsim 1.0$, but its character is qualitatively different from the low-temperature behavior. Namely, c_1 and c_2 change drastically: the relative populations of the first and second steps change stepwise, evidencing the liquid–liquid phase transition. The question of the phase-transition kind (first or second) cannot be answered within our approximation, because, to do this, one should abandon the self-consistent approach that preserves the Hamiltonian SU(2) symmetry.

Among the alternative methods of studying the 2D square frustrated Heisenberg model, we point to the

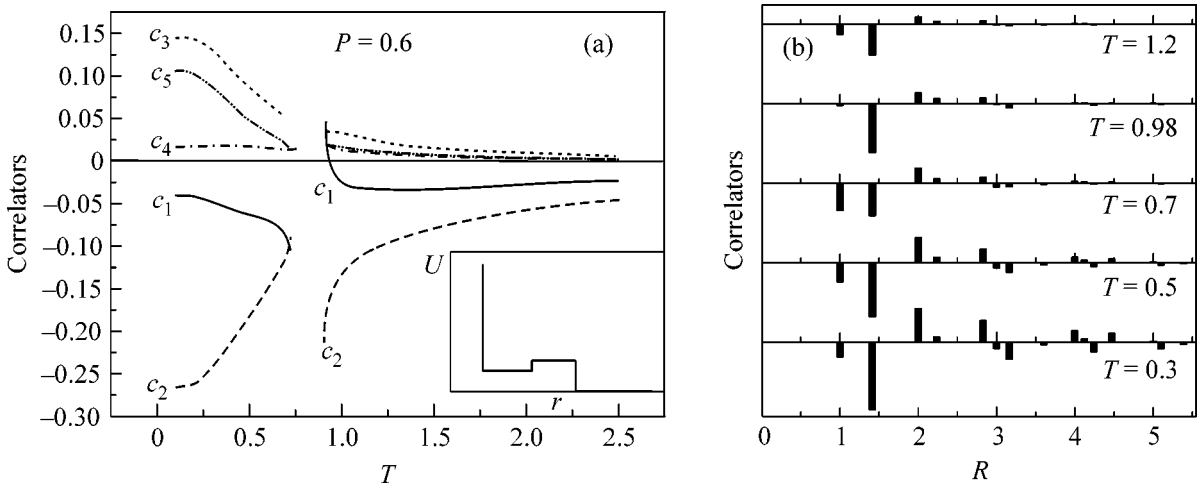

Fig. 5. (a) Temperature dependence of the first five spin correlation functions for $p = 0.6$ ($J_1 = 0.4$, $J_2 = 0.6$). In the phase-transition region (at T close to 0.8 J), no self-consistent solution exists. The form of the potential is shown in the inset. (b) The spin correlation function vs. the distance between the sites R for $p = 0.6$ and several temperatures.

calculation of the perturbation series for the susceptibility of finite-size clusters, the quantum Monte-Carlo method, and the methods of exact cluster diagonalization (for detail, see, e.g., review [8]). However, in the frustration regime at finite temperatures, none of these methods can reliably distinguish the states with spontaneous symmetry breaking (the box phase, the columnar dimerized spin-fluid phase, and the plated phase) and the spin-fluid state considered in this work. Moreover, it is difficult to find the spin correlation functions within the framework of a unified approach using the above-mentioned alternative methods over broad frustration and temperature intervals and to study a model with longer-range interactions.

The development of our approach is of interest primarily in the following directions. Since it is based on the isotropic Heisenberg model, the kinetic energy of the density fluctuations (transverse terms) and the potential energy (longitudinal terms) are determined by the same constant J. The spin-fluid consideration of the frustrated anisotropic Heisenberg model would be more realistic. To our knowledge, such an approach is lacking as yet within the framework of spin-fluid theories. One more line of investigation is a more accurate analysis of the effect of the potential form (addition of the third step) on the phase transition and on the possibility of forming a quasi-molecular state. The second open problem is the analysis of the change in the short-range order upon the transition, i.e., the investigation of not only square but also other lattices.

Within our approach, it is impossible to analyze the effect of a change in pressure and density on the behavior of $c(\mathbf{r})$. We note, however, that the two-dimensional molecular dynamics simulation [2] indicates that an increase in temperature is qualitatively equal to an increase in pressure.

Thus, a lattice spin–fluid approach to the classical fluid has been suggested in this work. It is based on the Heisenberg model and provides a description of the behavior of the total correlation function with a change in the temperature and the potential form.

We are grateful to V.N. Ryzhov and V.V. Brazhkin for discussion of the results. This work was supported by the Russian Foundation for Basic Research.

REFERENCES

1. S. V. Buldyrev *et al.*, in *Proceedings of NATO Advanced Research Workshop on New Kinds of Phase Transitions: Transformations in Disordered Substances, Volga River*, Ed. by V. V. Brazhkin, S. V. Buldyrev, V. N. Ryzhov, and H. E. Stanley (Kluwer Academic, Dordrecht, 2002), p. 97.
2. M. R. Sadr-Lahijany, A. Scala, S. V. Buldyrev, and H. E. Stanley, Phys. Rev. Lett. **81**, 4895 (1998).
3. V. N. Ryzhov and S. M. Stishov, Phys. Rev. E **67**, 010201 (2003).
4. R. J. Baxter, *Exactly Solved Models in Statistical Mechanics* (Academic, New York, 1982; Mir, Moscow, 1985).
5. A. F. Barabanov, L. A. Maksimov, and A. V. Mikheenkov, in *Spectroscopy of High-T_c Superconductors: A Theoretical View*, Ed. by N. M. Plakida (Taylor and Francis, London, 2003), p. 1.
6. A. F. Barabanov and L. A. Maksimov, Phys. Lett. A **207**, 390 (1995).
7. S. Tyc and B. I. Halperin, Phys. Rev. B **42**, 2096 (1990).
8. G. Misguich and C. Lhuillier, cond-mat/0310405 (2003).

Translated by V. Sakun

JETP Letters, Vol. 80, No. 10, 2004, pp. 663–673. Translated from Pis'ma v Zhurnal Éksperimental'noĭ i Teoreticheskoĭ Fiziki, Vol. 80, No. 10, 2004, pp. 771–783.

Spatial–Temporal Ion Structures in the Earth's Magnetotail: Beamlets as a Result of Nonadiabatic Impulse Acceleration of the Plasma

L. M. Zelenyĭ[1], E. E. Grigorenko[1, 2], and A. O. Fedorov[1, 3]

[1] *Space Research Institute, Russian Academy of Sciences, ul. Profsoyuznaya 84/32, Moscow, 117810 Russia*
e-mail: lzelenyi@iki.rssi.ru

[2] *Skobel'tsyn Institute of Nuclear Physics, Moscow State University, Vorob'evy gory, Moscow, 119899 Russia*
e-mail: elenagrigorenko2003@yahoo.com

[3] *Centre d'Etude Spatial des Rayonnnements, 4346-31028 Toulouse, France*

Received October 13, 2004

The properties of high-energy ion beams (beamlets) observed in the boundary layer of the plasma sheet of the Earth's magnetotail during short time intervals (1–2 min) have been considered. Beamlets are induced by nonlinear impulse accelerating processes occurring in the current sheet of the far regions of the geomagnetic tail. Then, moving toward the Earth along the magnetic field lines, they are detected in the magnetotail (in the plasma sheet boundary layer) and in the high-latitude part of the auroral zone in the form of short bursts of high-energy ions (with energies of several tens of keVs). The size of the localization region of the beamlets in the magnetotail and auroral zone has been determined by the epoch-superposition method, and it has been shown that beamlets are concentrated in a narrow region near the plasma sheet boundary, whose latitude size is no more than 0.8°. This conclusion corroborates the theoretical prediction that the nonadiabatic resonant acceleration of ions occurs in a spatially localized region near the separatrix separating the open magnetic field lines and closed field lines, which contain the hot and isotropic plasmas of the plasma sheet. Based on the CLUSTER multisatellite measurements, the spatial structure of beamlets is analyzed and it has been found that the Alfvén wave arises due to the excitation of fire-hose instability at the instant of the exit of the ion beam from the current sheet to the high-latitude region of the far tail of the Earth's magnetosphere. The longitudinal (along the magnetic field) and transverse sizes of a beamlet are estimated. It has been found that the beamlet is a dynamic plasma structure whose longitudinal size is several hundred times larger than its transverse size. © *2004 MAIK "Nauka/Interperiodica".*

PACS numbers: 94.30.Ej; 94.30.Gm

INTRODUCTION

The geomagnetic tail of the Earth's magnetosphere has attracted the attention of researches since its discovery in the late 1960s as one of the complex and interesting objects in space physics. It is formed on the night side of the Earth due to the elongation of the magnetic field lines of the Earth by the solar wind plasma flow, which moves continuously from the Sun (Fig. 1). From the plasma physics point of view, the geomagnetic tail is a vast self-consistent magneto-plasma configuration ($\beta \approx 1$), where energy coming in the magnetosphere from the solar wind is accumulated. This energy is then released either explosively, causing magnetic substorms, or by small portions through the acceleration of particles. Charged particles entering the magnetosphere, predominantly from the ionosphere and solar wind (primarily from the solar wind excluding disturbed periods), are accelerated in the current sheet of the magnetotail to very high velocities (about several thousands of kilometers per second). The mystery of such an unusually effective acceleration of the plasma in the Earth's magnetotail has stimulated numerous theoretical and experimental investigations for several decades. In the late 1980s, it was understood that the ion acceleration in the current sheet must occur near the separatrix separating the closed magnetic field lines that intersect the current sheet, which are filled with the hot plasma of the plasma sheet from the open field lines of the high-latitude part of the tail (one of the ends of the latter lines are connected with the ionosphere and the other ends are in the solar wind) [1–3]. The ion fluxes accelerated in the separatrix region, then, move toward the Earth within a narrow region located along the boundary separating the plasma sheet from the comparatively empty (at least, without the hot plasma) high-latitude region of the tail (Fig. 2). This transition region separates the two half-spaces with the different topologies of the magnetic field and different plasma regimes; i.e., it is a near-separatrix layer, and it is called the plasma sheet boundary layer (PSBL). Thus, the PSBL, as a mirror, reflects the complex nonlinear acceleration processes that occur in the far tail and cannot be

0021-3640/04/8010-0663$26.00 © 2004 MAIK "Nauka/Interperiodica"

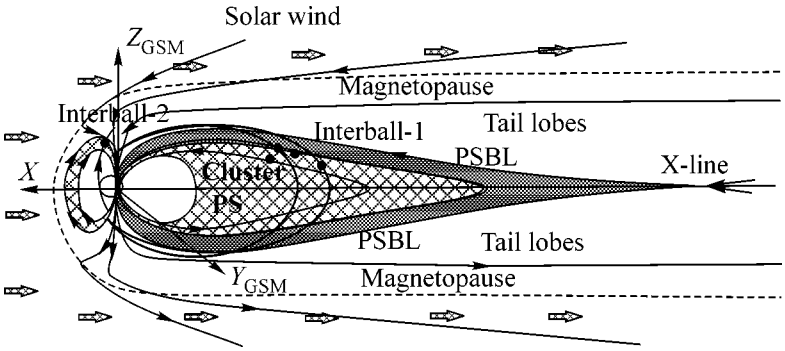

Fig. 1. Magnetosphere structure and the orbits of the Interball-1, Interball-2, and CLUSTER satellites.

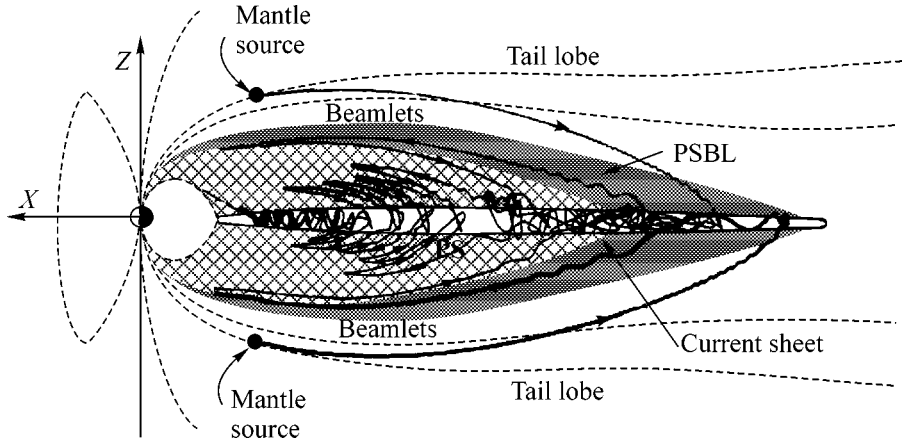

Fig. 2. Trajectories of particles in the (*X*, *Z*) plane that move from the mantle source and interact with the current sheet. In the dependence of the local conditions in the interaction region, particles can either undergo strong scattering and be captured within the current sheet or leave the current sheet and move along the Speiser orbits toward the Earth. These particles form beamlets observed in the plasma sheet boundary layer.

measured *in situ*. Moreover, this region is a channel through which energy released in the far regions of the tail enters the inner magnetosphere. It was previously thought that the source of the ion acceleration in the current sheet is the large-scale reconnection described by the well-known Petschek model; hence, the accelerated plasma fluxes that are generated by it and then collimated in the PSBL should also be large-scale [4, 5]. In view of this circumstance, it was also thought that the appearance of the accelerated plasma fluxes at the plasma sheet boundary was associated with the development of substorms; i.e., the PSBL exists only during active periods [6]. More recently, owing to numerous observations carried out in the tail by the ISEE-1 and ISEE-2 satellites, it has been understood that the PSBL is a continuously existing part of the tail, because it is observed during long quiet periods.

In many theoretical works [7, 8], it was shown that the ions in the current sheet do not have smooth adiabatic trajectories. They chaotically move along much more complex nonadiabatic trajectories, because their motion cannot be described by the leading center approximation that is broken in this case. Such particles can undergo strong stochastic scattering when intersecting the current sheet, and their motion sometimes can be completely chaotic [9–11]. The behavior of a particle after its interaction with the current sheet is determined by the so-called adiabaticity parameter $K = \sqrt{R_{curv}/\rho_{max}}$, where R_{curv} is the local curvature radius of the magnetic field lines and ρ_{max} is the maximum Larmor radius of the particle.

In the dependence of the K value, particles can either undergo strong scattering and be captured in the current sheet or leave the current sheet, moving in the PSBL along open (so-called Speiser) orbits (Fig. 2). More recently, the analytical theory [10] was corroborated by the numerical simulation based on the large-

scale kinetic model of the ion motion in the current sheet [12]. It was shown in [12] that the accelerated ion fluxes moving in the PSBL are not large-scale structures and are rather a set of many spatially separated ion beams whose velocity increases with the altitude of their observation over the neutral sheet. These ion beams were called beamlets. More recently, the numerical simulation results were corroborated by numerous experimental observations [13–16]. Thus, the complex structure of the PSBL represents the nonlinear self-consistent magneto-plasma configuration of the magnetotail, which is in stable equilibrium due to the balance between the plasma inflow from the plasma mantle source and the losses of particles due to their nonadiabatic motion in the tail. The quasi-equilibrium oscillations of the system that arise due to the instantaneous disbalancement between the inflow of particles and their losses occur with a period of 1–5 min [17]. This period corresponds to the characteristic time scales of the observation of beamlets in the PSBL [13–15]. However, experimental evidence explaining the short time of beamlet observations has not yet been obtained. In other words, it is not clear whether beamlets are spatial or temporal structures. In early works devoted to the kinetic simulation of the processes of the nonadiabatic acceleration of ions in the stationary model of the tail, it was supposed that beamlets are spatially localized long-lived structures [12]. In this case, the short observation time of beamlets is associated with the motion of the plasma sheet boundary with respect to a satellite (the so-called flapping of the plasma sheet). Owing to this flapping, the satellite detects a beamlet only for a short time. At the same time, the time of beamlet generation in the source can be limited to several minutes. More recent works devoted to the simulation of the self-consistent configuration of the geomagnetic tail [17, 18] show that the finite lifetime of the source can significantly affect their observable manifestations.

The particles from transient plasma structures that move toward the Earth in the PSBL must finally precipitate in the auroral zone. The remaining part of the plasma is reflected from the regions of the strong magnetic field near the Earth, returns to the tail, and is later isotropized (Fig. 2). Numerous investigations were devoted to various structures observed at the plasma sheet boundary in the auroral zone. Among such structures are primarily velocity dispersed ion structures (VDISs) and time-dispersed ion structures (TDISs). The former structures are typical spatial structures [19] and are observed for several tens of minutes. The latter structures are time-of-flight structures with a source located in the equatorial plane comparatively close to the Earth (7–40 R_E, where R_E is the Earth's radius). The appearance of these structures in the auroral zone is usually associated with the development of a substorm [20, 21]. There is one more mysterious and interesting type of structure, the observation of which will be discussed in this work. We consider structures of this type separately from the above structures, because they are observed during absolutely quiet periods in contrast to TDISs and they are short (no longer than several minutes) in contrast to VDISs and have no virtually internal dispersion. It was shown in [22] that such undispersed structures, which were detected near the high-latitude boundary of the plasma sheet in the auroral zone, are beamlets precipitating from the tail. In this work, we perform a comparative statistical analysis of the duration of the beamlets observed in the tail and auroral zone in the framework of the international multisatellite project Interball. Moreover, we attempt to separate the time and spacial effects in the observation of the beamlets. In addition, we present new data of observation of beamlets by the satellites of the European project CLUSTER. These satellites conduct measurements simultaneously at four points spaced by distances of about 2000 km. These latest data with high time resolution (compared to the Interball satellite measurements) allow the determination of new properties of beamlets that were unknown previously.

2. EXPERIMENTAL DATA

The Interball-1 satellite was launched on August 3, 1995, for studying the boundary layers of the Earth's magnetosphere, including the PSBL, which are very important and interesting from the plasma physics point of view. Owing to its orbit, the satellite was present in the high-latitude regions of the tail and in the PSBL for a long time. In this respect, the Interball-1 had an undeniable advantage for studying the PSBL over other satellites performing measurements in the tail. In each passage through the tail, the Interball-1 satellite intersected its high-latitude part, the PSBL, and the plasma sheet (Fig. 1). In this work, we analyze 42 intersections of the PSBL by the Interball-1 satellite at a distance of $X \sim -25\ R_E$. We use the data obtained with the Russian instruments: the magnetic field obtained with the MIF magnetometer and the plasma parameters obtained by the CORALL ion spectrometer.

The measurements in the auroral zone were carried out by the Interball-2 satellite. The plasma data were obtained by the Russian–French ion spectrometer ION. We analyzed 52 intersections of the high-latitude boundary of the plasma sheet by the Interball-2 satellite under quiet geomagnetic conditions at altitudes of about 3 R_E.

The project CLUSTER involving four satellites (Fig. 1) started in summer 2000. Each year from July to October, their orbits pass through the magnetotail and intersect the plasma sheet from the north to the south. During this period, the distances in this satellite quartet vary from 1500 to 3000 km. In this work, we use the measurements from the HIA (hot plasma analyzer) ion spectrometer and the measurements of the magnetic field from the FGM magnetometer with a resolution of 4 s.

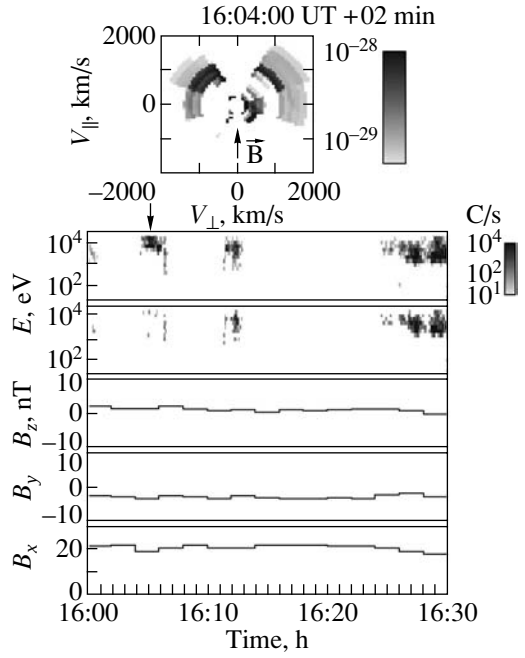

Fig. 3. Beamlet observed by the Interball-1 satellite in the high-latitude part of the magnetotail on November 25, 1996. The Interball-1 position: $X = -28\ R_E$, $Y_{GSM} = 1.4\ R_E$, and $Z_{GSM} = 2.6\ R_E$. The upper panel shows the characteristic shape of the velocity distribution function of ions in the beamlet as measured at the time marked by the arrow in the upper part. The distribution function was measured for 2 min and is plotted in the system of the ion velocity components $V_\perp$ (km/s) and $V_\|$ (km/s) perpendicular and parallel to the magnetic field, respectively. The lower panel shows the ion spectrogram plotted in the time–energy (eV) system. The count rate is shown by the gray tones according to the scale shown in the right part of the figure. (From top to bottom) The spectrogram measured by the detector faces the tail (the arrow indicates the beamlet) the spectrogram measured by the detector faces the Sun and the time dependence of the $B_{Z_{GSM}}$, $B_{Y_{GSM}}$, and B_X magnetic field components.

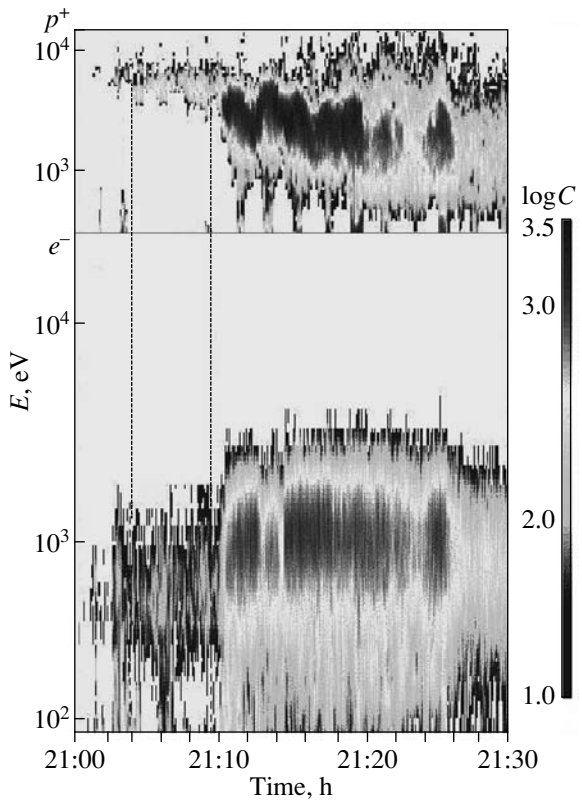

Fig. 4. (Dashed lines) Beamlet observed by the Interball-2 satellite near the high-latitude boundary of the plasma sheet in the auroral zone on August 26, 1997. The Interball-2 position: an invariant latitude of 73.5°, a radial distance from the Earth of 2.65 R_E, and a local time of 2.00. (From top to bottom) The ion spectrogram in the time–energy system and the electron spectrogram.

3. EXPERIMENTAL OBSERVATION OF BEAMLETS BY THE INTERBALL-1 AND INTERBALL-2 SATELLITES

3.1. Observations of Beamlets in the Magnetotail

On the spectrograms measured in the PSBL of the magnetotail, beamlets are manifested as short bursts of high-energy ions (with an energy of several tens of keVs) with a duration of 1–2 min. Velocity dispersion is not usually observed in an individual event. All the observations of beamlets in the PSBL are accompanied by a decrease in the magnetic field magnitude (diamagnetic effect). The velocity distributions of the beamlets have the shape of Peru beans [14, 23–25]. On spectrograms, they can be either isolated from the plasma sheet or observed at the boundary with the plasma sheet. Unfortunately, measurements conducted only at one point are insufficient for definitely concluding whether beamlets are structures isolated from the plasma sheet or they are connected with the plasma sheet and occur at its boundary. Figure 3 shows a typical example of a beamlet observed in the tail by the Interball-1 satellite. The satellite flew from the high-latitude region toward the plasma sheet. When the satellite was in the high-latitude region (it is seen from the data on the magnetic field that reaches a high value of 30 nT in this region), on the spectrogram recorded by the detector faces against the Sun, a short ion beam (beamlet) with an energy of about 10 keV and a duration of about 1 min is observed and it is accompanied by a local decrease in the magnetic field magnitude. As seen in the distribution function, the beamlet moves to the Earth with high velocity predominantly along the magnetic field. Unfortunately, the CORALL instrument had a blind angle along the rotation axis (Sun–Earth line). For this reason, the distribution function has a gap in the angular sector corresponding to the velocity directed along the magnetic field.

3.2. Observation of Beamlets in the High-Latitude Part of the Auroral Zone

Figure 4 shows the Interball-2 observation of the undispersed structure of precipitating ions in the auroral zone near the high-latitude boundary of the plasma sheet at 21:02–21:09 on August 26, 1997. The duration of this event was equal to 7 min, which was uniquely long for such a structure. This event was observed under absolutely quiet geomagnetic conditions. An interesting feature of such events is the simultaneous observation of comparatively cold electrons ($E \sim$ 300–400 eV), which noticeably differ from the plasma sheet electrons, whose energies are usually higher than 1 keV. This is one more piece of evidence that the phenomena under consideration are observed in the boundary layer beyond the plasma sheet. Such events are the traces of beamlets precipitating in the high-latitude region of the auroral zone from the magnetotail [22].

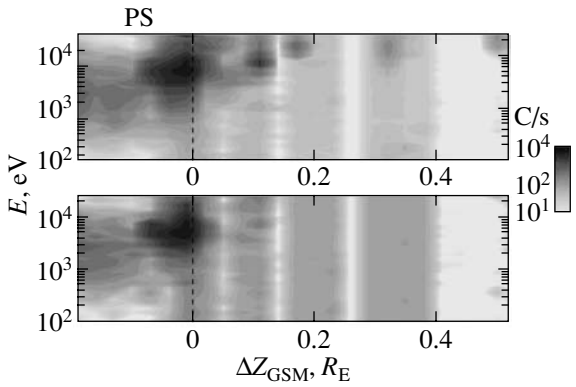

Fig. 5. Ion spectrogram obtained by the epoch-superposition method applied to the 42 intersections of the plasma sheet boundary layer in the magnetotail by the Interball-1 satellite in the quiet geomagnetic intervals. The spectrogram is plotted in the (ΔZ–ion energy) system, where ΔZ is the distance between the satellite and (dotted line) the plasma sheet boundary. The count rates in the detectors are shown by the gray tones according to the scale shown in the right part of the figure. The upper and lower panels are the data from the detectors facing the tail and the Sun, respectively.

4. STATISTICAL ANALYSIS OF BEAMLETS OBSERVED IN THE TAIL AND AURORAL REGION

The detection of the beamlet in only one point is insufficient for separating the time and spatial effects forming the resulting observable pattern; i.e., it is impossible to estimate the actual duration and spatial size of the beamlet. In addition, nothing can be said about the spatial size of the region where beamlets are located. Nevertheless, having extensive measurements, one can attempt to solve these problems by statistical methods. For the statistical analysis of the spatial distributions of beamlets in the tail and in the high-latitude part of the auroral zone, we first take intervals when the Interball-1 and Interball-2 satellites intersect these magnetosphere regions in the midnight sector ($|Y_{GSM}| \le 7\ R_E$ for the tail and 21.00 h < MLT < 03.00 h for the auroral zone) and in the quiet geomagnetic intervals (AE < 100 nT). We remember that the GSM coordinate system includes the X axis directed to the Sun (along the Earth–Sun line), the Z axis directed along the axis of the Earth's magnetic dipole, and Y axis complementing the right-handed coordinate system (Fig. 1). As a result, 42 intersections of the PSBL in the magnetotail and 52 intersections of the high-latitude boundary of the plasma sheet in the auroral zone were selected.

Figure 5 shows the spectrogram obtained by the epoch-superposition method applied to all the selected intersections of the PSBL in the tail. The spectrogram is plotted in the ΔZ energy coordinates, where ΔZ is the distance between the satellite and the plasma sheet boundary (along the Z_{GSM} direction). The plasma sheet boundary was determined separately for each intersection of the PSBL according to the following criteria: (i) ion temperature $T_i > 1$ keV and (ii) approximately identical count rates in all five polar channels of the CORALL instrument (the differences must be no more than 30%). Thus determining the plasma sheet boundary in each specific passage, we assign $dZ = 0$ to it. As a result, the region $dZ > 0$ is the high-latitude part of the tail and the region $dZ < 0$ is the inner part of the plasma sheet. The spectrogram from the high-latitude region clearly demonstrates beamlets moving from the tail. Thus, the size of the region (along the Z_{GSM} direction) where beamlets are observed is statistically estimated as 0.5 R_E (or 0.5° of the invariant latitude).

A similar method was applied to the intersections of the auroral zone by the Interball-2 satellite. According to the auroral data, the latitude size of the region where beamlets are observed is equal to about 0.8°. Thus, we obtained similar results for the size of the beamlet localization region in the tail and auroral zone of the magnetosphere. Thus, we found that beamlets are observed within a very narrow latitude region near the plasma sheet boundary. As is seen in Fig. 5, the probability of their observation decreases when the distance from the plasma sheet boundary increases.

Although we have data on the observation of beamlets at two points (in the tail and auroral zone), it is unfortunately impossible to detect the same beamlet in both regions of the magnetosphere and thereby to separate the time and spacial effects in its observation. The only method that can be applied is the statistical comparison of the beamlet observation durations in the tail and auroral zone. Figure 6 shows the probability of the observation of beamlets in the (a) auroral zone and (b) tail as a function of the event duration. It is seen that the distributions in both magnetosphere regions are similar to each other: the mean duration of the beamlet observations in the tail and auroral zone is equal to

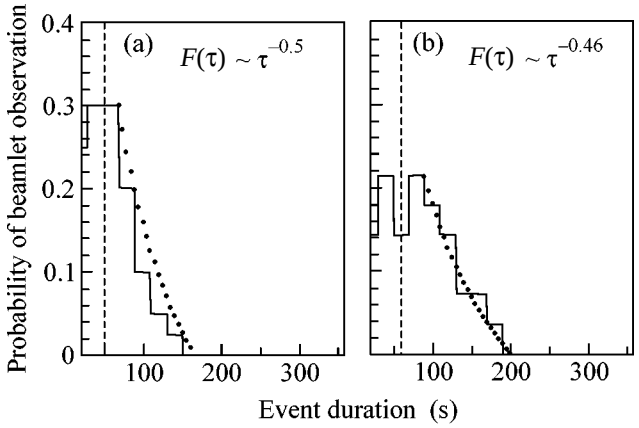

Fig. 6. Probability of beamlet observation vs. event duration for beamlets observed in the (a) auroral zone (Interball-2 satellite data) and (b) the tail (Interball-1 satellite data).

about 1 min, and the distribution tail is well approximated by the power law $F(\tau) \sim \tau^{-0.5}$, where τ is the beamlet observation duration. We remind that the conditions of the beamlet detection are different in the tail and auroral zone: the velocities of the Interball-1 and Interball-2 satellites, as well as the velocities of the plasma convection, are different. The similarity of the beamlet distributions in both cases seems to be evidence that a time scale of 1–1.5 min is the actual duration of beamlets; i.e., it is the characteristic time of the impulse acceleration of particles in the far tail. However, a contradiction with the absence of velocity dispersion in a beamlet arises in this case. According to the experimental data, the spread of the longitudinal velocities of ions in the beamlet is equal to 200–500 km/s. Nevertheless, all the ions are observed almost simultaneously near the Earth. If the acceleration source worked in the impulse mode (i.e., the particles were simultaneously accelerated to different energies) for the absence of dispersion (at least, to within the time resolution of the instrument), this source would be close to the beamlet detection point (according to our estimates, at a distance of no more than 4 R_E). Otherwise, higher energy ions would be observed noticeably earlier than lower energy ions. Since both theory and experiment indicate that beamlets are generated in the far regions of the tail (at distances of about 100 R_E from the Earth), the absence of dispersion can be explained only by assuming that the generation of beamlets is not instantaneous; i.e., the source operates at least for 10–15 min. In this case, beamlets are spatial structures with a limited lifetime rather than purely temporal structures (short-lived plasma bursts). Observations of beamlets the CLUSTER satellites, which are presented in the next section, corroborate this assumption.

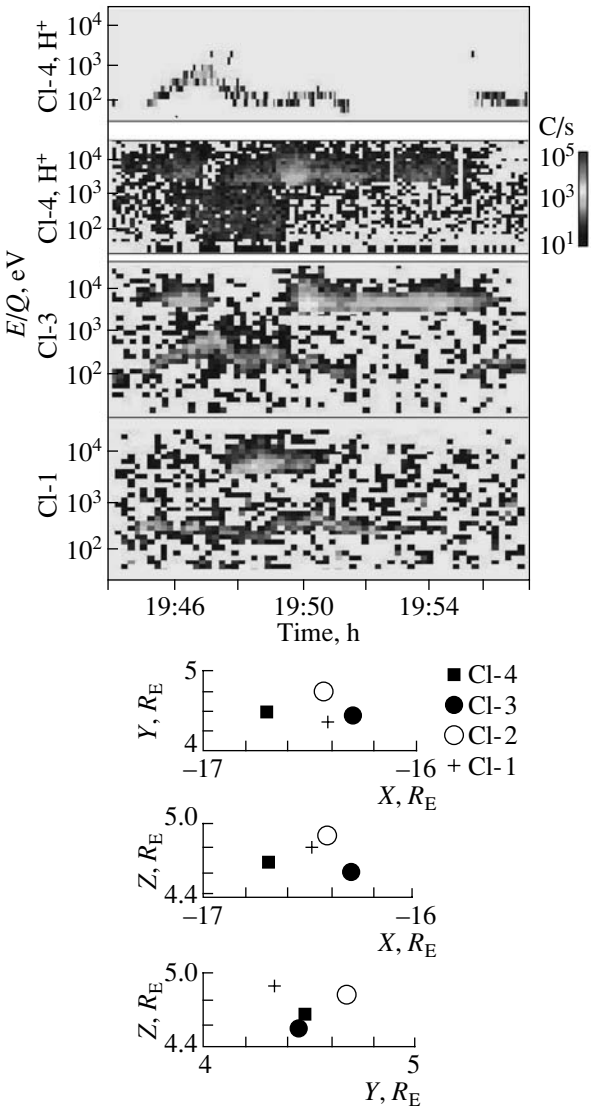

Fig. 7. Beamlet observed from three CLUSTER satellites (Cl-1, Cl-3, and Cl-4). Upper panel: (from top to bottom) the O^+ ion spectrogram measured on the Cl-4 satellite, the H^+ ion spectrogram measured on the Cl-4 satellite, the ion spectrogram (without mass resolution) measured on the Cl-3 satellite, and the ion spectrogram measured on the Cl-1 satellite. Lower panel: the position of the CLUSTER satellites in the time interval under consideration (from top to bottom, in the XY_{GSM}, XZ_{GSM}, and YZ_{GSM} planes).

5. OBSERVATION AND ANALYSIS OF THE BEAMLET STRUCTURE USING CLUSTER SATELLITE DATA

5.1. CLUSTER Satellite Observations of Beamlets in the Magnetotail

Figure 7 shows the beamlet observed on three CLUSTER satellites (hereinafter, they are denoted as Cl-1, Cl-3, Cl-4) on September 21, 2001. Unfortunately, ion measurements are unavailable on the fourth satellite (Cl-2). This event was observed under abso-

lutely quiet geomagnetic conditions. In the ion spectrograms shown in Fig. 7, as well as in spectrograms recorded on the Interball-1 satellite (Fig. 3), the beamlet is observed for a short time, has an energy of about 10 keV, and velocity dispersion is virtually absent. Nevertheless, simultaneous measurements at three points reveal some features that cannot be observed from one satellite (Interball-1). On the spectrogram obtained from the CLUSTER satellites, it is clearly seen that the beamlet is first observed on the Cl-3 and Cl-4 satellites for 1.5 min (19:45:30–19:47). The third satellite Cl-1 does not observe the beamlet at that time. Then, the Cl-1 satellite begins to observe the beamlet at 19:47:30, whereas the Cl-3 and Cl-4 satellites cease to observe it. Finally, the Cl-3 and Cl-4 satellites again begin to observe the beamlet at 19:50, whereas it was not observed on the Cl-1 satellite. Such features in the beamlet observation indicate that it has complex geometry, which will be explicitly analyzed in the next section. Here, we point to one more phenomenon that is associated with the origin of the beamlet and has not been observed previously. On the spectrograms shown in Fig. 7, it is clearly seen (particularly in the Cl-3 and Cl-4 satellite data) that the energy of the cold plasma increases (the lower part of the spectrograms) at the instant of the beamlet's pass and the energy of cold ions is maximal at the beamlet boundary. The cold plasma that is extracted from the ionosphere and fills the high-latitude part of the tail is not usually observed by detectors because its energy is lower than the sensitivity threshold of the instruments. However, when some disturbances, such as Alfvén waves, pass, this plasma can be accelerated by the varying electric field associated with the disturbance and it can become observable for the detectors [26]. In this sense, an increase in the velocity of the cold plasma can serve as a good indicator of the motion of magnetic tubes occupied by beamlet ions. We use this phenomenon in the next section when analyzing the spatial structure of the beamlet.

5.2. Analysis of the Spatial Structure of the Beamlet

Let us consider the positions of the CLUSTER satellites in the time interval 19:40–20:00 under investigation (the lower panel in Fig. 7). The Cl-1 satellite is always higher (along Z_{GSM}) than the Cl-3 and Cl-4 satellites. Since the satellites in this case were in the northern lobe of the tail, this means that the Cl-1 satellite was farther from the plasma sheet than the Cl-3 and Cl-4 satellites were; the distance between the Cl-1 and Cl-3 satellites was equal to about 0.3 R_E (the Cl-3 and Cl-4 satellites have virtually identical Z_{GSM} coordinates). Moreover, the satellites were separated along the Y_{GSM} direction. The Cl-3 and Cl-4 satellites were maximally separated in the X direction. Since their observations of the beamlet are virtually identical, one can assume that the longitudinal size of the beamlet (along the X direction) is much larger than the distance between the satellites (>0.4 R_E). Thus, the observed beamlet is spatially localized (i.e., its size is smaller than the distances between the satellites) along the directions Y_{GSM} and/or Z_{GSM}. In order to involve the fourth measurement point (Cl-2 satellite), we use the magnetic field measurements that are available on all four satellites. It turns out that the variations in the magnetic field components observed on the Cl-2, Cl-3, and Cl-4 satellites are similar to each other, whereas they are different on the Cl-1 satellite. One may assume that the beamlet and the corresponding disturbance of the magnetic field first pass through the Cl-2, Cl-3, and Cl-4 satellites and then approach the Cl-1 satellite. Introducing a new coordinate system $X'Y'Z'$, where the X' axis is directed along the unperturbed magnetic field lines of the high-latitude part of the magnetotail, the Y' axis passes through the Cl-2, Cl-3, and Cl-4 satellites, and the Z' axis complements the right-handed triple, we plot the hodograph of the magnetic field in the $Y'Z'$ plane for the time interval corresponding to the beamlet observation (Fig. 8). The hodographs are virtually symmetric in the $Y'Z'$ plane for all four satellites, and the variation in the magnetic field is maximal along the Y' direction. Moreover, the variations in the magnetic field component $B_{Y'}$ and the velocity component $V_{Y'}$ of the cold plasma (which was mentioned in the preceding section) occur synchronously and are maximal at the beamlet boundary. Let the beamlet be coupled with a magnetic disturbance propagating toward the Earth with a velocity of V_{prop} along the magnetic field lines (along the X' axis of our coordinate system, Fig. 9). Owing to the freezing of the mag-

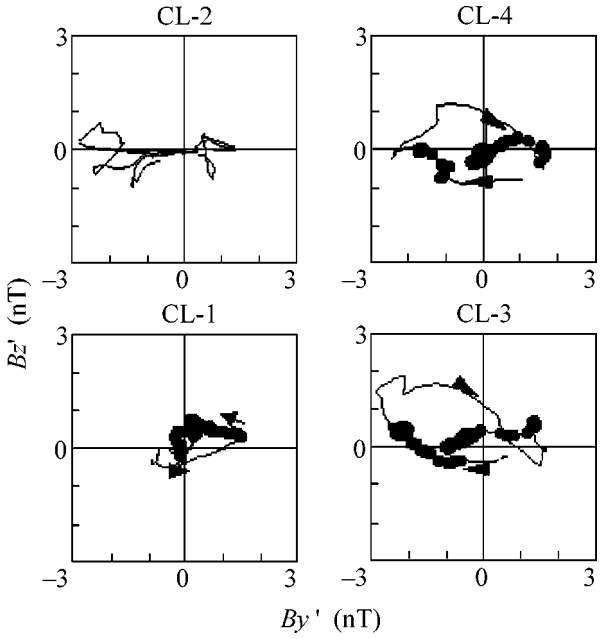

Fig. 8. Magnetic field hodographs plotted in the $B_{Y'}$–$B_{Z'}$ coordinates for the time interval 19:44–19:54. The circles are the times of the beamlet observation (observation of particles with energies higher than 5 keV).

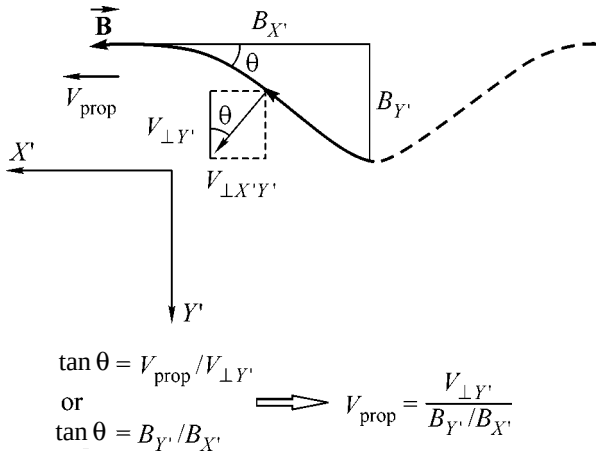

Fig. 9. Scheme of the magnetic field disturbance (snake) coupled with the beamlet in the (*X*'*Y*') plane. The condition of freezing of the magnetic field to the cold plasma provides a formula for determining the disturbance propagation velocity V_{prop} along the unperturbed magnetic field direction in terms of the measured cold-plasma velocity component $V_{\perp Y'}$ and the magnetic field components $B_{Y'}$ and $B_{X'}$.

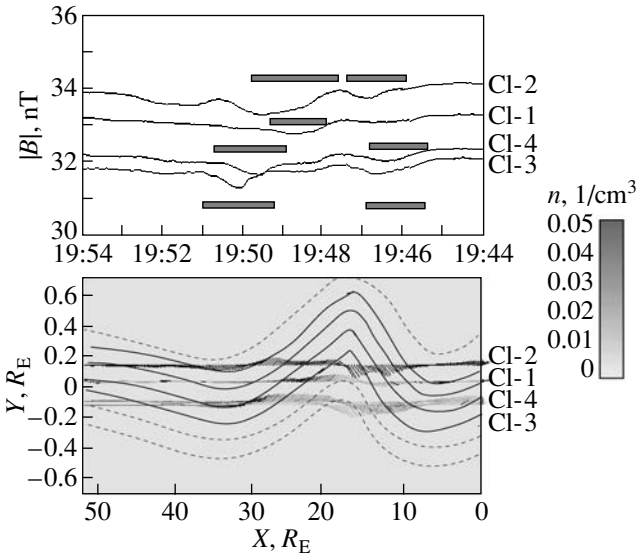

Fig. 10. Instantaneous "photograph" of the spatial structure of the beamlet (in the *X*'*Y*' projection). The spatial scale *X*' (in R_E) in the lower panel corresponds to the time scale in the upper panel. The upper panel: the time dependence of the magnetic field magnitude |*B*| (in nT) according to the data from four CLUSTER satellites (the satellite numbers are indicated on the right). The closed rectangles are the periods of decreasing |*B*| (diamagnetic effect), which are initiated by the passage of high-energy ions (beamlet) through the corresponding satellite. The lower panel: the projections of the magnetic field in the (*X*'*Y*') plane as measured on four CLUSTER satellites. For the Cl-1, Cl-3, and Cl-4 satellites (on which the plasma measurements are available), the magnetic field projections are shown by the gray tones corresponding to the density of ions with energies above 5 keV (beamlet) according to the scale shown in the right part of the figure. With the use of the data on the beamlet density and on the time dependence of |*B*|, the projections of the magnetic field lines that contain beamlet ions and sequentially pass through all four CLUSTER satellites are plotted by the solid lines.

netic field to the cold component of the plasma, variations in the magnetic field (which, as was shown above, occur primarily along the *Y*' direction) must be directly related to changes in the velocity $V_{\perp Y'}$ of the cold plasma. The relation between $B_{Y'}$ and $V_{\perp Y'}$ makes it possible to determine the disturbance propagation velocity along the magnetic field as

$$V_{prop} = \frac{V_{\perp Y'}}{B_{Y'}/B_{X'}} \quad (1)$$

(see Fig. 9). Thus, the velocity V_{prop} is equal to the slope of the plot of the Cl-1, Cl-3, and Cl-4 satellite data in the coordinates $B_{Y'}/B_{X'}$ and $V_{\perp Y'}$. The velocity of the disturbance propagation was equal to 570 km/s, and the Alfvén velocity calculated from a magnetic field magnitude of |*B*| = 31 nT and a plasma density of $n_{H+} = n_{O+} = 0.06$ cm^{-3}, which were observed at that time, was equal to $V_A = 640$ km/s. These two velocities are close to each other. Therefore, one may assume that the disturbance coupled with the beamlet is an Alfvén wave propagating toward the Earth.

Knowing the disturbance propagation velocity along the magnetic field (along the *X*' axis), one can transform the time variations to spatial variations as $X_i' = t_i V_{prop}$ (where t_i is the times when the beamlet was observed) and study the beamlet geometry. Figure 10 shows the projections of the magnetic field onto the (*X*'*Y*') plane that were measured in the time interval 19:44–19:54. This time interval was transformed to spatial coordinates *X*', where *X*' = 0 corresponds to the beginning of the analyzed time interval (19:44). The magnetic field projections measured on the Cl-1, Cl-3, and Cl-4 satellites are shown by the gray tones corresponding to the density of high-energy ions (*E* > 5 keV) according to the scale shown in the right part of the figure. Thus, it is seen on which magnetic field lines the beamlet is located and which magnetic field lines are empty (these lines are shown by the dashed lines). Since the Cl-2 satellite did not perform plasma measurements and we could not directly indicate the beamlet localization by the gray tone, to determine the beamlet structure, we used additional data on the time dependence of the magnetic field magnitude and the total flux of electrons with energies 0.1–1 keV, which were available from all four satellites. Moreover, to correctly reconstruct the beamlet geometry, we take the distances between the CLUSTER satellites in the *Y*' direction equal to the values that were in the indicated time interval. Thus, Fig. 10 is an instantaneous "photograph" of the beamlet. This figure clearly shows that the beamlet is a "snake" propagating in the *X*'*Y*' plane. The width of this snake in the *Y*' direction is as small as 0.25 R_E, whereas the length of the beamlet structure in the

X' direction is no less than 25 R_E. Unfortunately, this event provides no information on the beamlet size in the Z' direction. As seen in Fig. 10, good agreement between the magnetic field projections in the time interval 19:46–19:48 was observed only for the Cl-2, Cl-3, and Cl-4 satellites (through which common magnetic field lines can be drawn) and only these satellites detected the beamlet in this time interval (the Cl-1 satellite did not detect the beamlet, because this satellite was located higher in Z'). However, in the time interval 19:48–19:51, the magnetic field projections measured on all four satellites agreed well with each other: the magnetic field lines containing the beamlet sequentially pass through all four satellites. This means that the field tubes containing the beamlet rose up to the Cl-1 level and the size of the beamlet in the Z' direction exceeds the distance between the satellites, i.e., is larger than 0.3 R_E.

Thus, the beamlet is a plasma structure that is elongated along the magnetic field and whose longitudinal size is larger than its transverse size by a factor of several tens. This experimentally determined fact finally corroborates the fact that beamlets are generated in the spatially localized regions of the current sheet of the magnetotail. Therefore, they are manifestations not of the large-scale reconnection but of local acceleration sources acting in various parts of the far current sheet.

A new interesting feature of the beamlet is its bending. Since a beamlet is a beam of fast ions (in the case under consideration, the velocity of the ions along the magnetic field was equal to about 800 km/s) with a pronounced temperature anisotropy ($T_\parallel \gg T_\perp$), at the time of the ejection of the beamlet from the current sheet to the high-latitude region of the tail, fire-hose instability is developed in the beam and gives rise to the bend of the magnetic field lines along which the beamlet propagates, i.e., to the excitation of the Alfvén wave. Indeed, fire-hose instability arises under the condition $p_\parallel - p_\perp > B_{lobe}^2/4\pi$, where $p_\parallel$ and $p_\perp$ are the plasma pressures along and across the magnetic field, respectively, and B_{lobe} is the magnetic field magnitude where the ion beam propagates. Since beamlets are generated in far regions of the magnetotail (at distances of about 100 R_E from the Earth), where the high-latitude magnetic field B_{lobe} is quite weak ($B_{lobe} \sim 5$–8 nT), the condition of fire-hose instability is easily satisfied. Indeed, in the example under consideration, the plasma density in the beamlet is equal to $n = 0.05$ cm^{-3} and the longitudinal and transverse temperatures are equal to $T_\parallel = 8$ keV and $T_\perp = 20$ eV, respectively. Therefore, $p_\parallel = 0.064$ nPa, $p_\perp = 0.00016$ nPa ($p_\parallel - p_\perp = 0.063$ nPa), and $B_{lobe}^2/4\pi = 0.05$ nPa (for $B_{lobe} = 8$ nT); i.e., $(p_\parallel - p_\perp)/(B_{lobe}^2/4\pi) \approx 1.5 > 1.0$. Thus, when the beamlet enters the high-latitude region of the tail, fire-hose instability arises in the tail and generates the Alfvén wave, which propagates in the $X'Y'$ plane. As known from magnetohydrodynamics, the plasma is hydrodynamically stable if the magnetic field increases with the distance from the plasma boundary [27]. Magnetic field gradients can stabilize the development of fire-hose instability. In this sense, one can expect that unstable magnetic disturbances will be polarized in the XY plane, because the gradients of all the parameters of the plasma and magnetic field across the tail (in the Z_{GSM} direction) are at least two orders of magnitude higher than those in the morning–evening direction are (i.e., along the Y_{GSM} direction). Thus, the basic component of the Alfvén disturbance must be directed along the Y_{GSM} direction, as was observed in the experiments.

Thus, the CLUSTER multisatellite measurements revealed a new feature of beamlets that was not detected previously. The excitation of the fire-hose instability on the magnetic field lines along which the beamlet propagates makes it possible to experimentally estimate at least the lower bound of the distance from the Earth to the source of its generation (using the maximum value B_{lobe} for which the instability criterion can still be satisfied). In particular, the instability condition is still satisfied for $B_{lobe} = 8$ nT in the example under consideration. According to the magnetic field measurements made by the Geotail satellite in the far tail, this field value is observed at distances ≥80 R_E [28].

Thus, according to the CLUSTER multipoint measurements, beamlets are spatial structures. The short time of their observation (1–2 min) is attributed to the motion of the beamlet with respect to the satellite, and such motion is possible not only in the vertical plane (the flapping of the plasma sheet along the Z axis) but also in the horizontal plane (along the Y axis) due to the bending of force tubes along which beamlet particles move. The close times of the detection of beamlets observed in the tail and auroral zone (Fig. 6) does not contradict this statement. This can be proved as follows.

Indeed, the beamlet observation time is $\Delta t = L/V_\perp$, where L is the transverse size of the beamlet and $V_\perp$ is the velocity of the magnetic tubes filled with beamlet ions across the magnetic field. According to Eq. (1), the transverse velocity of the tubes is related to the longitudinal velocity of the disturbance propagation (Alfvén velocity) as

$$V_\perp = \frac{V_A B_\perp}{B} \approx \frac{B_\perp}{\sqrt{n m_i}}, \quad (2)$$

where V_A is the Alfvén velocity, n is the plasma density, m_i is the mass of ions (predominantly H^+), and $B_\perp$ is the magnetic field component that is perpendicular to the unperturbed magnetic field B and arises upon passing the beamlet. Let S_1 and S_2, B_1 and B_2, and $B_{1\perp}$ and $B_{2\perp}$ be the section areas, unperturbed magnetic fields, and perpendicular components of the magnetic field in the tail and auroral zone, respectively. Then, from the con-

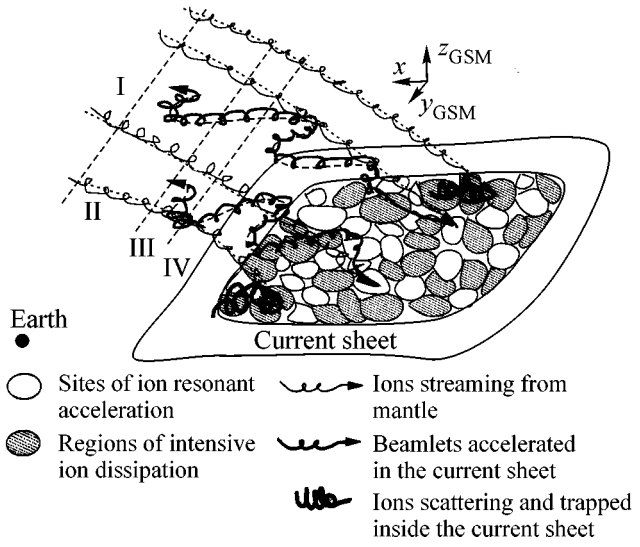

Fig. 11. Scenario of the generation of beamlets in the current sheet of the Earth's magnetotail. For the processes of the transformation and dissipation of energy, the current sheet is not homogeneous, but it is space consisting of intermittent (shaded ovals) regions of intense ion dissipation and (open ovals) sites of the resonant acceleration of the plasma. The distribution of these regions is not stationary. It continuously changes: in various parts of the current sheet, new regions of the resonant acceleration of beamlets flash or old such regions decay. The magnetosphere regions are (I) the mantle, (II) high-latitude part of the tail, (III) plasma sheet boundary layer, and (IV) the plasma sheet.

dition of the conservation of the energy flux of the wave connected with the beamlet, we obtain the condition

$$B_{1\perp}^2 S_1 = B_{2\perp}^2 S_2. \quad (3)$$

The magnetic flux conservation condition yields

$$B_1 S_1 = B_2 S_2. \quad (4)$$

Therefore,

$$B_{1\perp}/B_{2\perp} = \sqrt{B_1/B_2}. \quad (5)$$

Let Δt_1 and Δt_2 be the time interval of the beamlet observation in the tail and auroral zone, respectively. We verify whether these time intervals can be close, as was experimentally found in the preceding section under the assumption that the beamlet is a spatial structure. Using Eqs. (2)–(5), we obtain

$$\frac{\Delta t_1}{\Delta t_2} = \frac{\sqrt{S_1}/V_{1\perp}}{\sqrt{S_2}/V_{2\perp}} = \frac{B_2}{B_1}\sqrt{\frac{n_1}{n_2}}.$$

Since the magnetic field is equal to $B_1 \sim 30$ nT and $B_2 \sim 300$ nT in the high-latitude part of the tail and auroral zone, respectively, and the respective plasma densities are equal to $n_1 \sim 0.2$ cm^{-3} and $n_2 \sim 20$ cm^{-3}, the ratio of the time intervals of the beamlet observation is equal to $\Delta t_1/\Delta t_2 \approx 1.0$; i.e., the beamlet observation durations in both regions of the magnetosphere are indeed very close to each other due to the composition of the physical parameters. Thus, the statistical result presented in the preceding section does not contradict the new understanding of the beamlet as a spatial structure with which the Alfvén wave propagating toward the Earth is connected.

6. CONCLUSIONS

The available satellite measurements have sufficient time resolution to ensure *in situ* analysis of a fundamentally important physical phenomenon—the dissipation of the magnetic energy through localized short-time plasma injections as bursts. It is important that the magnetic field energy is transformed in this case not only to the chaotic heating of solar wind ions but also to the ordered (kinetic) energy of ion beams. This phenomenon has analogues in the solar atmosphere. As was shown by Parker [29] and other researchers, small-scale nanoflares, in which the basic energy heats the corona to millions of degrees, are the most important component of solar activity. Our conclusions concerning the nanoflares in the Earth's magnetotail are as follows.

(i) High-velocity ion beams (beamlets) are observed in the PSBL of the magnetotail and near the high-latitude boundary of the plasma sheet in the auroral zone as short plasma bursts, which are usually dispersionless and have energies of several tens of keVs and durations of 1–2 min.

(ii) Both in the tail and in the auroral zone, beamlets are localized near the plasma sheet boundary in a region with a latitude size of 0.5°–0.8°.

(iii) A beamlet is a spatial structure that is connected with an Alfvén wave propagating toward the Earth and exists for 10–15 min. Analysis of simultaneous observations of the beamlet at several points provides an estimate of its spatial sizes. The beamlet is elongated along the magnetic field: its longitudinal size (several tens of the Earth's radii) is much larger than the transverse size (no more than one Earth's radius). This is one more piece of evidence that beamlets are generated in the spatially localized regions of the current sheet of the magnetotail.

(iv) The multisatellite observations show that the beamlet is not a straight-line structure extended along the magnetic field (as was supposed previously) but has a snake shape formed due to the development of fire-hose instability, which arises when the beamlet leaves the current sheet at the site of its generation in the far tail of the magnetosphere. Using the maximum value of the magnetic field for which the fire-hose instability condition is still satisfied, one can estimate the lower bound of the distance from the Earth to the beamlet source. For the case under consideration, this distance exceeds ~80 R_E.

On the whole, our results corroborate the model of the nonadiabatic acceleration of the plasma that leads to the generation of beamlets during transient processes

sporadically occurring in various regions of the tail even under the quietest conditions. Such short-lived fast ion beams (beamlets) need not necessarily be associated with reconnection (i.e., with the change of the B_z sign in the current sheet). A pure nonadiabatic mechanism is possible in regions with a weak quasi-stationary magnetic field $B_z > 0$. If reconnection is a source of beamlets, it must certainly be localized in space. Such properties of reconnection occurring in the magnetotail have been actively discussed for the last decade [30–33]. In any case, the pattern of the transformation and dissipation of energy in the hot plasma of the magnetotail is associated with multisite (intermittent) events (Fig. 11) that flash in various parts of the current sheet [34, 35]. Such a pattern is very far from the recently dominating concepts of the globality and quasi-stationarity of such processes.

We are grateful to V.A. Sergeev for stimulating discussion and useful remarks. This work was supported by the Russian Foundation for Basic Research (project nos. 01-02-16367, 04-02-17371), the Council of the President of the Russian Federation for Support of Young Russian Scientists and Leading Scientific Schools (project no. NSh-1739.2003.2), the INTAS (grant nos. YS Felloship 03-55-1880, 00-04-65, 03-51-3738), and the Russian Foundation for Support of Domestic Science (program "Outstanding Scientists, Candidates, and Doctors of Science").

REFERENCES

1. L. R. Lyons and T. W. Speiser, J. Geophys. Res. **87**, 2276 (1982).
2. L. M. Zelenyi, J. Buchner, and D. V. Zogin, in *Proceedings of Varenne–Abustuman Workshop on Plasma Astrophysics* (Eur. Space Agency, 1988), Spec. Publ. ESA-SP285, Vol. 1, p. 227.
3. J. Buchner and L. M. Zelenyi, in *Proceedings of Varenne–Abustuman Workshop on Plasma Astrophysics* (Eur. Space Agency, 1988), Spec. Publ. ESA-SP285, Vol. 1, p. 219.
4. D. J. Williams, J. Geophys. Res. **86**, 5501 (1981).
5. M. K. Andrews, P. W. Daly, and E. Keppler, Geophys. Res. Lett. **8**, 987 (1981).
6. J. D. Winningham, F. Yasubara, S.-I. Akasofu, *et al.*, J. Geophys. Res. **80**, 3148 (1975).
7. T. W. Speiser, J. Geophys. Res. **70**, 4219 (1965).
8. B. U. O. Sonnerup, J. Geophys. Res. **76**, 8211 (1971).
9. J. Buchner and L. M. Zelenyi, Phys. Lett. A **118**, 395 (1986).
10. J. Buchner and L. M. Zelenyi, J. Geophys. Res. **94**, 11821 (1989).
11. J. Chen and P. J. Palmadesso, J. Geophys. Res. **91**, 1499 (1986).
12. M. Ashour-Abdalla, J. P. Berchem, J. Buchner, and L. M. Zelenyi, J. Geophys. Res. **98**, 5651 (1993).
13. G. Parks, L. J. Chen, M. McCarthy, *et al.*, Geophys. Res. Lett. **25**, 3285 (1998).
14. E. E. Grigorenko, A. O. Fedorov, and L. M. Zelenyi, Ann. Geophys. **20**, 329 (2002).
15. J.-A. Sauvaud and R. A. Kovrazhkin, in *Abstracts of 35th COSPAR Scientific Assembly, Paris* (2004), COSPAR04-A-01819 D3.1-0022-04.
16. A. Keiling, H. Reme, I. Dandouras, *et al.*, J. Geophys. Res. **109**, A05215 (2004).
17. V. Peroomian, M. Ashour-Abdalla, and L. M. Zelenyi, J. Geophys. Res. **105**, 18807 (2000).
18. V. Peroomian and L. Zelenyi, Space Sci. Rev. **95**, 257 (2001).
19. L. M. Zelenyi, R. A. Kovrazhkin, and J. M. Bosqued, J. Geophys. Res. **95**, 12119 (1990).
20. J.-A. Sauvaud, D. Popescu, D. C. Delcourt, *et al.*, J. Geophys. Res. **104**, 28565 (1999).
21. V. A. Sergeev, J.-A. Sauvaud, D. Popescu, *et al.*, J. Geophys. Res. **105**, 18465 (2000).
22. E. E. Grigorenko, A. O. Fedorov, L. M. Zelenyi, *et al.*, Adv. Space Res. **31**, 1271 (2003).
23. R. J. DeCoster and L. A. Frank, J. Geophys. Res. **84**, 5099 (1979).
24. T. G. Onsager, M. F. Thomsen, R. C. Elphic, *et al.*, J. Geophys. Res. **96**, 20999 (1991).
25. L. M. Zelenyi, A. L. Taktakishvili, E. M. Dubinin, *et al.*, in *Proceedings of the 9th COSPAR Colloquium on Magnetospheric Research with Advanced Techniques* (Beijing, China, 1996), p. 125.
26. J.-A. Sauvaud, P. Louarn, G. Fruit, *et al.*, J. Geophys. Res. **109**, AO1212 (2004).
27. N. A. Krall and A. W. Trivelpiece, *Principles of Plasma Physics* (Academic, New York, 1973; Mir, Moscow, 1975).
28. T. Yamamoto, K. Shiokawa, and S. Kokubun, Geophys. Res. Lett. **21**, 2875 (1994).
29. E. N. Parker, *Spontaneous Current Sheets in Magnetic Fields* (Oxford Univ. Press, New York, 1994).
30. V. A. Sergeev, R. C. Elphic, F. S. Mozer, *et al.*, Planet. Space Sci. **40**, 1551 (1992).
31. A. J. Klimas, J. A. Valdivia, D. Vassiliadis, *et al.*, J. Geophys. Res. **105**, 18765 (2000).
32. W. Liu, J. Geophys. Res. **106** (A1), 289 (2001).
33. T. Nagai, I. Shinohara, M. Fujimoto, *et al.*, J. Geophys. Res. **106**, 25929 (2001).
34. K. V. Chukbar, Zh. Éksp. Teor. Fiz. **108**, 1875 (1995) [JETP **81**, 1025 (1995)].
35. G. M. Batanov, V. E. Bening, V. Yu. Korolev, *et al.*, Pis'ma Zh. Éksp. Teor. Fiz. **73**, 143 (2001) [JETP Lett. **73**, 126 (2001)].

Translated by R. Tyapaev